



L-Università ta' Malta
Institute of Space
Sciences & Astronomy

Detection of Orbital Debris in Low Earth Orbit

Denis Cutajar

June, 2020

Supervisor

Dr Alessio Magro

Co-Supervisor

Prof. Kristian Zarb Adami

A dissertation presented to the Institute of Space Sciences and Astronomy in part fulfillment of the requirements for the degree of Doctor of Philosophy at the University of Malta



L-Università
ta' Malta

University of Malta Library – Electronic Thesis & Dissertations (ETD) Repository

The copyright of this thesis/dissertation belongs to the author. The author's rights in respect of this work are as defined by the Copyright Act (Chapter 415) of the Laws of Malta or as modified by any successive legislation.

Users may access this full-text thesis/dissertation and can make use of the information contained in accordance with the Copyright Act provided that the author must be properly acknowledged. Further distribution or reproduction in any format is prohibited without the prior permission of the copyright holder.

This work is dedicated to my beloved parents, whose encouragement and unwavering support led me to become the person I am today.

Acknowledgements

I would like to take this opportunity to thank the people who have been part of this journey and have assisted me either academically or emotionally during these past four years. Your support contributed to the success of this study.

First and foremost, I would like to express my sincere appreciation to my supervisor, Dr Alessio Magro, for his guidance and constant encouragement throughout my research. I would also like to extend my gratitude to my co-supervisor Prof. Kris Zarb Adami, for offering me the opportunity to study at the Institute of Space Sciences and Astronomy. I am also particularly grateful for the insightful feedback of Dr John Abela and Dr Andrea DeMarco at the Institute.

This work is the fruit of a collaborative effort between the University of Malta, the Italian National Institute for Astrophysics (INAF) and the Politecnico di Milano. I would like to thank Prof. Pierluigi Di Lizia, Matteo Losacco and Mauro Massari at the Politecnico di Milano and Germano Bianchi, Giuseppe Pupillo, Giovanni Naldi, Andrea Mattana and Luca Lama at the Medicina Radio Astronomy station. It has been a privilege to collaborate with such a group of accomplished individuals.

Most notably, I would like to thank Professor Charles V. Sammut, for motivating me into pursuing a career in research and Professor André Xuereb, for supporting my work at the Department of Physics. My special regards go to Professor Alfred Micallef, Dr Lourdes Farrugia and Dr Pierre Sandre Farrugia for their precious counsel throughout these years.

Further, I would also like to take the opportunity to recognise the exceptional team at the Physics Department for their invaluable assistance and dedication: Jesmond Debattista, Josette Costa, Isabelle Dimech, Kristian Grixti and the legendary Sandro Sapiano. My heartfelt thanks go to Mr Robert

Grech, and Ms Carmen Mifsud at the Physics Department for their sterling work in dealing with the administrative matters throughout my studies.

I would particularly like to thank my fellow PhD colleagues and friends at the UWBL and EMRG labs: Mark Bezzina, Andrew Finch, Xandru Mifsud, Dr Ian Fenech Conti, Miguel Zammit, Anastasia Seifert, Karl Fiteni, Livia Massa, Dr Gabriel Farrugia and Jeantide Said Camilleri. Thank you for the stimulating discussions and the long hours we spent working together to meet those pesky deadlines. I am profoundly thankful to the industrious Dr Iman Farhat for always finding the time to answer my questions and discuss my research.

This accomplishment would not have been possible without the emotional support of my close friends at the University. My deepest gratitude goes to Julian Bonello, Josef Borg, Dr Daniela Farrugia and Dr Sara Fenech for being a significant source of support when the road ahead was darkest and the future was uncertain. Thank you for listening and offering me your most valuable advice. You have given me the best coffee breaks of my life!

I reserve my biggest thanks to my close friends and family, most notably my parents, for their unfailing support, especially during these last few months. Finally, I wish to thank my loving and supportive significant other, Laura Cumbo, for having stuck by my side during the past decade. I am forever in your debt.

Abstract

The ever increasing satellite population in near-Earth orbit has made the monitoring and tracking of active satellites, and orbital debris objects ever more critical. As the in-orbit population grows, so does the risk of a collision. In recent years, the European Space Agency (ESA)'s Space Situational Awareness (SSA) programme has been assisting national institutions in the upgrading of their space detection and monitoring capabilities. One of the latest such systems within this programme is the Bi-static RAdar for LEO Survey (BIRALES) space surveillance system consisting of a radio transmitter in Caligari, Sardinia and the BEST-2 phased array in Medicina, near Bologna, Italy. This research lays out the foundation for a new space debris detection system for this novel sensor. First, this work introduces a new software backend that makes use of data processing pipelines to process the incoming data from the 32-antenna radio telescope in real-time. The detection pipeline channelises and beamforms the incoming antenna signals, creating a multi-pixel of beams covering the Field of View (FoV) of the instrument. The detection algorithm uses a series of filters to pre-process the incoming data from any interference. In this study, two novel track detection algorithms are presented. These algorithms identify the unique doppler echo tracks emanating from resident space objects crossing the FoV of this bi-static radar. Candidates are identified by these algorithms are validated to reject false positives. The trajectory of the detected objects is determined by considering the illumination sequence of the multi-pixel. Initial experimental results from observation campaigns of known objects show that the radar can reliably detect in-orbit objects down to a few centimetres in size in Low Earth Orbit (LEO). These encouraging results represent the latest scientific contribution from Europe's emerging space debris monitoring radar within its growing network of European Space Surveillance and Tracking (SST) systems.

Publications

Parts of the work presented in this thesis have been previously presented or published in:

1. **Cutajar, D.**, Magro, A., Borg, J., Adami, K. Z., Bianchi, G., Pupillo, G., ... others. (2020). PyBIRALES: A Radar Data Processing Backend for the Real-Time Detection of Space Debris. *Journal of Astronomical Instrumentation*, 9.
2. **Cutajar, D.**, Magro, A., Borg, J., Zarb Adami, K., Bianchi, G., Bortolotti, C., ... others. (2018). A real-time space debris detection system for BIRALES. In 69th International Astronautical Congress (IAC 2018) (pp. 1–9).
3. **Cutajar, D.**, Farhat, I., Magro, A., Borg, J., Kris, Z. A., and Charles, S. V. (2018). A Real-Time Antenna Verification System. In 2nd URSI AT-RASC.
4. Farhat, I., **Cutajar, D.**, Zarb Adami, K., and Sammut V, C. (2018). Field Trials for Ultrawideband Antenna. In 2nd URSI AT-RASC.
5. Farhat, I., **Cutajar, D.**, Bezzina, M., and Adami, K. Z. (2019). Drone Characterization Approach for Radio Telescopes. In 2019 PhotonIcs and Electromagnetics Research Symposium-Spring (PIERS-Spring) (pp. 3016–3018).
6. Di Lizia, P., Massari, M., Losacco, M., Bianchi, G., Mattana, A., Pupillo, G., **Cutajar, D.**, ... others. (2017). Performance assessment of the multibeam radar sensor birales for space surveillance and tracking. In Proceedings of 7th European Conference on Space Debris.

7. Bianchi, G., Bortolotti, C., Cattani, A., Fiocchi, F., Maccaferri, A., Mattana, A., **Cutajar, D.**, ... others. (2017). A new approach to LEO space debris survey: the Italian multibeam bi-static radar 'BIRALES'. In 1st IAA Conference on Space Situational Awareness (ICSSA) (pp. 1–18).
8. Losacco, M., Di Lizia, P., Massari, M., Mattana, A., Perini, F., Schiano, M., **Cutajar, D.**, ... others. (2018). The multibeam radar sensor BIRALES: Performance assessment for space surveillance and tracking. In 69th International Astronautical Congress (IAC 2018) (pp. 1–9).
9. Farhat, I., **Cutajar, D.**, Adami, K. Z., Sammut, C., and Abela, J. (2018). Characterization of 36 Meter Square Mid-Frequency Radio Astronomy Prototype Antenna Array. In 2018 IEEE Conference on Antenna Measurements and Applications (CAMA) (pp. 1–3).
10. Losacco, M., Massari, M., Di Lizia, P., Bianchi, G., Pupillo, G., Mattana, A., **Cutajar, D.**, ... others. (2019). Multibeam Radar Technology applied to Space Surveillance in the LEO Regime. In 25th Conference of the Italian Association of Aeronautics and Astronautics (AIDAA 2019) (pp. 972–980).
11. Pupillo, G., Bianchi, G., Mattana, A., Naldi, G., Bortolotti, C., Roma, M., **Cutajar, D.**, ... others. (2019). Operational Challenges of the Multibeam Radar Sensor BIRALES for Space Surveillance. In First International Orbital Debris Conference.
12. Losacco, M., Di Lizia, P., Massari, M., Bianchi, G., Pupillo, G., Mattana, A., **Cutajar, D.**, ... others. (2019). Space Surveillance with the Multibeam Radar Sensor BIRALES. In 70th International Astronautical Congress (IAC 2019) (pp. 1–8).
13. Losacco, M., Di Lizia, P., Massari, M., Mattana, A., Perini, F., Schiaffino, M., **Cutajar, D.**, ... Villadei, W. (2018). Orbit Determination of Resident Space Objects with the Multibeam Radar Sensor BIRALES. 2018 Space Flight Mechanics Meeting, (January). <https://doi.org/10.2514/6.2018-0729>.

Other Contributions

1. Magro, A., Demarco, A., Adami, K. Z., **Cutajar, D.**, and Borg, J. (2017). A monitoring and control prototype for the SKA low frequency aperture array. In 2017 International Conference on Control, Automation and Diagnosis, ICCAD 2017. <https://doi.org/10.1109/CADIAG.2017.8075701>.
2. Magro, A., Chiello, R., **Cutajar, D.**, Borg, J., Zarb-Adami, K., ... others. (2019). A New Digital Backend for the Mexican Array Radio Telescope. In 2019 International Conference on Electromagnetics in Advanced Applications (ICEAA) (pp. 185–189).
3. de Vaate, J. G. B., Bast, J., Benthem, P., Gerbers, M., Wijnholds, S. J., Booler, T., **Cutajar, D.**, ... others. (2018). The SKA1_Low Telescope: The Station Design and Prototyping. In 2018 2nd URSI Atlantic Radio Science Meeting (AT-RASC) (p. 1).
4. Benthem, P., Gerbers, M., De Vaate, J. G. B., Wynholds, S., Bast, J., Booler, T., **Cutajar, D.**, ... Adami, K. Z. (2017). The low frequency receivers for SKA 1-low: Design and verification. In 2017 32nd General Assembly and Scientific Symposium of the International Union of Radio Science, URSI GASS 2017 (Vol. 2017-Janua). <https://doi.org/10.23919/URSIGASS.2017.8104992>.

Contents

1	Introduction	1
1.1	Orbital debris	2
1.2	Mitigation measures	7
1.3	Sensors for space situational awareness	8
1.4	Conclusion	13
2	Space Situational Awareness using the BEST-II phased array	15
2.1	The Northern Cross	16
2.2	The BEST-II phased array	18
2.2.1	An electromagnetic model of the BEST-II array	22
2.2.2	Beam steering	28
2.3	Calibration	31
2.4	Space surveillance using the BEST-II phased array	35
2.5	Doppler shift	37
2.6	The radar equation	40
2.7	Radar capability	43
2.8	Conclusion	48
3	The BIRALES bi-static radar	49
3.1	The BIRALES radar	49
3.2	System overview	55
3.2.1	Ranging system	55
3.2.2	Doppler processing	58
3.3	Stream data processing in radio astronomy	60
3.4	Architecture	62
3.5	Observation scheduling	66
3.6	Hardware Controllers	68

3.7	Data processing pipelines	69
3.7.1	Pipeline builders	70
3.7.2	Data blobs	71
3.8	Correlation pipeline	74
3.9	Detection pipeline	75
3.9.1	Data acquisition	76
3.9.2	Beamforming and multi-pixel generation	77
3.9.3	Channeliser	82
3.9.4	Detection	85
3.10	Frontend	87
3.11	Conclusion	91
4	Detection of Orbital Debris	93
4.1	Track detection in spectrograms	94
4.2	Detection strategy in PyBirales	97
4.3	Pre-processing	98
4.4	Filtering	98
4.4.1	Transmitter filter	99
4.4.2	Background noise filtering	99
4.4.3	Salt-and-pepper noise filter	100
4.4.4	Evaluation	101
4.5	Track initiation	106
4.5.1	DBSCAN clustering	107
4.5.2	A multi-beam streak detection algorithm	110
4.5.3	Evaluation	116
4.6	Track association	119
4.7	Track termination	120
4.8	Conclusion	121
5	Experimental Results	123
5.1	Experimental results	124
5.2	The re-entry of the Tiangong-1 space station	127
5.3	NORAD 1328	132
5.4	Conclusion	136
6	Conclusion	139
6.1	Future work	141

A Appendix	143
A.1 Antenna Verification	143
A.1.1 A real-time antenna verification system	145
A.1.2 Real-time synchronisation	147
A.1.3 Monitoring application	148
A.1.4 Methodology	149
A.1.5 Results	152
A.1.6 Future work	153
A.2 Performance metrics	155
Bibliography	157

List of Figures

1.1	The evolution of the total payload mass put in orbit	1
1.2	Number of fragmentation events	2
1.3	A typical crater left by a hyper-velocity	4
1.4	Inclination distribution of catalogued in-orbit objects	5
1.5	Eccentricity distribution of the catalogued in-orbit objects	5
1.6	Altitude distribution of the catalogued in-orbit objects	6
1.7	The Haystack facility in Massachusetts, US	10
1.8	The Goldstone radar system	10
1.9	The TIRA radar facility	11
1.10	The GRAVES radar	12
2.1	The Northern Cross in Medicina, Bologna Italy. Source: www.jodrellbank.manchester.ac.uk	17
2.2	The BEST-2 array	18
2.3	Model of a single antenna element	23
2.4	The simulated azimuth and elevation cuts of a dipole element	24
2.5	The simulated beam pattern for a sub-array receiver	26
2.6	The simulated beam pattern of the BEST-2 array	27
2.7	Illustration of the steering of the BEST-2 radiation pattern	28
2.8	Angle deviation as a function of the azimuthal pointing away from broadside	29
2.9	Experimental verification of the simulated beam pattern	31
2.10	Baseline visibilities before and after calibration	33
2.11	Complex gain solutions obtained through 10 calibration observations	35
2.12	A representative doppler curve that is typical of a passage from a high-velocity orbiting objects such as a satellite	39
2.13	Attenuation of the radar signal	43

2.14	The theoretical radar range	45
2.15	The relationship between the diameter of a detectable target and the working frequency frequency	46
2.16	The theoretical range as a function of the transmitter power .	47
3.1	The parabolic antenna in ‘Salto di Quirra’, Caligari, Sardinia [90]	50
3.2	The BIRALES bi-static radar	51
3.3	The theoretical SNR as a function of range	52
3.4	A performance comparison between the BIRALES radar and existing instruments	54
3.5	Overview of the BIRALES components	56
3.6	Transmitted and reflected signal used by the ranging system .	57
3.7	An illustration of the three-tier architecture of the PyBiraless space debris processing system	64
3.8	Illustration of typical observation schedule	67
3.9	A graphical representation of processing pipeline	69
3.10	A UML Class diagram of the pipeline manager builder	71
3.11	A graphical representation of a data block	72
3.12	A graphical representation of a ring buffer	73
3.13	A UML sequence diagram of the concurrency pattern of a typ- ical processing module in PyBiraless	74
3.14	The BIRALES correlation pipeline	75
3.15	The PyBiraless detection pipeline	76
3.16	Beamformer tests on astronomical sources	78
3.17	The multi-pixel configuration of the BIRALES radar	79
3.18	An alternative configuration for the BIRALES multi-pixel . .	80
3.19	Beamformer performance benchmarking tests	81
3.20	Channeliser performance benchmarking tests	84
3.21	A typical radar echo emanating from a space debris object . .	86
3.22	A block diagram of the web-application	88
3.23	The BIRALES monitoring dashboard	89
3.24	The event-log page of the BIRALES control application	90
3.25	Visualisation of the results of the BIRALES control application	91
4.1	Typical tracks that are present in passive sonar spectrogram images	97
4.2	Kernel used for speck noise removal	101

4.3	An example of the test used to evaluate the performance of the detection algorithms	102
4.4	Output of the Triangle filter algorithm	104
4.5	Image segmentation algorithms performance comparison	105
4.6	Performance benchmark of the image segmentation algorithms	106
4.7	Clusters identified by the DBSCAN algorithm	109
4.8	Visualisation of the input data	111
4.9	Visualisation of the inertia ratio calculation	113
4.10	Hierarchical clustering	114
4.11	Second stage clustering	114
4.12	An example of a crossing track test data	115
4.13	The resultant track upon track validation	116
4.14	Performance metrics of four streak detection algorithms	118
4.15	Performance benchmark of four streak detection algorithms	118
5.1	Overview of the observation campaigns performed by the BI-RALES radar	124
5.2	RCS as a function of SNR	125
5.3	Slant range as a function of SNR	126
5.4	Doppler shift measurements for the Tiangong-1 observation	129
5.5	SNR profile for the Tiangong-1 observation	129
5.6	Beam illumination sequence for the Tiangong-1 observation	130
5.7	Beam trajectory prediction and comparison with simulations	131
5.8	Doppler shift results for the NORAD 1328 observation	133
5.9	SNR profile for the NORAD 1328 observation	134
5.10	Beam illumination sequence for the NORAD 1328 observation	134
5.11	Beam trajectory prediction and comparison with simulations	135
A.1	System overview of the ChopPy antenna verification system	145
A.2	UML sequence diagram of the real-time synchronisation algorithm	148
A.3	The ChopPy monitoring application	150
A.4	The model used for the log-periodic antenna	151
A.5	Visualisation of the radiation pattern	152
A.6	Validation of the measured radiation pattern	153

List of Tables

2.1	The Northern Cross radio telescope	16
2.2	System specification of the BEST-2 array	19
3.1	SSA radar capabilities	53
5.1	Observation parameters for the Tiangong-1 observation	128
5.2	Observation parameters for the NORAD 1328 observation	133
A.1	Performance metrics for the image segmentation algorithms	155
A.2	Performance metrics for the feature detection algorithms	156

List of Abbreviations

AAVS	Antenna Verification System.
ANN	Artificial Neural Network.
ASI	Italian Space Agency.
ASTRiDE	Automated Streak Detection for Astronomical Images.
AUT	Antenna Under Test.
AZ	Azimuth.
BEST	Basic Element for SKA Training.
BIRALES	BIstatic RAdar for LEO Survey.
BIRALET	BIstatic RAdar for LEO Tracking.
BRAMS	Belgian Radio Detection System.
CAD	Computer-Aided Design.
CASPER	Collaboration for Astronomy Signal Processing and Electronics Research.
CLI	Command Line Interface.
CST	Computer Simulation Technology Studio Suite.
CW	Continuous Wave.
DAQ	Data Acquisition.
DBSCAN	Density-Based Spatial Clustering of Applications with Noise.
DFT	Discrete Fourier Transform.
DISCOS	Database and Information System Characterising Objects in Space.
DoD	Department of Defence.
EISCAT	European Incoherent Scatter Scientific Association.

EL	Elevation.
EM	Electromagnetic.
ESA	European Space Agency.
EU	European Union.
FFT	Fast Fourier transform.
FHR	Fraunhofer Institute for High Frequency Physics and Radar Techniques.
FIFO	First In First Out.
FIR	Finite Impulse Response.
FMCW	Frequency Modulated Continuous Wave.
FoV	Field of View.
FPGA	field-programmable gate array.
FPR	False Positive Rate.
GEO	Geostationary Earth Orbit.
GEODSS	Ground-based Electro-Optical Deep Space Surveillance.
GIL	Global Interpreter Lock.
GNSS	Global Navigation Satellite System.
GPU	Graphical processing unit.
GRAVES	Grand Réseau Adapté à la Veille Spatiale.
GUI	Graphical User Interface.
HASHPIPE	High Availability Shared Pipeline Engine.
HAX	Haystack Auxiliary.
HDF5	Hierarchical Data Format 5.
HMM	Hidden Markov Model.
HPBW	Half-Power Bandwidth.
HST	Hubble Space Telescope.
IADC	Inter-Agency Space Debris Coordination Committee.
INAF	Istituto Nazionale di Astrofisica.
IOD	Initial Orbit Determination.
IRA	Istituto di Radioastronomia.
ISAR	Inverse synthetic aperture radar.
ISS	International Space Station.
JSON	JavaScript Object Notation.
k-NN	k-Nearest Neighbors.

KA	Keep Alive.
LCS	Lincoln Calibration Sphere.
LEO	Low Earth Orbit.
LFAA	Low-Frequency Aperture Array.
LLVM	Low-Level Virtual Machine.
LNA	Low Noise Amplifier.
LOFAR	Low Frequency Array.
LOS	Line of Sight.
LRIR	Long-Range Imaging Radar.
MEO	Medium Earth Orbit.
MEXART	Mexican Array Radio Telescope.
MoD	Ministry of Defence.
MODA	Multibeam Orbit Determination Algorithm.
MOTIF	Maui Optical Tracking and Identification Facility.
MSDS	Multi-beam streak detection strategy.
NEO	Near Earth Orbit.
NI-VISA	National Instruments - Virtual Instrument Software Architecture.
ONERA	Office National d'Etudes et de Recherches Aérospatiales.
PAPER	Precision for Probing the Epoch of Reionization.
PCA	Principal Component Analysis.
PELICAN	Pipeline for Extensible, Lightweight Imaging and CALibrationN.
PFB	Polyphase Filter Bank.
PPS	Pulse Per Second.
PRF	Pulse Repetition Frequency.
PRI	Pulse Repetition Interval.
PSRDADA	PSR-Distributed Acquisition and Data Analysis.
RANSAC	Random sample consensus.
RCS	RADAR Cross Section.
RF	Radio Frequency.
RFI	Radio-Frequency Interference.

RMS	Root Mean Squared.
RMSE	Root Mean Square Error.
ROACH	Reconfigurable Open Architecture Computing Hardware.
RSO	Resident Space Object.
SKA	Square Kilometre Array.
SKADS	Square Kilometre Array Design Study.
SNR	Signal-to-Noise Ratio.
SPEAD	Streaming Protocol for Exchanging Astronomical Data.
SSA	Space Situational Awareness.
SSN	Space Surveillance Network.
SSS	Russian Space Surveillance System.
SST	Space Surveillance & Tracking.
StEFCal	Statistically Efficient and Fast Calibration.
TDM	Tracking Data Message.
TETRA	TErrestrial Trunked RAdio.
TIRA	Tracking and Imaging Radar.
TLE	Two-Line Element.
TN	True Negative.
TP	True Positive.
TPR	True Positive Rate.
TRF	Radio Frequency Transmitter.
UAV	Unmanned Aerial Vehicle.
UDP	User Datagram Protocol.
UHF	Ultra High Frequency.
UNCOPUOS	United Nations Committee on the Peaceful Uses of Outer Space.
USRP	Universal Software Radio Peripheral.
USSTRATCOM	United States Strategic Command.
UTM	Universal Transverse Mercator.
VHF	Very High Frequency.

Chapter 1

Introduction

Satellites have become indispensable to many areas and disciplines including telecommunications, climate research, navigation and human space exploration. Humanity's reliance on space-based technology makes the safeguarding of these assets of paramount importance. Since the launch of the first artificial satellite, the Russian Sputnik-1, the number of satellite launches has increased dramatically. This exponential growth can be seen in Figure 1.1. It is estimated that as of 2019, a total of 8500 t of space hardware have been put into Earth's orbit [1].

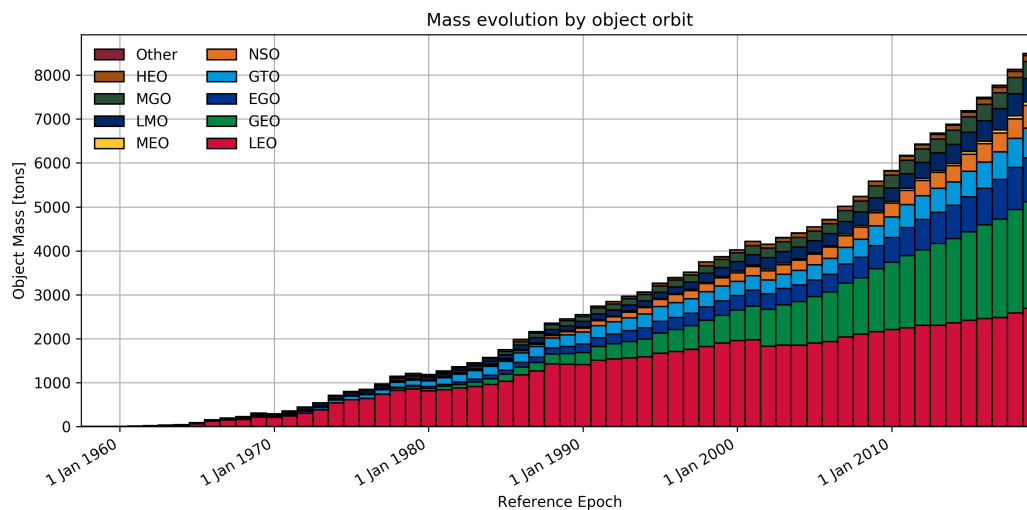


Figure 1.1: The evolution of the total payload mass put in orbit and the orbit these reside in [1]

Of the thousands of satellites that were put in orbit, only a fraction of these remain operational to date. Satellites are usually decommissioned at the

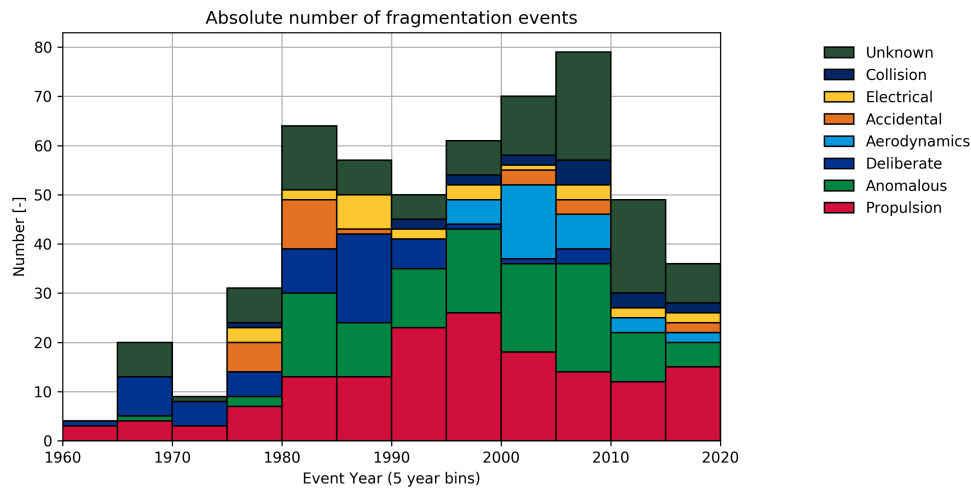


Figure 1.2: Number of fragmentation events that have occurred to date. The data is categorised by the most likely cause of the fragmentation event [1]

end of their mission which could span decades. During this time, they can also suffer from a fatal break-up. Break-ups are the result of either a system malfunction or an in-orbit collision. In either case, these fragmentation events lead to the proliferation of inactive hardware in Earth’s orbit. Figure 1.2 shows a breakdown of historical fragmentation events according to their most likely cause. One may note that most of these fragmentation events are due to propulsion issues and the number of events whose cause is unknown or anomalous is substantial. Klinkrad et al. (2006) stated that most (80 %) of the known fragmentations occurred at altitudes lower than 2000 km. The space environment is also home to spacecraft that were used to put the satellites in orbit. This list includes spent rocket bodies, exhaust and dust particles and leaked cooling agents [2]. These objects are commonly referred to as space or orbital debris.

1.1 Orbital debris

The United Nations Committee on the Peaceful Uses of Outer Space (UNCOPUOS)’s space debris mitigation guidelines defined space debris as:

All man-made objects, including fragments and elements thereof, in Earth orbit or re-entering the atmosphere, that are non-functional.

– UNCOPUOS [3]

Orbital debris objects can be categorised into three orbital classes depending on the altitude in which they reside. It is estimated that the vast majority of these objects (75%) of the catalogued objects are put in Low Earth Orbit (LEO) at a perigee altitude of less than 2000 km. Navigation Global Navigation Satellite System (GNSS) satellites are put in at a perigee altitude of 20 000 km [4]. At an altitude of 35 876 km, an inclination of $\sim 0^\circ$ and eccentricity of ~ 0.0 , Geostationary Earth Orbit (GEO) objects move synchronously with the Earth's rotation. On these orbits, one finds communication and meteorological satellites which makes this particular orbit of high commercial value. As of 2016, there are 7 per cent of the catalogued objects reside in GEO [5].

Large objects are routinely monitored, and their orbit is well known. However, only estimates are available for objects that are less than 10 cm in LEO and 1 m in GEO. It is estimated that there are twice as many non-trackable objects as what is currently being tracked in GEO. The number of objects between 5 mm and 10 cm in LEO is currently estimated at around 600,000 objects [5]. Smaller objects dominate the orbital debris population. Most of these objects are the direct result of satellite disintegration or collision processes [6]. Objects orbiting the Earth can reach speeds of up to 8 km s^{-1} in LEO [7]. At these speeds, even the smallest of objects can cause extensive damage to an active satellite. An indicative example of the damage that can be caused by these projectiles is shown in Figure 1.3.

Objects smaller than 1 cm are harder to detect or track regularly from the ground. At this scale, the data is unreliable and only estimates that are based on statistical models are available [8]. Current estimates put the number of objects smaller than 1 cm to hundreds of millions and those below 1 mm to tens of billions. These estimates can be determined experimentally through impact assessment on returned hardware from space. Analysis of the impact craters can give an estimate for the impact velocity, direction and origin of the projectile [9].

In 1993, one solar panel from Hubble Space Telescope (HST) was returned to Earth for analysis. A total of 3600 impacts were reported on its brittle glass covering the solar array with a surface area of 55 m^2 . Chemical analysis of the

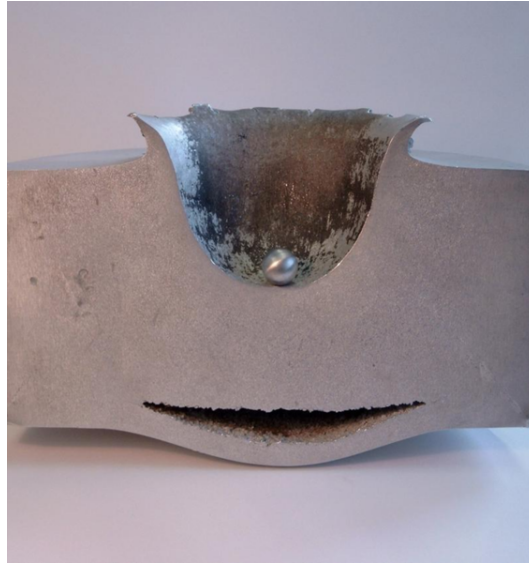


Figure 1.3: Crater left by a hyper-velocity impact emulating the damage caused by a 1.2cm aluminum sphere travelling at typical LEO velocity of 6.8 km s^{-1} (Source: ESA)

crater pits showed that 69 per cent of the object were micro-meteorites, 10 per cent originated from human-made objects, and 21 per cent were not classified [10]. This data suggests that at this scale, human-made objects do not exceed the natural background objects [11]. Mathews et al. (2001) [12] estimate that around 4 t to 7 t of space material enter Earth's atmosphere per day. This contributes to the hazardous environment satellites are operating in.

The orbiting objects are not distributed evenly around the Earth. An analysis of the inclination, periodicity and eccentricity ratio of the catalogued objects can identify regions with a higher density of objects. For instance, objects are found concentrated at orbital inclinations near 65° , 75° , 83° and 99° [13]. As illustrated in Figure 1.4, a maximum in orbital concentration can be observed at particular inclination bands such as the sun-synchronous orbits (inclination of $\sim 100 \pm 5^\circ$), polar orbits (inclination of $\sim 90^\circ$) and orbits at which navigation satellites reside in (inclination between $\sim 55^\circ$ and $\sim 65^\circ$). On the other hand, if one considers the eccentricity of the objects, the distribution is more continuous. Figure 1.5 shows that most of the catalogue objects have near-circular orbits with an eccentricity of less than 0.01. These accumulation regions are of particular research interest as they pose a higher statistical threat than other regions. The likelihood of a collision is highest at locations with the highest resident probability [11].

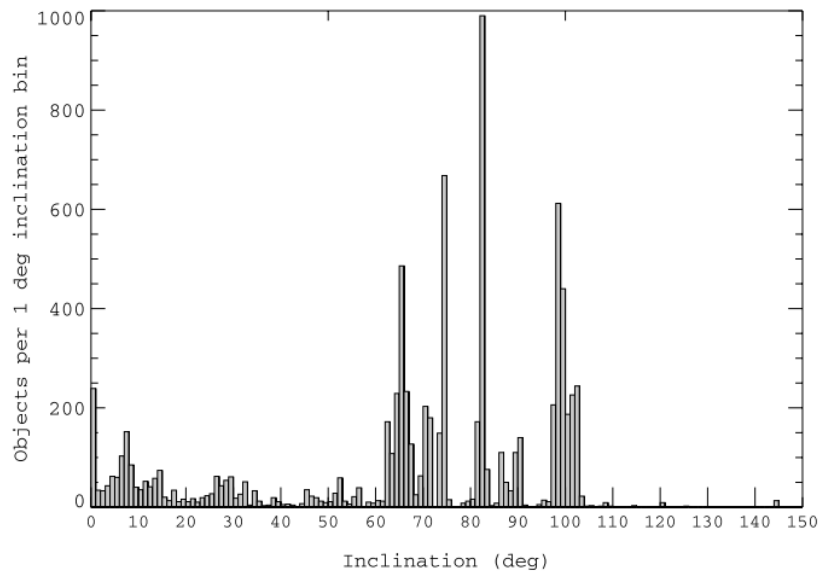


Figure 1.4: A histogram of the catalogue object's inclination with a bin width of 1° [11]

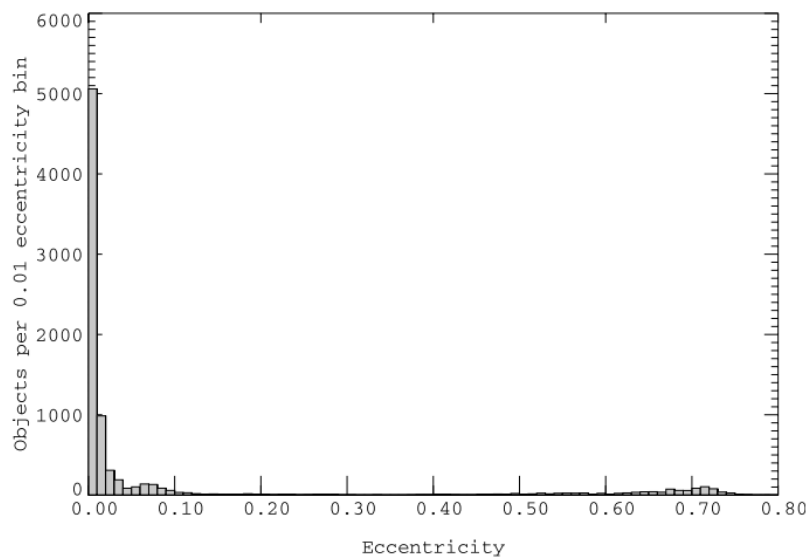


Figure 1.5: A histogram of the catalogue object's eccentricity with a bin width of 0.01 [11]

In 1996, space agencies witnessed the first-ever known on-orbit collision between the French Cerise satellite and an Ariane-1 h-10 upper stage debris [14]. The debris field created by two similar events is manifested in Figure 1.6 as two distinct peaks in the orbital population. The first peak observed is attributed to the intentional destruction of the Chinese Fengyun-1C polar-

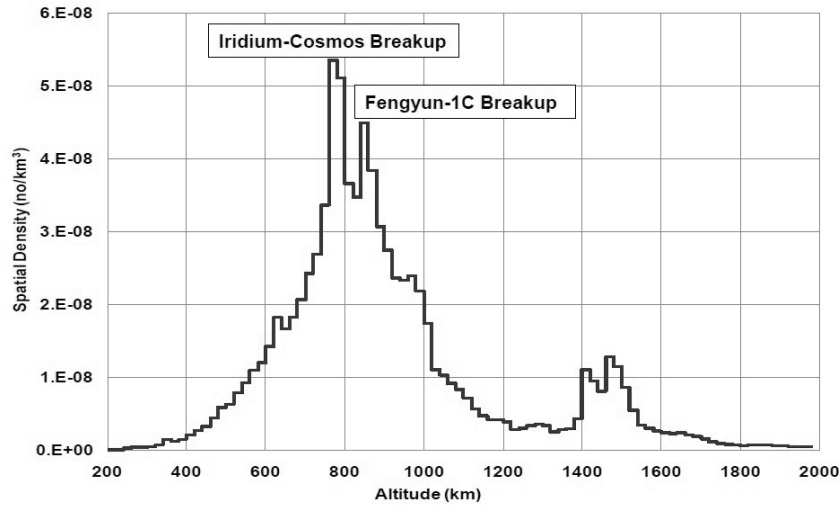


Figure 1.6: A histogram of the catalogue object’s altitude [11]

orbiting weather satellite [15] in 2007. The second peak is attributed to the on-orbit collision between an active 560 kg Iridium-33 satellite with a defunct Russian Kosmos-2251, 900 kg communication satellite in February 2009. The speed of the impact was over 11 km s^{-1} , destroying the Iridium satellite [16].

Nowadays, the space environment in LEO is mostly driven by the commercial sector. In recent years, there have been several announcements of mega-constellations, consisting of a network of thousands of satellites such as Starlink mega-constellation from SpaceX¹. This new constellation, whose initial launch started in 2019, raised fresh concerns on the safety of these constellations in LEO [17].

One can theorise that if no effective measure is taken to control the orbital debris population, the likelihood of further collisions can be expected to increase. In 1978 [18] stated that the uncontrolled debris growth could lead to a self-supporting process of collisional cascade where in-orbit collisions can generate a debris cloud of highly energetic projectiles which in-turn trigger further collisions. Known as the Kessler’s syndrome, this theory predicts that in the long-term, the debris population would decrease in size as the number of collisions between space debris increases. The implication is that if no remedial action is taken, this process can lead to a situation where the risk of a collision in LEO is so high that future crewed and uncrewed space missions will become impractical or dangerous.

¹ www.spacex.com

1.2 Mitigation measures

The increasing risk of orbit collisions has led to a substantial investment in new preventive measures in order to mitigate the proliferation of space debris. In the last decade, there have been several techniques that proposed methods of removing the larger debris directly. However, as yet, no such system is operational [5].

Effective mitigation strategies are essential for satellites in the LEO and GEO regions, which are of most importance due to the unique properties for space activity. The Inter-Agency Space Debris Coordination Committee (IADC) singled out these two orbital regimes as protected regions of outer space. Any space activity in this region should strictly abide IADC space debris mitigation guidelines which were set out to ensure a sustainable and safe future with regards to the generation of space debris [19]. For instance, nowadays, post-mission passivation measures [20] have become standard practice. Furthermore, the orbital lifetime of a spacecraft with a propulsion system can be reduced by lowering its perigee altitude before being passivated [21].

There are no natural cleaning mechanisms to remove orbiting objects in GEO. Unlike objects in LEO, there are no energy-dissipating mechanisms, such as atmospheric drag at this orbital regime [22]. Consequently, collision risks in GEO are reduced by placing retired spacecraft to an IADC-compliant ‘graveyard’ orbit in order to separate them from operational spacecraft in the GEO protection zone [23].

While the risk of collision can be reduced significantly through the above mentioned practices, catastrophic orbital collisions can occur and have occurred in the past. Specialised shielding can protect the spacecraft from sub-centimetre objects [24]. However, currently, there is no effective shielding capable of protecting the spacecraft from a collision with medium to large debris objects [25]. Satellite operators have to routinely assess the probability of a collision of their assets with other objects. For instance, in the case of the International Space Station (ISS), the accurate tracking of objects that are larger than its maximum shield capacity is essential. When the risk of a collision with these objects is high, the ISS can execute evasive manoeuvres [26, 27].

Tracking of space debris objects is vital for the characterisation of the debris environment through direct observations. Measurements provide space

agencies and satellite operators with a deeper understanding of the current environment. Observational campaigns shed light into the space debris growth trends [28] and accumulation regions. This data is presently used both at the mission design phase and in collision risk assessment studies [29]. Additionally, these measurements are also used in the monitoring campaigns of orbital debris re-entries.

These measurements are used to populate orbital debris databases or catalogues detailing the space environment produced by human-made objects. The United States Strategic Command (USSTRATCOM) distributes an extensive data set of orbital debris objects in Two-Line Element (TLE) format. This catalogue is maintained through the observations performed by the US Space Surveillance Network (SSN) [30]. It lists objects in the order of 10 cm in LEO and 1 m in GEO. This information is made available through the SpaceTrack² website through a public API that allows users to download the TLE information of the target objects. The USSTRATCOM is also used to build most of European Space Agency (ESA)'s Database and Information System Characterising Objects in Space (DISCOS)³ catalogue [31].

1.3 Sensors for space situational awareness

Space agencies amalgamate the output of different sensors in order to detect, track and identify both known and unknown orbiting objects. At present, the space environment is determined through both space-borne [32, 9] and ground-based optical and radar systems [33].

At higher perigee altitudes, such as Medium Earth Orbit (MEO) and GEO, optical instruments are typically used given that the sensitivity of optical instruments decreases with the second power of the distance between the instrument and the target. High-altitude objects are tracked using the Ground-based Electro-Optical Deep Space Surveillance (GEODSS) and Maui Optical Tracking and Identification Facility (MOTIF) USSTRATCOM installations. Each facility is a system of three 1 m aperture diameter telescopes and part of the US SSN [34]. Although European and Japanese institutions operate several space

² www.space-track.org

³ www.discosweb.esoc.esa.int

surveillance assets, none of them is being used for the operational maintenance of a catalogue [11].

Optical instruments are dependent on the Sun's illumination of the target object and their performance is susceptible to atmospheric conditions [28]. On the other hand, radar instruments are independent of the Sun's illumination of the targets and are not susceptible to meteorological conditions. Radar instrumentation is often used in the characterisation of the debris environment at lower altitudes. In these methods, the sky is irradiated with a powerful microwave beam. The radiation is reflected back to the receiver by any object that crosses the coverage area of the radar. The reflected signal is used to infer the position, RADAR Cross Section (RCS) and trajectory of the target objects [29]. The strength of the returned echo is inversely proportional to the fourth power of the incident radiation [35], making them most suitable for LEO monitoring.

The US SSN makes use of several dedicated and collateral sensors for the routine tracking of space debris objects. Apart from the operational sensors, there are also experimental instruments which can detect orbital objects to a higher degree of accuracy. Of particular note is the Haystack radar facility located in Lexington, Massachusetts. The system consists of two parabolic dish X-band radars systems. The Haystack Long-Range Imaging Radar (LRIR) (Figure 1.7) is a 36 m mono-static parabolic radar with a 250 kW peak power and having a 0.058° beamwidth. The radar is reported to be capable of detecting sub-centimeter level objects at an altitude of 1000 km [36].

The second facility at Lexington is the Haystack Auxiliary (HAX) 12.2 m mono-static parabolic dish [37]. The radar has a peak power of 50 kW and a 0.10° beamwidth and can provide accurate range and angle measurements of debris greater than 2 cm at a range of 1000 km [36]. Even smaller sized objects are detected by the Goldstone Deep Space Network in the Mojave Desert. The radar can detect 2 mm objects at 500 km [11]. The Goldstone radars (Figure 1.8) are a bi-static X-band system consisting of a 70 m, 450 kW transmitter parabolic antenna (0.02° beamwidth) that is coupled with a 34 m receiving parabolic antenna 500 m away [38, 39].

In Europe, the characterisation of space debris objects is one of the primary objectives of the ESA Space Situational Awareness (SSA) programme. The tracking of space debris objects is done through several sensors in the European network of sensors [29]. In northern Scandinavia, one finds the



Figure 1.7: The Haystack facility in Massachusetts, US



Figure 1.8: The Goldstone radar system in California, US (Source: NASA)

low frequency European Incoherent Scatter Scientific Association (EISCAT)⁴ scatter radar. The primary research goal of the facility is high-latitude atmospheric and ionospheric research. However, it was also shown to be able to perform space debris observation campaigns in conjunction with the standard ionospheric measurements. The EISCAT Ultra High Frequency (UHF) radars located in Tromsø and Svalbard were used for beam park experiments of space debris objects. The Tromsø radar operates at 920 MHz and uses a 1.6 MW peak power transmitter. On the other hand, the Svalbard radar is a 32 m parabolic dish antenna that operates at 500 MHz with a peak transmitting power of 0.7 MW [40]. Both of these radars have been used in the characterisation of in-orbit events such as the debris field created by the Chinese anti-satellite incident [41, 42] and the Iridium-Cosmos collision [43]. In a 5000 h observation campaign, detections of 3.5 cm objects at a range of 700 km to 1000 km were reported using the EISCAT Svalbard radar [41]. In 2017, studies showed that a multi-static radar composed of the various radar installations within the EISCAT network, called EISCAT-3D [44], can be used to obtain an object's trajectories and instantaneous position and velocity vectors [45].



Figure 1.9: The 34 m diameter parabolic reflector at the TIRA radar facility in Wachtberg, Germany (Source: Fraunhofer Institute for High Frequency Physics and Radar Techniques (FHR))

The French Grand Réseau Adapté à la Veille Spatiale (GRAVES) radar system (Figure 1.10) is the only space debris monitoring system outside the US SSN and Russian Russian Space Surveillance System (SSS) which maintains an

⁴ www.eiscat.se



Figure 1.10: The GRAVES radar system in Dijon, France (Source: Office National d'Etudes et de Recherches Aérospatiales (ONERA))

independent catalogue. Owned by the French Department of Defence (DoD), the system consists of Very High Frequency (VHF) Continuous Wave (CW) transmitter and a planar 15 m by 6 m phased antenna arrays acting as receivers. The quoted resolution of the system, whose operational tests started in 2001, is of the order of 1 m at an altitude of 1000 km [46].

Wachtberg is home to the German Tracking and Imaging Radar (TIRA) system (Figure 1.9), of the FHR. This mono-pulse radar system consists of an L-band, 2 MW transmitter for tracking and a Ku-band, 13 kW transmitter for Inverse synthetic aperture radar (ISAR) imaging (0.50° beamwidth). The quoted detection threshold of the system is that of ~ 2 cm at a range of 1000 km [47]. This sensitivity can be enhanced in bi-static experiments with the TIRA system acting as a transmitter and a 100 m radio telescope located in Effelsberg acting as a receiver. In these experiments, detections of objects as small as 1 cm at a range of 1000 km were reported [48]. Other European radar systems worth mentioning are Ukraine's Evpatoria dish antenna and the French's Armor system deployed on the Monge tracking ship. An exhaustive list of experimental and operational radar facilities for SSA is given in [11] and [5].

Observational facilities and space surveillance networks monitor a fraction of the space debris population. Thus, the introduction of new high sensitivity instrumentation is paramount to the better characterisation of the space environment. Apart from building new high sensitivity instruments, one of the research missions of the ESA SSA programme is to adapt existing facilities for the monitoring of orbital debris. As part of this endeavour, the Istituto Nazionale di Astrofisica (INAF) in collaboration with the University of Malta and the Politecnico di Milano embarked on an ambitious project to upgrade one of INAF radio telescope for use in SSA. The aim of this new facility was to establish the first Italian space surveillance radar facility within the ESA SSA network.

1.4 Conclusion

The space-age brought with it new challenges for the existing and future ventures in space. One of the more prominent issues is the proliferation of orbital debris as a consequence of human activity in space. The density of these objects was shown to be highest in the lower altitudes such as in LEO. This commercially sensitive orbit is predicted to become increasingly more congested with the advent of new mega-constellations. As the number of Resident Space Object (RSO) increase, so does the risk of a catastrophic collision with an active satellite or human-crewed mission.

The issues mentioned above highlight the need for new high-sensitivity instrumentation that can monitor, and subsequently catalogue, this ever-growing list of objects. An accurate characterisation of the space environment is paramount to the successful implementation of any space debris mitigation strategy. Nowadays, cutting-edge US and Russian facilities are actively monitoring the space environment. In the last couple of decades, European institutions have also been enhancing their capability for space situational awareness. This study presents the work put into the realisation of one of the latest space debris monitoring radars. The objectives of this project are laid out:

- Investigate the applicability of the Northern Cross (Bologna, Italy) radio telescope as the receiver component for a new bi-static radar that is dedicated to the monitoring of the space environment in LEO.

- Characterisation of the radar's multi-beam receiver's radiation pattern.
- Design and develop a new data processing backend for the radar's receiver that can process the incoming antenna data in real-time.
- Development of new algorithms that are able to detect faint radar echoes reflected off high-velocity RSO's crossing the instrument's radar coverage.

The aforementioned objectives are addressed in the ensuing chapters. The problem statement and the motivation behind the introduction of new European SSA monitoring facilities were outlined in this chapter. In the next chapter, the receiver of this new radar facility is described in detail. This is followed by the design considerations that were put into the development of a novel data processing system for this receiver. Chapter 4 describes the detection algorithms that were used to infer the Doppler and trajectory information of the target objects. In the fifth chapter, the results obtained during several observations, are presented. Finally, a reflection on the current progress and the future direction of this study are discussed in the last chapter.

Chapter 2

Space Situational Awareness using the BEST-II phased array

Since the inception of the European SSA Programme in 2009, SSA activities have benefited from a 200 million Euro budget from the financial participation of 19 member states. The Space Surveillance & Tracking (SST) segment of this program aims to establish an independent SST data acquisition and processing capability in order to meet the increasing demand for larger, cross-national instrumentation for SST [49]. Apart from the design and construction of new SST monitoring assets, existing European national assets are also considered. The aim is to upgrade these systems for their use in space surveillance [50].

In Italy, INAF has been investigating several possible radar setups at the Medicina radio astronomical station since the beginning of the programme. These studies were part of the Italian space debris research program and funded by Italian Space Agency (ASI). An extensive review of the work done within this program can be found in [51] and [6]. The facility is located in Medicina near Bologna, Italy. It hosts two main receiving antennas that are currently dedicated to astronomical research in the radio regime. The first instrument is a 32 m diameter parabolic dish which operates from 1.4 GHz to 22 GHz. In 2007, this parabolic antenna was used in several space debris detection tests. These observation campaigns were done in bi-static mode with the parabolic dish acting as the receiver and the RT-70 parabola in Evpatoria, Ukraine acting as the transmitter. The system was shown to be capable of detecting small-sized debris in LEO and MEO [52].

The second instrument at Medicina is the Northern Cross shown in Figure 2.1. This chapter investigates the use of an upgraded part of this instrument

for its use as a receiver for a bi-static radar. This instrument is described in detail in the next section.

2.1 The Northern Cross

The Northern Cross radio telescope is a T-shape array which operates at the UHF band (408 MHz) with a bandwidth of approximately 2.5 MHz. The main characteristics of the instrument are summarised in Table 2.1. It is composed of two branches or arms that are perpendicular to each other. One arm is aligned in an East-West (E-W) direction while the other is aligned to the North-South (N-S) direction. The E-W arm is a 564 m long, 29.4 m wide cylindrical parabolic reflector having a total collecting area of 16 600 m² [50].

Antenna pointing	Declination only
Collecting area	27 400 m ²
Frequency bands	UHF
Beam N-S	2°
Beam E-W	60°
Polarization	Single

Table 2.1: The system specification of the Northern Cross radio telescope [28]

The N-S arm is composed of 64 parallel parabolic-shaped cylindrical antennas that are spaced 10 m apart. Each antenna is 22.6 m long by 7.5 m wide and is composed of 64 dipoles for a total of 4096 receivers [28]. In total, the N-S arm has a collecting area of 10 800 m² [50].

Thus, if both arms of the Northern Cross are considered, the total collecting area of the instrument is 27 400 m². This makes the Northern Cross the largest UHF-capable antenna in the Northern hemisphere. World-wide, this is second only to the Arecibo Observatory in Puerto Rico [50]. The instrument can point at objects that transit over the local celestial meridian given that it is mechanically steerable in declination only [28]. The array has two elevation limits for its mechanical pointing. In the North pointing configuration, the array can be steered from 22.5° to 90°. On the other hand, in the South pointing configuration, the elevation angle can range from 90° to 17° [53].

In 2010, Montebugnoli et al. [28] stated that an upgraded Northern Cross is an ideal instrument for the tracking of satellites and debris larger than 6 cm in size. At the operating frequency of 408 MHz, the instrument is characterised



Figure 2.1: The Northern Cross in Medicina, Bologna Italy.

Source: www.jodrellbank.manchester.ac.uk

by a large Field of View (FoV) of 2° (N-S) to 60° (E-W). The authors report that the FoV can be populated with up to 46,000 beams, 4 min by 4 min each. As the target object crosses the field of view, a number of beams are illuminated. Simulations of the proposed system show that 85% of the catalogued objects within the USSTRATCOM can be detected. A detection of 80% of the catalogued objects is still obtained if the FoV is halved [28].

The Northern Cross has been engaged in two important radio-astronomical projects: the Square Kilometre Array (SKA) [54] and the Low Frequency Array (LOFAR) [55]. As part of the Square Kilometre Array Design Study (SKADS) framework, a section of the Northern Cross was upgraded to suit the needs of these projects. These upgrades consisted of the installation of new low-noise receivers with a high-dynamic range. It also included the installation of new vector modulators/mixers and low-cost digital optical links [56, 57].

This re-instrumentation endeavour, called Basic Element for SKA Training (BEST) [58, 59], was split into three phases. The first phase, the BEST-1, consisted of the upgrade of a single parabolic cylinder along the N-S arm [60]. This system has been in operation since 2004. The second phase of this instrument is discussed in the next section.

2.2 The BEST-II phased array

The BEST-2 array, shown in Figure 2.2, is a UHF-band radio telescope operating at a band of 16 MHz centred at 408 MHz. It consists of a set of eight East-West oriented cylindrical concentrators having a total collecting area of 1411 m². Each cylinder has a reflecting surface made of 430 parallel steel wires of 0.5 mm that are placed 2 cm apart. The feed consists of 64 $\lambda/2$ dipoles that are situated at the focal line of the primary reflector. The elements are critically spaced by half the wavelength (0.345 m) to minimise grating lobe effects [59]. A flat sub-reflector is placed behind the focal line to increase the efficiency of the cylinder [60]. The specifications of the array are summarised in Table 2.2.



Figure 2.2: The eight East-West cylindrical concentrators making up the BEST-2 array within the Northern Cross. Source: www.med.ira.inaf.it

Operations such as phase-shifting or analogue-to-digital conversion are too expensive to implement for each individual element. Thus, in practice, a compromise is found whereby the elements are grouped into sub-arrays [62]. The BEST-2 array makes use of four low noise receivers (sub-array) that are in-

Total Collecting Area	1411.2 m ²
Total Effective Area (A_{eff})	1001.95 m ²
Receiver Temperature	51 K
System Temperature (T_{sys})	86 K
A_{eff}/T_{sys}	11.65 m ² K ⁻¹
Longest Baseline (N-S)	70 m
Longest Baseline (E-W)	17 m
Radio Frequency (RF) band	400 MHz to 416 MHz
Total analogue channels	32
Primary FoV (DEC, 408 MHz)	5.7°
Primary FoV (RA, 408 MHz)	6.6°

Table 2.2: System specification of the BEST-2 array [61]

stalled at the focal line of each cylinder. Each receiver combines the signals from 16 dipoles using a hierarchical, analogue, beamformer that result in four analogue sub-arrays per cylinder. Hence, the array consists of a total of 32 elements that are arranged in a 4×8 grid [60]. Collectively, these receivers make up what is referred to as the BEST-2 phased array.

The signals received from the receivers are combined in order to increase the overall gain and Signal-to-Noise Ratio (SNR) of the instrument relative to that of a single element. As the aperture size of the array is increased, the width of the main lobe radiation pattern decreases [63] to the point that a single narrow pencil-like beam is generated. Such a narrow beam is desirable in tracking applications [64].

The basic principle behind phased arrays can be explained by considering a planar wave front, of wavelength λ_0 , incident on a linear array consisting of M elements, separated by a distance d . The signals, incident at an angle θ , will arrive at different times across the array elements. An antenna element m will experience a phase difference ϕ_m with respect to the first element. This phase difference is given by,

$$\phi_m = k_0(M - m)d \sin(\theta) \quad (2.1)$$

where,

$$k_0 = \frac{2\pi}{\lambda_0} \quad (2.2)$$

The signal $S_m(\theta)$ received at an element m located at $x_m = (M - m)d$ can be written as,

$$S_m(\theta) = S_e(\theta) \exp(jk_o x_m \sin(\theta)) \quad \text{for } m = 1, 2, \dots, M \quad (2.3)$$

Where $S_e(\theta)$ is the complex radiation pattern of the elements also known as the element factor. The elements are assumed to have a uniform amplitude distribution. The response of the array $S(\theta)$ can be obtained by summing the received signals from the individual elements,

$$S(\theta) = \sum_{m=1}^M S_m(\theta) \quad (2.4)$$

$$= S_e(\theta) \sum_{m=1}^M \exp(jk_o x_m \sin(\theta)) \quad (2.5)$$

The array output can be alternatively written in terms of the element factor $S_e(\theta)$ and the Array Factor (A_F) defined as,

$$A_F(\theta) = \sum_{m=1}^M \exp(jk_o x_m \sin(\theta)) \quad (2.6)$$

Such that,

$$S(\theta) = S_e(\theta) A_F \quad (2.7)$$

Thus, the combined radiation pattern for an antenna array consisting of identical elements and oriented in same direction, is simply the radiation pattern $S_e(\theta)$ multiplied by the Array Factor (A_F).

The radiation pattern of a phased array can be electronically steered such that, in the case of a receiving antenna, it is made more sensitive to a particular direction [65]. This makes it possible for the BEST-2 array to be steered electronically in both the elevation and the azimuth plane.

The direction of maximum reception of the array can be altered by changing the phase of the received signal across its elements. This is the principle behind antenna or beam steering. In beam steering, the received signals $S_m(\theta)$ are multiplied by a steering vector $\vec{v} = \exp(j\psi_m)$ such that when the signals are added, they combine coherently towards a particular direction θ_0 . Thus, the array factor becomes,

$$A_F(\theta) = \sum_{m=1}^M \exp(j[k_0(M - m)d \sin(\theta) + \psi_m]) \quad (2.8)$$

Thus, if the phase taper is,

$$\psi_m = -k_0 x_m \sin(\theta_0) \quad \text{for } m = 1, 2, \dots, M \quad (2.9)$$

the array factor can be expressed as,

$$A_F(\theta) = \sum_{m=1}^M \exp(jk_0 x_m [\sin(\theta) - \sin(\theta_0)]) \quad (2.10)$$

Hence, phasing the antenna elements according to the beam-pointing direction θ_0 will result in an array factor which reaches a maximum at an angle $\theta = \theta_0$, as desired. Put differently, the beam is said to be steered towards the angle θ_0 . For a planar phased array of K by L elements, such as the BEST-2 array, the radiation pattern in (θ, ϕ) can be shown to be the product of the element factor $S_e(\theta, \phi)$, and the two linear array factors $A_{F1}(\theta, \phi)$ and $A_{F2}(\theta, \phi)$ in the x and y direction respectively [63, 66],

$$S(\theta, \phi) = S_e(\theta, \phi) A_{F1}(\theta, \phi) A_{F2}(\theta, \phi) \quad (2.11)$$

In this case, the phased array factor $A_F(\theta, \phi) = A_{F1}(\theta, \phi) A_{F2}(\theta, \phi)$ is given by,

$$A_F(\theta, \phi) = \sum_{m=1}^M \sum_{n=1}^N \exp(jk_0 \xi_{xm}) \exp(jk_0 \xi_{yn}) \exp(j\psi_{mn}) \quad (2.12)$$

where,

$$\xi_{xm} = x_m \sin \theta \cos \phi \quad (2.13)$$

$$\xi_{yn} = y_n \sin \theta \sin \phi \quad (2.14)$$

and x_m and y_n is the position of the mn^{th} element and ψ_{mn} is the phase taper that is applied on the incoming signals such that the maximum array radiation occurs at $(\theta, \phi) = (\theta_0, \phi_0)$. In general, the position of the mn^{th} element from the origin can be expressed in terms of the position vector \vec{r}_{mn} ,

$$\vec{r}_{mn} = x_m \hat{x} + y_n \hat{y} \quad (2.15)$$

Therefore,

$$\vec{k} \cdot \vec{r}_{mn} = k_0 \hat{r} \cdot \vec{r}_{mn} = k_0 x_m \sin \theta \cos \phi + k_0 y_n \sin \theta \sin \phi \quad (2.16)$$

Similarly the phase term ψ_{mn} can be expressed as,

$$\psi_{mn} = -\vec{k}_0 \hat{r}_0 \cdot \vec{r}_{mn} = k_0 x_m \sin \theta_0 \cos \phi_0 + k_0 y_n \sin \theta_0 \sin \phi_0 \quad (2.17)$$

Substituting the terms, the array factor can be written more compactly in terms of the wave vector \vec{k} steered towards the incident radiation with a wave-vector \vec{k}_0 [67, 66],

$$A_F(\vec{k}) = \sum_{m=1}^M \sum_{n=1}^N \exp(j(\vec{k} - \vec{k}_0) \cdot \vec{r}_{mn}) \quad (2.18)$$

Thus, the complete radiation pattern for a phased array whose elements are arranged in a grid is given by,

$$S(\vec{k}) = S_e(\vec{k}) A_F(\vec{k}) = S_e(\vec{k}) \sum_{m=1}^M \sum_{n=1}^N \exp(j(\vec{k} - \vec{k}_0) \cdot \vec{r}_{mn}) \quad (2.19)$$

The element radiation pattern $S_e(\vec{k})$ can be obtained either empirically or through simulation. The next section presents the radiation pattern for an element within the BEST-2 array that was obtained through simulation. This pattern is ultimately used to produce the complete radiation pattern of the array.

2.2.1 An electromagnetic model of the BEST-II array

A complete characterisation of the resulting radiation pattern can be achieved through a full electromagnetic simulation software packages. Computer Simulation Technology Studio Suite (CST)¹ is an electromagnetic simulation software that can simulate the electromagnetic behaviour of an antenna design.

In this work, a single parabolic cylinder of the BEST-2 array was modelled in CST. The individual steel wires acting as the antenna's reflector were modelled as a single, solid, sheet of metal in order to simplify the simulation. This reduced the complexity of the simulation. Mutual coupling effects between the dipoles were modelled by introducing all the 64 dipoles within a cylinder. The dipoles, separated by a distance of 0.345 m were put at the focal length

¹ www.3ds.com

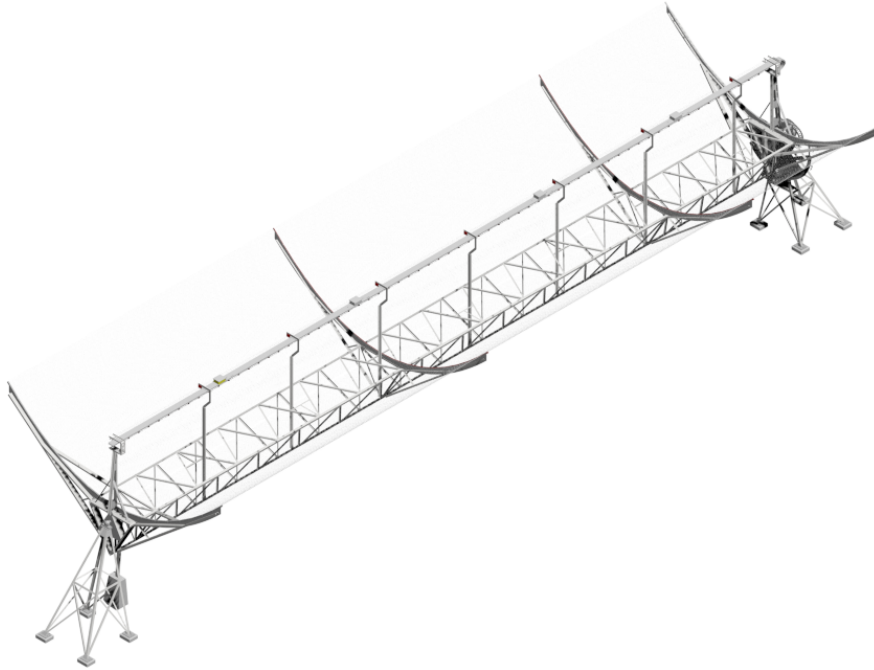


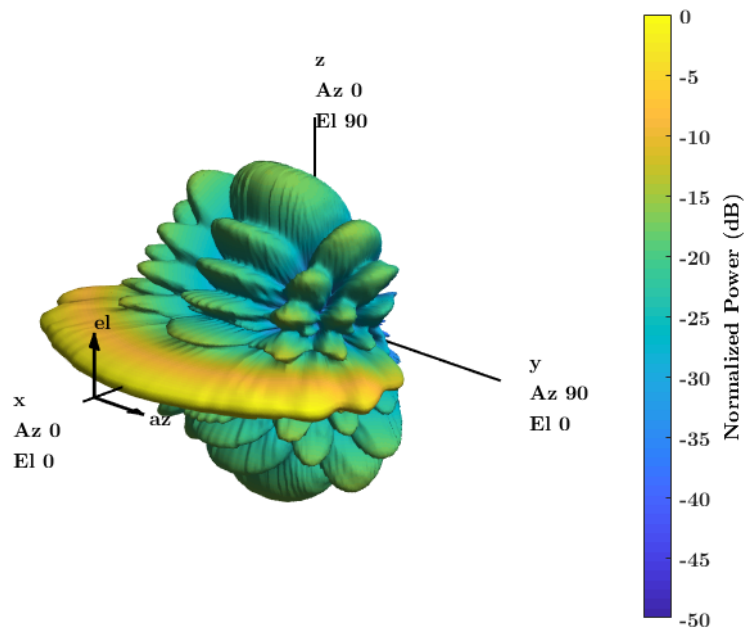
Figure 2.3: A 3D model of an element of the BEST-2 array (Source: M. Schiaffino at INAF)

of the reflector. A rectangular sheet of metal was placed behind the dipole elements to emulate the physical sub-reflector installed. Care was taken to ensure that the measurements are as precise as possible. Precise measurements of the parabolic reflector were obtained from a Computer-Aided Design (CAD) model developed by Marco Schiaffino at INAF. This CAD model is shown in Figure 2.3.

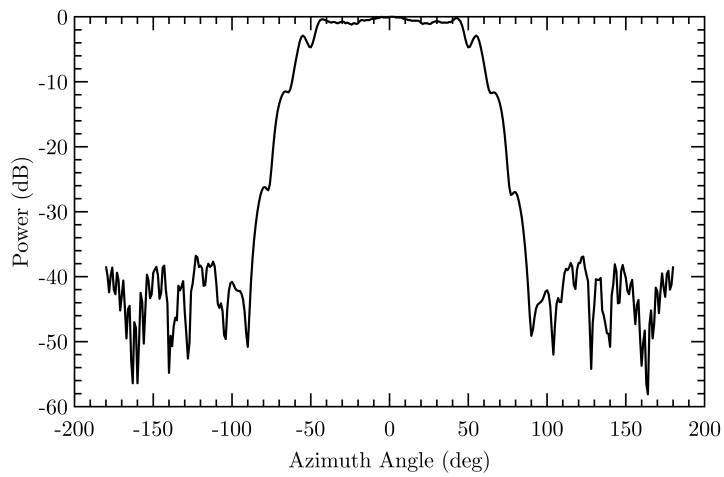
The ensuing discussion will detail how the electromagnetic simulation results obtained in CST were used to build a complete model for the BEST-2 phased array. The electromagnetic results from this simulation were exported to CSV file and subsequently post-processed in such a way that they could be imported and used by MATLAB's Phased Array Toolbox².

The simulated far-field 3D pattern of an ideal half-wavelength dipole placed in the middle of the reflector is shown in Figure 2.4a. The corresponding power pattern in the azimuthal, ϕ and elevation, θ , planes are shown in Figure 2.4b and Figure 2.4c. The reflector enhances the directivity of the antenna element when compared to that of a conventional dipole antenna.

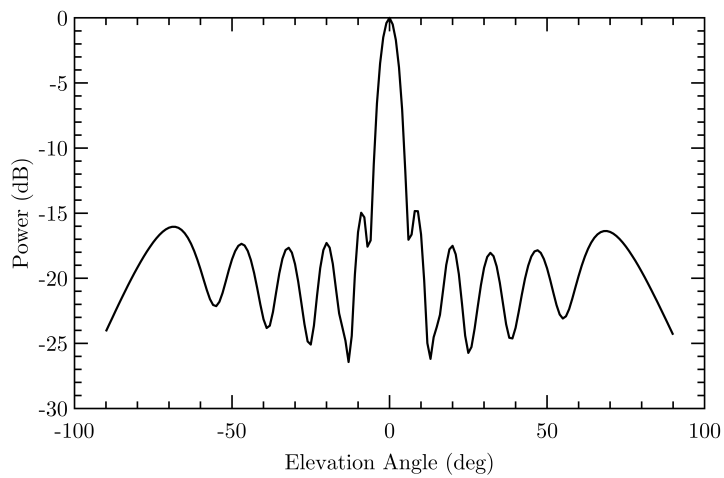
² www.mathworks.com/products/phased-array.html



(a) 3D representation



(b) Azimuthal plane cut



(c) Elevation plane cut

Figure 2.4: A element radiation pattern of a dipole element at the centre of a parabolic reflector of the BEST-2 array

The BEST-2 sub-array, or receiver, was assumed to consist of 16 identical dipole antennas having the same response. The pencil-shaped power pattern of the sub-array is shown in Figure 2.5a. The corresponding azimuth and elevation cuts of the sub-array's power pattern are illustrated in Figure 2.5b and Figure 2.5c. One can note that the gain of the combined elements is enhanced and the directivity of the element is improved as the beamwidth narrows in the plane parallel to the focal line.

The beam pattern of the full BEST-2 array is realised by aggregating the response from 32 receivers spread across eight cylinders. The realised pattern for the BEST-2 phased array is shown in Figure 2.6. The gain of the array is calculated to be 43.59 dB at broadside while the side-lobe level of the array is -13.45 dB relative to the main lobe. The Half-Power Bandwidth (HPBW) along the E-plane is 1.63° and 0.45° along the H-plane. One may also note that the gain of the synthesised beam is governed by a tapering action of the element pattern. This tapering effect attenuates the radiation pattern in the direction of the array's FoV boundary.

One may note the emergence of grating lobes in the Elevation cut. Grating lobes are the aliasing effect introduced as a consequence of the array geometry [68]. These maxima are not desirable in radar applications since these introduce ambiguities in the detection. A radar's performance is hindered by the fact that it is not able to distinguish between a detection in the main lobe with that inside of a grating lobe.

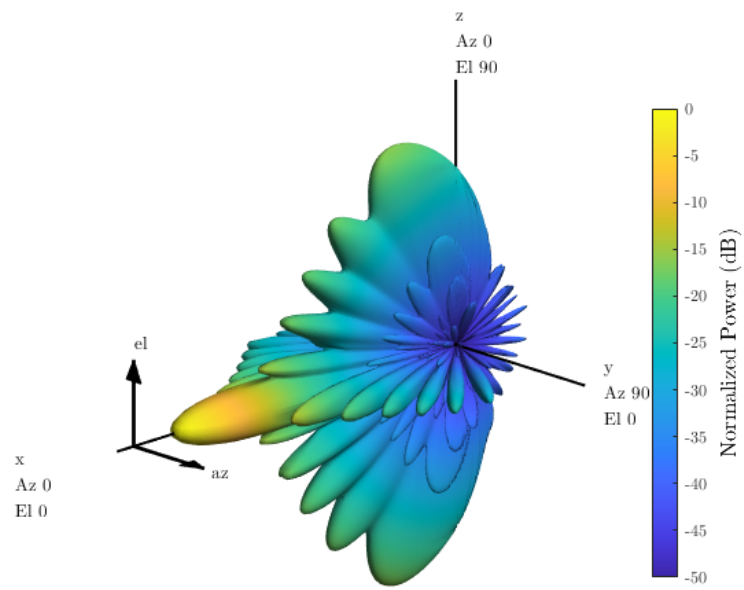
Grating lobes are unavoidable in the BEST-2 array given that the separation distance d between the antenna elements (along the South-North direction) is greater than $\lambda/2$ (for the end-fire case). A maximum in the radiation pattern of an antenna is expected at an angle θ which satisfies,

$$\frac{d}{\lambda}(\sin \theta - \sin \theta_s) = m, \quad m = 0, \pm 1, \pm 2 \quad (2.20)$$

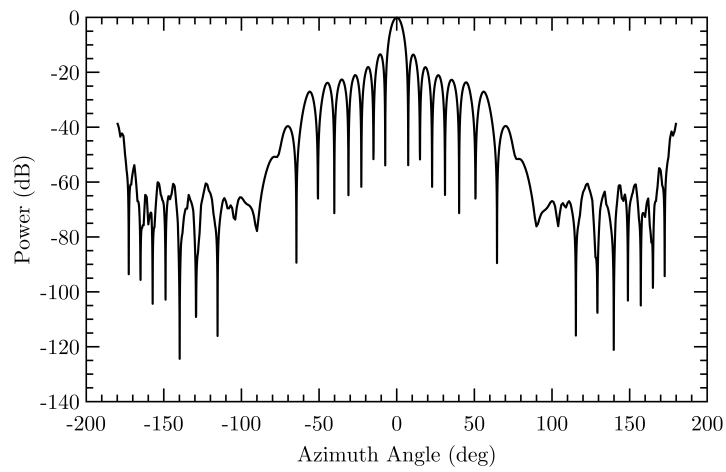
where θ_s , also known as the scanning angle, is the angle of the array at which maximal directivity occurs. Thus, at broadside, a beam maxima should occur at an angle θ [64].

$$\theta = \sin^{-1} \left(\frac{m\lambda}{d} \right) \quad (2.21)$$

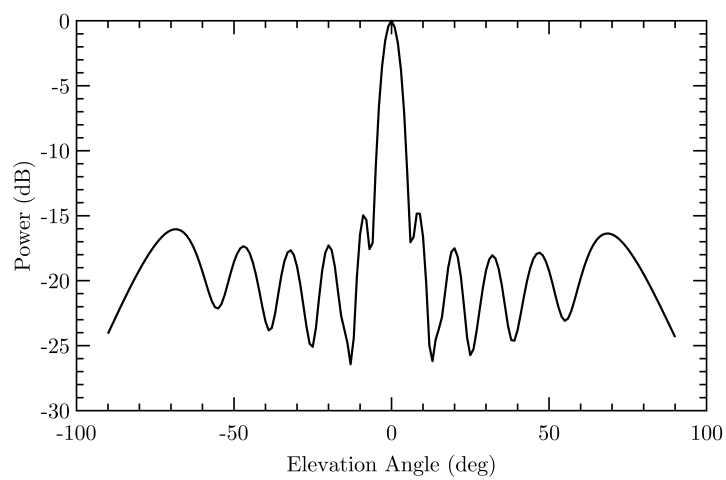
In the case of the BEST-2 array operating at a frequency of 410 MHz (the chosen carrier frequency for space surveillance), the separation distance is 8λ



(a) 3D representation

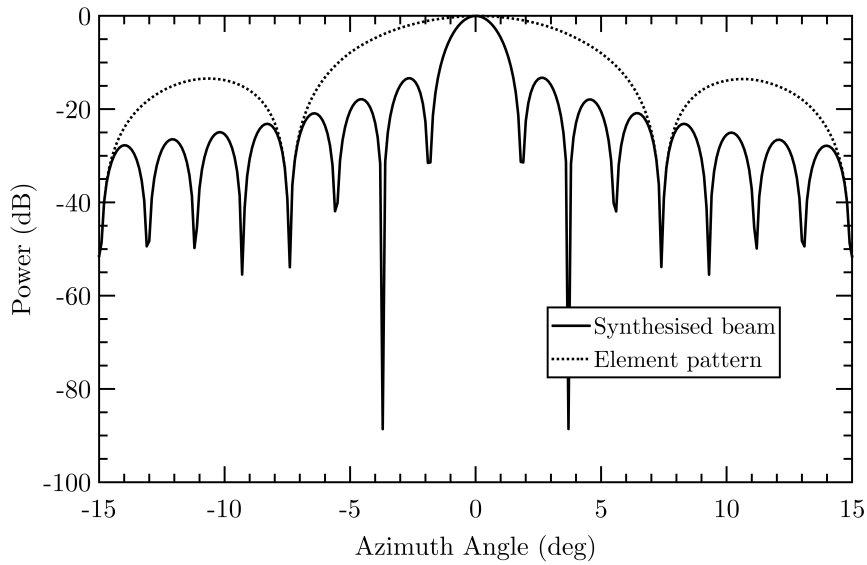


(b) Azimuthal plane cut

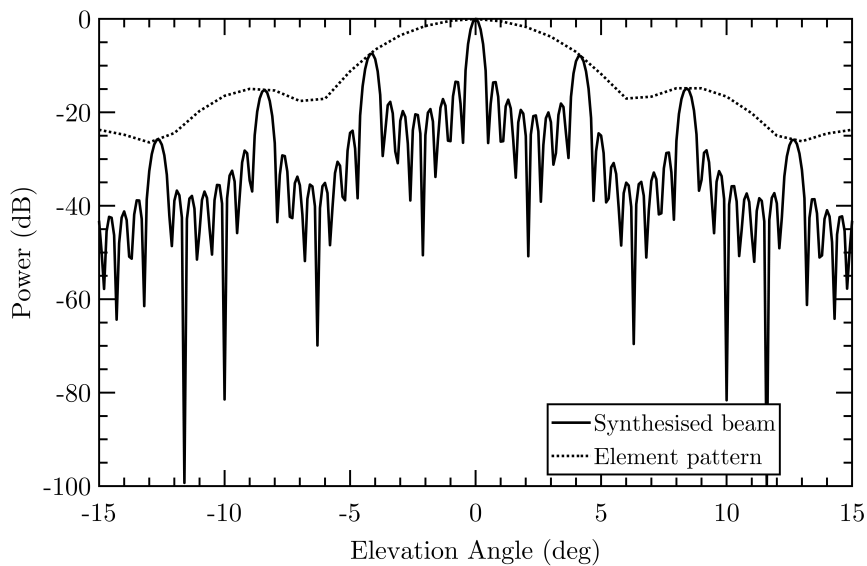


(c) Elevation plane cut

Figure 2.5: The simulated beam pattern for a sub-array receiver in the BEST-2 phased array



(a) Azimuthal plane cut



(b) Elevation plane cut

Figure 2.6: The simulated beam pattern of the BEST-2 phased array

and 13.6λ in the H-plane and E-plane respectively. The first grating lobe is expected to be 4.2° in H-plane and 7.2° in the E-plane away from the main lobe.

The discussion thus far has investigated the apparent radiation pattern of the array when the target object is at zenith. As the angle between the target and the array changes, so does the apparent distance between the cylinders. Assuming the hour angle between the target and the receiver is very close to

zero, the apparent change in cylinder distance is equivalent to $d \sin(\theta)$ where θ is the elevation angle between the array to the target source. Thus at the zenith ($\theta = 90$ deg), it will be equivalent to d as required.

2.2.2 Beam steering

The beam pattern for the BEST-2 array can be pointed in any direction by applying the correct steering vector. Figure 2.7 illustrates the array response as it is steered to 1.5° and 3.2° in azimuth, respectively. One may note that as the beam is steered off the broad-side, the shape of the array's response changes substantially. While the main beam is correctly steered towards the specified angle, quantisation lobes start to appear in the array response.

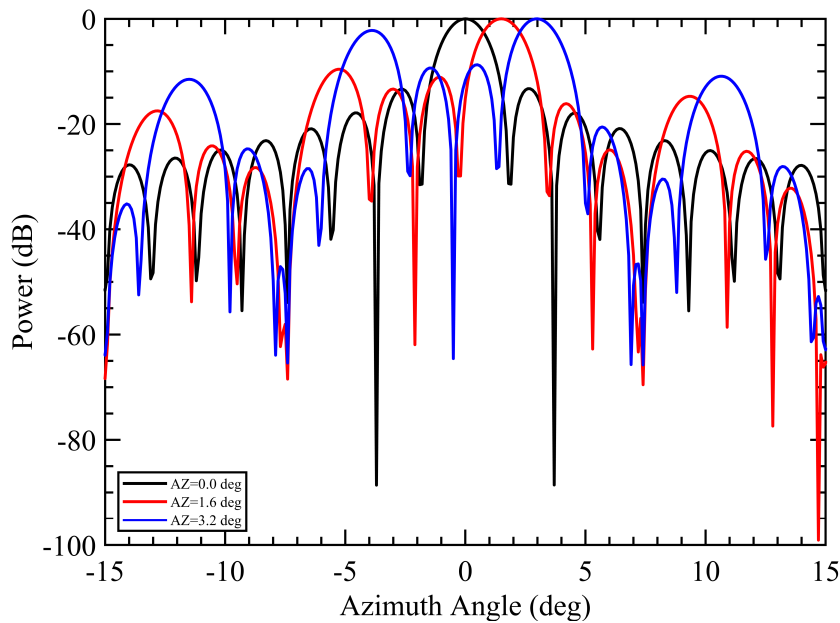


Figure 2.7: Steering of the main beam 1.5° and 3.2° away from broadside in the azimuth plane. Quantisation lobes are clearly visible at azimuth = 3.2°

Quantisation lobes are a consequence of applying the steering weights at the subarray level. The same discrete phase shift is applied across all elements within the sub-array instead of using a linear progressive phase shift where each element has its own correction [62]. This results in periodic phase and amplitude errors across the sub-array. These errors are highly correlated and result in the large, well-defined peaks. These peaks are known as quantisation lobes [68]. Apart from spatial aliasing, quantisation affects the accuracy of the

beam pointing [69]. It can be noted that this effect becomes more severe as the steering angle is increased.

Figure 2.8 shows the angular deviations between the generated beam pointing and the desired angle. The resultant pointing of the generated beam is determined by the azimuth, elevation angle at which the maximum gain is recorded. As expected, the difference becomes more significant as the beam is steered farther away from the azimuth direction. Such an error, which can rise to 0.2° at an azimuth offset of just 3° , is substantial and is not acceptable for the precise determination of a target's orbit. It can be shown that this phenomenon is not present when the beam is steered in the elevation direction and is independent of the declination of the array. The current understanding is that this deviation is attributed to the prevalence of quantisation lobes. Further reading into the pointing errors introduced by phase shift quantisation effects can be found in [70, 68].

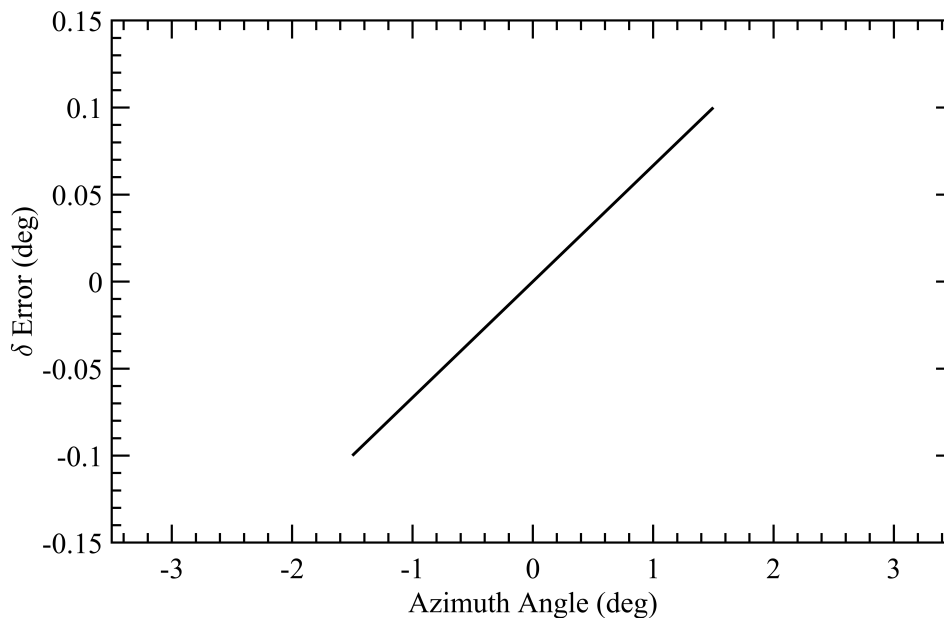


Figure 2.8: Angle deviation as a function of the azimuthal pointing away from broadside

Quantisation lobes can be compensated for by adding phase shifters behind each antenna element within the sub-array. Phase can be changed by altering the permeability using a ferrite phase shifter [66]. However, placing a phase shifter behind each element increases the costs and complexity of the array. In the absence of these phase shifters, one can alternatively try to model these

pointing errors. As shown in Figure 2.8, these errors can be quite predictable. Hence, they can be accounted for if an accurate model of the BEST-2 array is available. This highlights the need for such a model in order to understand the deviations from the nominal pointing direction.

This analysis suggests that the beam pointing errors can be minimised if the steering of the beams is restricted to a few degrees away from the broadside angle in azimuth. Furthermore, grating lobes effects in the N-S direction can also be reduced if the beams' steering in the Elevation (EL) direction is kept below 3° . However, the coverage area of the multi-pixel is reduced. This means that a balance needs to be found between the precision of the beam's pointing and the maximum coverage area. In Chapter 3, these considerations will be used to generate an optimal beam configuration for the detection of space debris.

The model mentioned above can be validated against the response of the array to an astronomical radio source. Such a technique is a standard practice that is used to verify the radiation pattern of the instrument. As the source passes over the array, the processing backend introduced in the following chapter is used to beamform the incoming array signals. The array response in time is converted in terms of angle such that it could be compared with the model's array response, as shown in Figure 2.9.

One can observe the high level of agreement between the data obtained during a transit of Cassiopeia A and the modelled antenna response. This agreement can also be seen at the sidelobe levels, where the deviation is less than 0.1 dB. However, this agreement is less pronounced for the beams that are steered farthest from broadside. While the presence and general shape of the quantisation lobes is predicted correctly, their position and relative strength is not. The implication is that the electromagnetic behaviour of the BEST-2 array is still not completely understood. This could be due to the fact that the elements do not behave identically. In reality, tapering effects at the edge of the parabolic cylinder mean that the element radiation pattern changes depending on its position on the parabolic cylinder.

The results seem to indicate that albeit the agreement between the model and observed data is favourable, the verification of the actual radiation pattern in-situ is imperative for a more precise characterisation of the array. Moreover, only the azimuthal plane could be compared using this method. Ideally, the radiation pattern is wholly characterised in both E and H planes. Given that

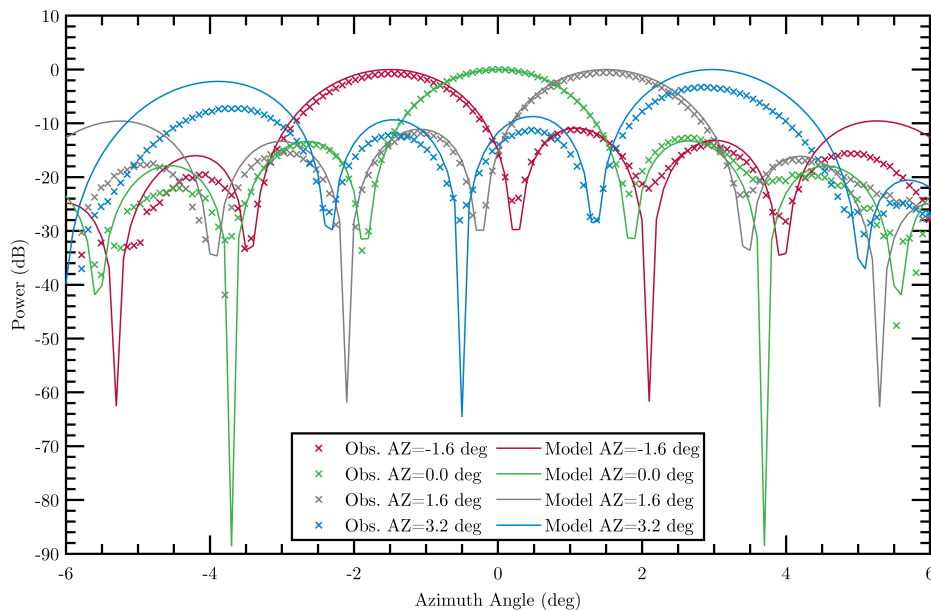


Figure 2.9: A comparison of the response of row of four beams from an observation of Cassiopeia A against the simulated beam pattern of the BEST-2 array

this is difficult to achieve using astronomical radio sources, researchers have been experimenting with the use of artificial sources as verification systems. The empirical verification of the radiation pattern of large radio antennas such as the BEST-2 radio telescope is a challenging problem.

Consequently, a new antenna verification system, called ChopPy, was developed. ChopPy is a new and inexpensive antenna verification solution that makes use of an Unmanned Aerial Vehicle (UAV) in order to characterise the radiation pattern of radio antennas. Unlike existing methods, the system was designed to acquire the data in real-time whilst the artificial RF source is still airborne. The system is presented in Appendix A.1.

2.3 Calibration

Radio astronomical instruments, such as the BEST-2 array, are subjected to several sources of errors that hinder the quality of the measurements. These sources of errors, which can either be inherent or independent of the instrument, can attenuate the strength of the incoming signal, distort the beam pattern of the instrument or introduce a systematic error in the measurements

[71]. These errors manifest themselves as gain and phase differences between the receiving elements of a phase array. Environmental conditions such as temperatures can also cause variations in amplitude in phase. Moreover, tropospheric or ionospheric effects may cause additional phase delays.

The ionosphere is a region of the upper atmosphere that is characterised by a significant number of ionized particles, produced primarily by the ultraviolet light from the sun, that affect the propagation of radio signals [64]. The propagation path of the electromagnetic waves through this dispersive medium is thus probabilistic in nature and varies with time [72]. However, in the case of the BEST-2 array, the FoV is small enough such that it can be assumed that all receiving elements experience the same propagation conditions. This makes it possible to calibrate the array on a single strong source in the FoV of the instrument [73].

The BEST-2 array was calibrated using a standard calibration method in which a bright, known, radio source is used to obtain a calibration solution for the array. The received signal is the sum of the signal noise and the source flux multiplied by the gain of the antenna. While the source flux is correlated across the array, the system noise and antenna gain are not [74]. The input data from the 32 element receiver is fed to a correlator as a radio source transits over the array. The correlator produces a series of co-variance matrices that are generated by cross-correlating the output from all the receivers commonly referred to as baselines visibilities. The generated matrix for the whole observation is persisted to disk.

Previous studies [74] obtained gain calibration solutions using the column ratio gain estimation method described in [75]. In this work, per-antenna complex gain solutions are obtained using the popular Statistically Efficient and Fast Calibration (StEFCal) calibration algorithm described in [76, 77]. StEFCal is a computationally efficient method of obtaining per-antenna complex gain solutions for large radio astronomical arrays. The algorithm tries to find the minimum Frobenius norm difference between the observed visibilities D (correlation matrix) and the gain matrix G . This can be written as,

$$\min_G \|D - G^H M G\|_F \quad (2.22)$$

where, M is the model visibilities, and G^H is the Hermitian transpose of the gain matrix G . StEFCal uses the normal equations method to iteratively

solve for G using a least-squares estimation method. The complex coefficient solutions G are updated after each iteration until the convergence criteria, set by the user, is met. A detailed description of this method can be found in [77].

A typical calibration solution is shown qualitatively in Figure 2.10. The uncalibrated fringe pattern is compared with that obtained once the antenna corrections are applied. One can observe that in the latter case, the received signals are aligned in phase, thereby illustrating a calibrated array. The generated calibration coefficients are the product of both instrumental errors as well as geometrical corrections. Geometrical corrections compensate for the fact that the plane wave-front from the source impinges on the array elements with different time delays. Thus, the geometrical delays are removed such that the resultant coefficients are valid for all declinations.

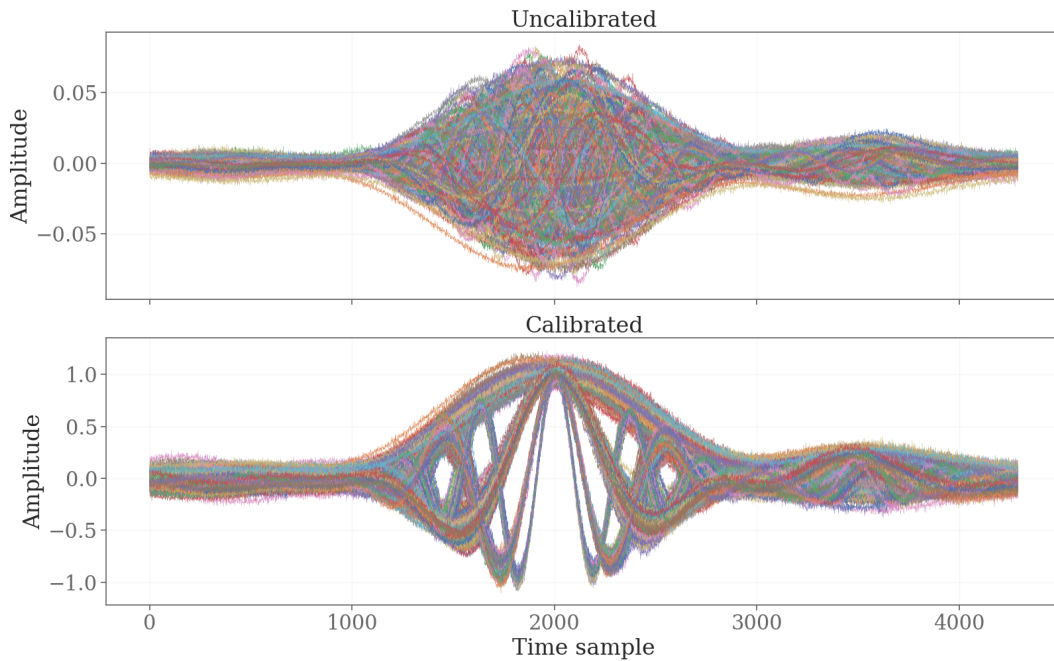


Figure 2.10: The baseline visibilities before and after calibration on Taurus A

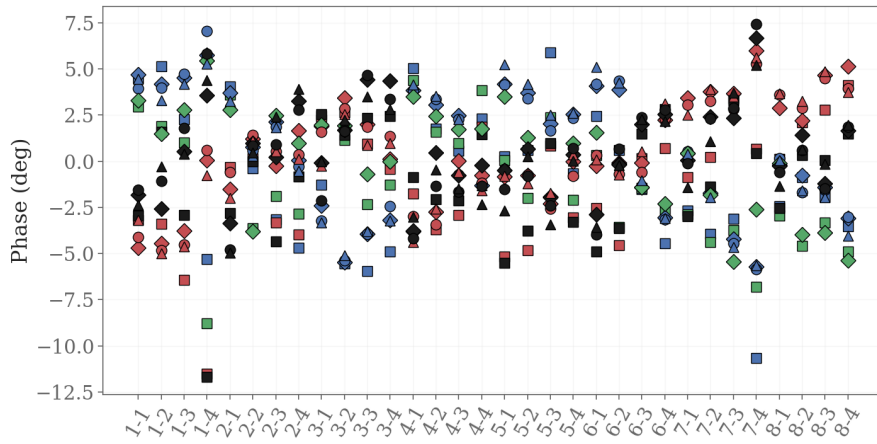
Calibration techniques relying on astronomical point sources are restricted to a limited number of calibration windows per day depending on the number of available point sources. Consequently, the generated calibration coefficients must remain suitable for multi-day timescales. The degree of stability of the calibration solution determines the frequency at which calibration observations need to be performed, which is ideally kept low given that observation time is expensive.

The stability of the calibration solution can be determined by analysing the degree of change in the antenna calibration coefficients that were generated through successive calibration observations. Back in 2014, Foster et al. [74] stated that a calibration observation every few days should be satisfactory for the BEST-2 array given that the calibration solutions were stable in both phase and amplitude.

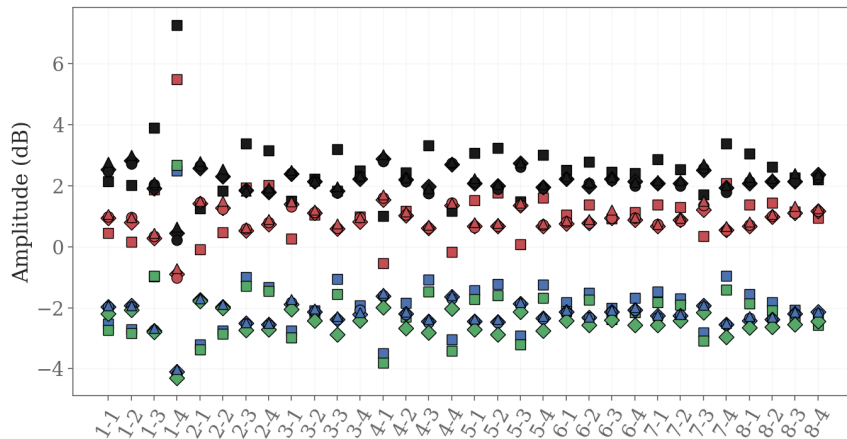
Figure 2.11 shows the phase and amplitude antenna corrections for a total of 10 calibration observations that were taken over a few days. The stability of both phase and amplitude is estimated by showing the deviations from the mean value. Figure 2.11a shows that over this period, the phase correction varies over a few degrees, across most of the antennas, and can thus be considered to be stable. However, as shown in Figure 2.11b, the amplitude correction can vary by tens of dB. One may note that there seems to be a bias in the corrections that seem to be dependant on the calibration source. One can theorise that this effect is due to the diurnal effects on the array due to temperature difference. It was also noted that these effects were independent of the calibration algorithm used.

These results suggest that, contrary to what was reported in [74], a calibration observation needs to be performed frequently, preferably at the start of an SSA observation campaign. Alternatively, a calibration solution performed within a similar time window can be used to mitigate the impact of diurnal effects on the array. Multiple calibration solutions, obtained on different times of day, can be made available depending on the time of observation. Future studies should aim to confirm these results on a larger set of observations. These studies should also help to address the impact of diurnal effects and whether the instability reported is a consequence of spurious Radio-Frequency Interference (RFI).

It is not always possible to schedule calibration observations at a satisfactory frequency. For instance, it is difficult to schedule a calibration observation during beam park campaigns, where the bi-static radar is expected to operate continuously for an extended period. Thus, future work should investigate the cause of the instability reported in this section and whether they are inherent to the instrument itself and the impact of the diurnal changes on the system noise of the array. Besides, other calibration algorithms and techniques can be evaluated. One alternative is the use of artificial sources as calibrators instead of astronomical ones as discussed in the previous section.



(a) Phase



(b) Amplitude

Figure 2.11: Complex gain solutions obtained through 10 calibration observations of Cassiopeia A (blue), Cygnus B (green), Taurus A (red) and Virgo (black), taken over a span of 7 days

2.4 Space surveillance using the BEST-II phased array

Since 2014, path-finding studies by INAF and the Istituto di Radioastronomia (IRA), have investigated the use of the BEST-2 array as a receiver for a bi-static space surveillance radar. The aim of these studies was to determine the suitability of the UHF radar measurements for space debris monitoring. Initial tests used the BEST-2 antenna in a bi-static configuration with a 3 m transmitter located 5 km from the receiver [78, 50]. The encouraging results

of those path-finding studies led to the inception of the Bi-static RAdar for LEO Survey (BIRALES) bi-static radar for SSA. This operational radar was the fruit of a collaboration between INAF, the University of Malta and the Politecnico di Milano. The aim of the project was the realisation an operational bi-static radar for orbital debris in LEO. In so doing, it fulfils the requirements for the participation within the European SST Support Framework [79, 78].

Early advances in radar technology were driven by military applications, most often in the tracking and surveillance of enemy ships or aircraft. The technology saw its initial developments during the 1930s and through the second World War [80]. Since then, this technology saw widespread adoption in a plethora of applications ranging from proximity sensors to 2D/3D dimensional mapping and meteorological monitoring. More recently, radar technology saw its use in the detection and tracking of in-orbit objects in LEO.

A basic radar system can be thought of consisting of a transmitter that irradiates the target with Electromagnetic (EM) signals and a receiver component that reads the echoes back-scattered by the target object. Most modern radars are mono-static where the same antenna is used as both the transmitter and receiver of EM radiation. In this configuration, the receiver needs to be shielded from the high-powered EM waves emitted by the transmitter to avoid damaging the receiver's electronics. Otherwise, the radar jams itself since the EM radiation is introduced directly into the receiver [64].

In bi-static radars, the interaction between the transmitter and receiver is minimised by having these two components physically separated by a considerable distance. Bi-static radars are usually more complicated to deploy and operate given that two, often very different, antennas are used at the transmitter and receiver sites. Specific communication protocols need to be put in place for the two components to work in tandem as a single instrument.

Another advantage of having two independent antennas for the reception and transmission is that it makes it possible to combine the receiver of the antenna with any transmitter operating in the receiver's bandwidth. This flexibility renders itself particularly useful in the design and construction of new SST monitoring assets which make use of existing instrumentation, such as astronomical radio telescopes.

The transmitted EM radiation can be classified into two general categories: CW and pulsed waveforms. In pulsed radars, the transmitter emits a train of pulses for a finite duration, or pulsed width τ that is typically $0.1 \mu\text{s}$ to $10 \mu\text{s}$

[64]. In long-range applications, such as space surveillance, the pulse width can exceed 1 ms such as in the case of the EISCAT [40] and TIRA [81] radar installations. These bursts are separated by a period where the transmitter is off. During this time, the receiver listens for the EM radar echoes. Range of a target can be estimated by timing the time taken for the pulse to be received at the receiver. The velocity of the target object can be determined by analysing the returned frequency of the radar echo. The total transmission and listening time is defined as one pulsed radar cycle, also known as the Pulse Repetition Interval (PRI). Thus, the Pulse Repetition Frequency (PRF) is the inverse of the PRI and it is the number of cycles the radar completes per second [82].

In a CW radar, the transmitter is operated continuously, usually without interruption. Range of a target can only be determined if the characteristics of the transmitted wave are changed. A simplified approach is to modulate the frequency of the transmitted wave. This technique, known as Frequency Modulated Continuous Wave (FMCW), puts a timing mark on the EM wave, thereby enabling the target's range to be determined [72]. Chapter 3 describes the FMCW radar used in this work to determine the range of a target object.

CW radars are relatively simpler and cheaper to design when compared to other pulsed radars. In a CW radar, the transmitter can reach a greater mean power, when compared to a pulsed radar with a fixed peak power transmitter. Unmodulated CW radars can only detect moving targets. The reflected radiation from stationary objects will be masked by the carrier frequency, f_0 . On the other hand, non-stationary objects can be distinguished from the background clutter by measuring the doppler shift f_d of the incident radar echo. This makes it ideal for the detection of long-range objects such as in the detection of high-altitude orbiting objects. In fact, CW radars are popular as early warning surface-to-air missiles radars. The main limitation of a CW radar is the probability of feedback from the transmitter carrier signal that can 'feedback' into the receiver. This can be minimised by having the receiver separated from the transmitter [64].

2.5 Doppler shift

The frequency f_r of the radiation reflected off a target object moving relative to the radar will be different from the transmitted frequency f_0 . This is due to the

Doppler effect in which the received signal, reflected off an approaching target, has a higher frequency. Conversely, a decrease in frequency is experienced for a receding target. Given that the velocity v of the target is a small fraction of the speed of light c , relativistic effects can be ignored such that the relationship is given by,

$$f_r = [1 + 2(v/c)]f_0 \quad (2.23)$$

The difference between the transmitter and the reflected frequency, Δf , is known as the Doppler shift and is given by,

$$\Delta f = \frac{2v}{c}f_0 = \frac{2v}{\lambda} \quad (2.24)$$

Where λ is the transmitted wavelength, and positive values of v correspond to a target approaching the receiver. Thus, the Doppler shift is shown to be proportional to the relative velocity along the Line of Sight (LOS) between the radar and the target object, known as the radial velocity or range rate. The Doppler shift can be used to distinguish between moving targets from background radar clutter [83]. Thus, a hyper-velocity RSO can be identified by their Doppler-shifted radar signatures. In a bi-static radar, the bi-static Doppler shift is defined as,

$$\Delta f = -\frac{1}{\lambda} \frac{d}{dt}(R_1 + R_2) \quad (2.25)$$

Where λ is the transmitted wavelength, R_1 is the distance between transmitter and target and R_2 is the distance between target and receiver [6]. Measurements of the doppler shift in frequency as a target object transits over the receiver can be used to determine the target object's orbital state. As the target object transits over the instrument's FoV the received frequency will typically vary from several thousands of Hz above the transmitter frequency (on approach) to several thousands of Hz below the transmitter frequency as the object moves away from the receiver [84].

The variation in the frequency with time for a typical object is sometimes referred to as doppler curve. An example of a doppler curve is given in Figure 2.12. The doppler curve is a function of the relative motion between the receiver of the radar and the target object. The very high velocity of in-orbit objects means that passages of the target objects over the BEST-2's FoV range

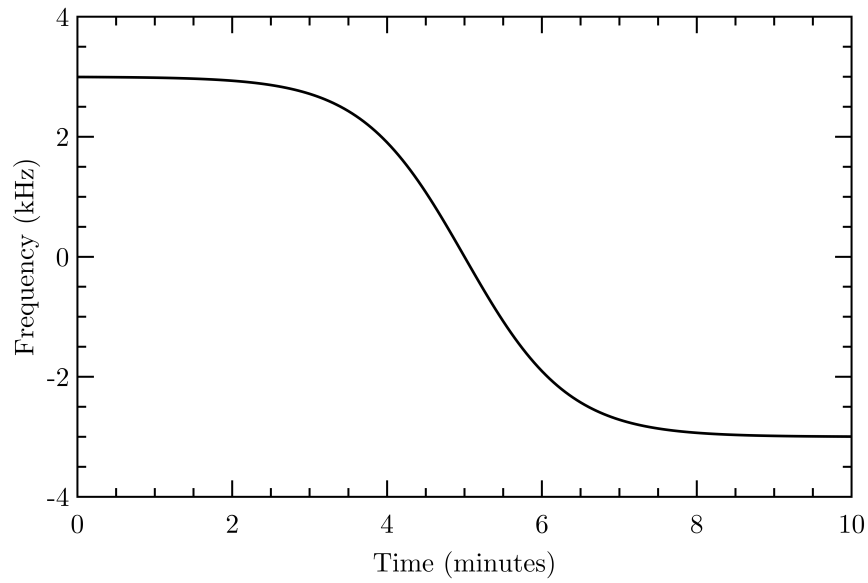


Figure 2.12: A representative doppler curve that is typical of a passage from a high-velocity orbiting objects such as a satellite

from a few seconds to tens of seconds. Given this very short time interval, the doppler curve can be assumed to be linear in time.

2.6 The radar equation

A radar system consists of a receiver and a transmitter antenna. In a monostatic radar, the receiver and the transmitter are the same. On the other hand, in a bistatic system, such as the one that is investigated in this study, the transmitter and the receiver antenna are two different antennas at two different locations. In both scenarios, the power density Q_i (W m^{-2}) of the transmitted signal at a target a distance R away from the radiating antenna is given by,

$$Q_i = \frac{P_t G_t}{4\pi R^2} \quad (2.26)$$

where G_t is the gain and P_t is the total peak power (W) of the radar transmitter antenna. The incident radiation is reflected off by the target and propagated back to the receiving component of the radar system. The reflected power P_{refl} in the direction towards the receiver is proportional to Q_i [83] and is given by

$$P_{\text{refl}} = Q_i \sigma = \frac{P_t G_t}{4\pi R^2} \sigma \quad (2.27)$$

where the constant of proportionality, σ , is often referred to as the target object's RCS and is determined by the physical size, the shape and material of the object [64]. The incident radiation on the target object is reflected back to the receiving antenna such that the power density at the receiving antenna, Q_r , is given by

$$Q_r = \frac{P_{\text{refl}}}{4\pi R^2} \quad (2.28)$$

Thus, by combining Equation 2.27 and Equation 2.28 an expression for the received power density at the receiver can be obtained,

$$Q_r = \frac{Q_i \sigma}{4\pi R^2} = \frac{P_t G_t \sigma}{(4\pi)^2 R^4} \quad (2.29)$$

The total power P_r received at the radar is the power density at the antenna multiplied by the effective area A_e of the receiving antenna, hence,

$$P_r = Q_r A_e = \frac{P_t G_t A_e \sigma}{(4\pi)^2 R^4} \quad (2.30)$$

In an ideal case, the signal received by the radar is solely due to radiation reflected back by the target object. However, the received signal is usually characterised by another interfering signal which varies randomly in phase and amplitude. This interference, also known as white or thermal noise, can come from multiple sources. Noise sources include galactic, solar, atmospheric, ground and man-made interference (such as RF sources). These sources can be represented by the thermal noise power P_n in the radar receiver,

$$P_n = kB_nT_s \quad (2.31)$$

where k is the Boltzmann's constant, T_s is the system noise temperature and B_n is the instantaneous noise bandwidth of the receiver. The system noise temperature is a combination of three separate components, such that,

$$T_s = T_a + T_r + L_rT_e \quad (2.32)$$

where T_a is the noise contribution from the antenna, T_r is the contribution from the RF components between antenna and the receiver, L_r is the loss of the input RF components and T_e is the temperature of the receiver.

Successful detection of the target can only be made if the power of the received echo exceeds the noise power by a significant margin. Otherwise, the received signal would be indistinguishable from the background noise. The SNR is defined as the ratio between the target signal power P_r and the noise power P_n . Hence,

$$\rho = \text{SNR} = \frac{P_r}{P_n} = \frac{P_t G_t A_e \sigma}{(4\pi)^2 R^4 k B_n T_s} \quad (2.33)$$

In the expressions obtained thus far, it was assumed that the distance R_1 between the target and the transmitter is equal to the distance between the target and the receiver, R_2 , as in the case of a mono-static radar. In the general case where, $R_1 \neq R_2$, the bi-static form of Equation 2.33 can be generalised to,

$$\rho = \text{SNR} = \frac{P_r}{P_n} = \frac{P_t G_t A_e \sigma}{(4\pi)^2 R_1^2 R_2^2 k B_n T_s L} \quad (2.34)$$

where the dimensionless term L was introduced to account for the total system losses arising from the waveguides used, filters, antenna efficiency, beam shape and attenuation due to the atmosphere.

Thus far, the dimensionless loss factor L was assumed to be constant. In reality this is product of multiple loss factors [64],

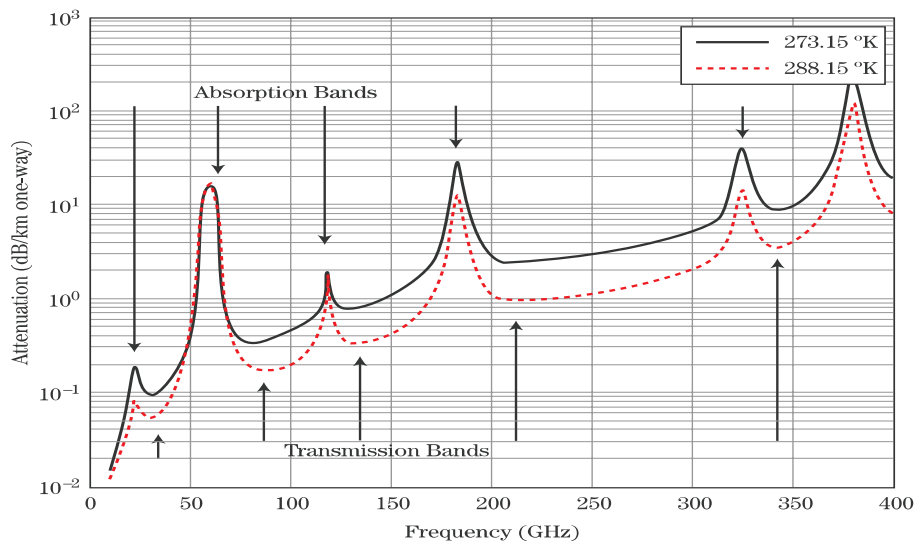
$$L = L_t L_a L_r L_{sp} \quad (2.35)$$

where, L is the total system noise, L_t is the transmitter loss, L_r is the receiver loss, L_{sp} is the signal processing loss and L_a is the loss due atmospheric attenuation of the signal. The atmospheric loss L_a is a function of the distance between the target and the receiver/transmitter. For a bi-static radar, this is given by [83],

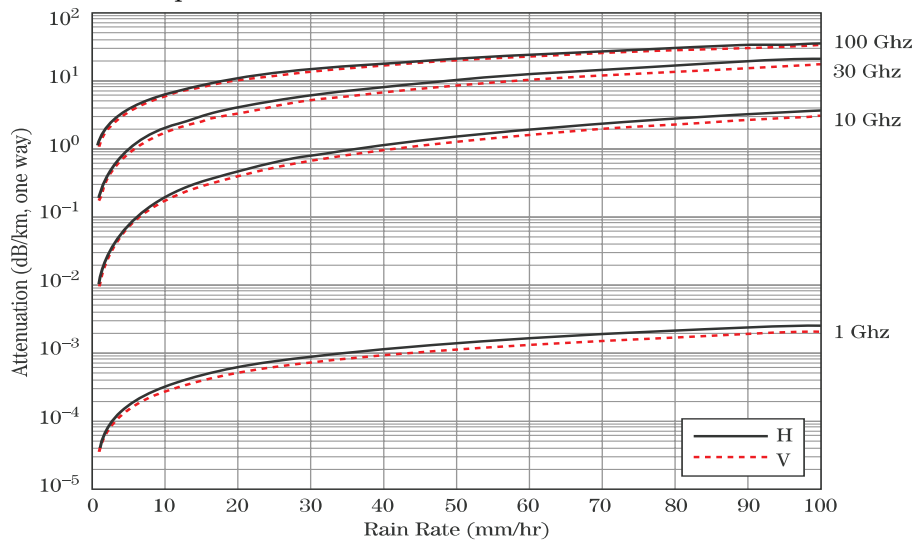
$$L_a[\text{dB}] = \alpha(R_1 + R_2) \quad (2.36)$$

The attenuation coefficient α depends on the condition of the atmosphere and the signal carrier frequency. The electromagnetic radiation is affected by several physical phenomena, including absorption and scattering. Absorption occurs when the water vapour and oxygen present in the atmosphere absorb some of the electromagnetic wave's energy. On the other hand, scattering is the process through which particulates within the atmosphere reflect the incident radiation in a different direction away from the receiver antenna of the radar system. The degree of attenuation is frequency dependant, as illustrated in Figure 2.13a. Similarly, meteorological conditions, such as rain and fog, can also attenuate electromagnetic waves, as shown in Figure 2.13b [64]. This suggests that longer-wavelengths radar systems are more suitable for long-range, all-weather observations.

One may note that UHF radars are less susceptible to atmospheric attenuation. However, atmospheric effects were still accounted for in this study. This attenuation decreases with altitude as the radio beam path passes through the rarefied layers of the atmosphere [83]. At ranges greater than 10 km, losses due to atmospheric attenuation can be neglected [85]. This loss is accounted for twice since the signal travels through two different paths on transmit and receiver [64]. The attenuation due to the atmosphere is also affected by the elevation of the antenna. The resultant air mass as the elevation of the antenna is changed can be derived by using the Maddalena and Johnson [86] model or through the Chebyvhev fitting of the Bemporad [87] tables. These effects are assumed to be minimal, given the large distances involved and the operating frequency.



(a) Attenuation of the radar signal as a function of frequency at two different temperatures



(b) Attenuation of the radar signal as a function of rain rate at four different frequencies for the horizontal (H) and vertical (V) field components

Figure 2.13: Attenuation of the radar signal as a function of frequency and rain rate. Figures adapted from [64]

2.7 Radar capability

In this study, the BEST-2 instrument is investigated as a candidate radio telescope for the receiving part of a bi-static radar system. To do so, we simulate the theoretical capability of such an instrument using the radar-range equation (Equation 2.34) derived in the previous section. In these simulations the

antenna bandwidth B_n was assumed to be 9.5 Hz. In the absence of an empirically determined system loss, the transmitter and receiver loss were taken to be 10 dB while the signal processing loss was assumed to be 2 dB. Moreover an atmospheric attenuation coefficient of 0.002 dB km^{-1} was used. This gives a maximum atmospheric attenuation (two-way) loss of 0.04 dB. The UHF transmitter was assumed to be a 7 m parabolic reflector having a maximum power of 10 kW while the receiver was taken to be the BEST-2 array. A detection threshold of 10 dB was assumed. The gain of the transmitter antenna G_t is given by,

$$G_t = \frac{4\pi A_t}{\lambda^2} \quad (2.37)$$

where A_t is the effective aperture of the transmitter antenna. Substituting Equation 2.37 in the radar range equation (Equation 2.34) gives

$$\rho_{\min} = \frac{P_r}{P_n} = \frac{P_t A_e \sigma A_t}{4\pi R_1^2 R_2^2 k B_n T_s L \lambda^2} \quad (2.38)$$

where ρ_{\min} is the minimum SNR required for a reliable detection [64]. If we define a constant κ as

$$\kappa = \frac{P_t A_t A_e}{4\pi k B T_s L \rho_{\min}} \quad (2.39)$$

The radar-range equation can be expressed as,

$$R_1^2 R_2^2 = \sqrt{\kappa \sigma_{\min}} \frac{1}{\lambda} \quad (2.40)$$

This expression can be used to illustrate the relationship between the maximum detectable range and the operating frequency of the instrument for a fixed RCS. Figure 2.14 shows that as the working frequency increases, so does the theoretical distance at which a fixed sized object can be detected. Conversely, as the wavelength is decreased the detection range is increased. However, the improvement in detection is limited since at higher working frequencies the atmospheric losses and influence of water vapour becomes substantial as discussed in the previous section [16]. The results show that at the BEST-2 operating frequency (400 MHz to 416 MHz), an object with an RCS of -10 dB m^2 can be theoretically detected around 794 km (59 dB m) away from the receiver.

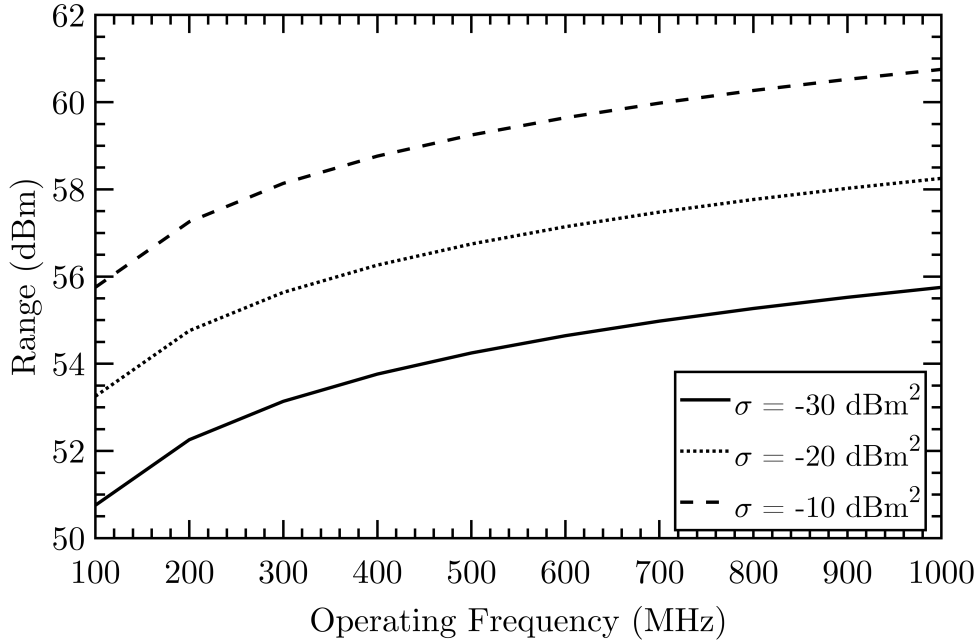


Figure 2.14: The theoretical range at which three different targets of varying RCS can be detected as a function of the radar's operating frequency

The target RCS can be used to determine the equivalent diameter for an idealised conducting sphere [88]. The equivalent diameter d_{\min} varies depending on the working frequency region. In the optical region ($\lambda \ll$ target size), the relationship is,

$$d_{\min} = 2\sqrt{\frac{\sigma_{\min}}{\pi}} \quad (2.41)$$

while in the Rayleigh region ($\lambda \gg$ target size), the relationship is given by,

$$d_{\min} = \left(\frac{\sigma_{\min}\lambda^4}{\pi}\right)^{1/6} \quad (2.42)$$

Hence,

$$d_{\min} = \sqrt[6]{\frac{R_1^2 R_2^2 \lambda^6}{144\kappa\pi^5}} \quad (2.43)$$

This relationship can be seen illustrated in Figure 2.15. One can note that at 400 MHz, objects with an equivalent diameter of around 10 cm can theoretically be detected up to a range of 800 km from the receiver. This suggests that such a radar would be suitable for the detection of small objects in LEO

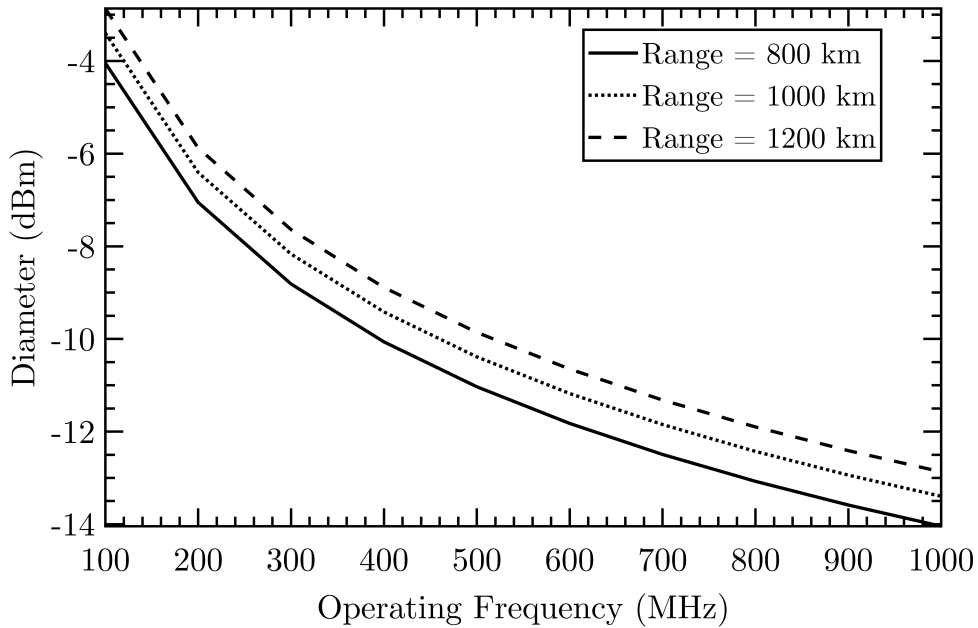


Figure 2.15: The relationship between the diameter of a detectable target and the working frequency frequency

Thus far, it was assumed that a 10 kW transmitter was used. Let,

$$\psi = \frac{\rho k B T L \pi^2 4 (R_1 R_2)^2}{G_t A_e} \quad (2.44)$$

such that the radar-range equation can be re-written as,

$$\sigma_{\min} = \frac{\psi}{P_t} \quad (2.45)$$

Thus, Equation 2.45 can be used to estimate the minimum detectable RCS as a function of the transmitter power or available power budget. Figure 2.16 shows that as the transmitter power increases, so does the smallest detectable RCS. Targets at an RCS of -2 dB m^2 can be detected at a distance of 800 km if the transmitter power is just 2 kW. However, the transmitter power has to increase by more than five-fold for the detection distance to increase by 400 km. These considerations are important in the design of a new radar system.

These simulations are important in order to establish the minimum technical specifications for a long-range radar system. The results suggest that the BEST-2 phased array is a promising receiver for a bi-static SSA radar if it is coupled with a suitable transmitter. Indeed, the array is the basis for one of

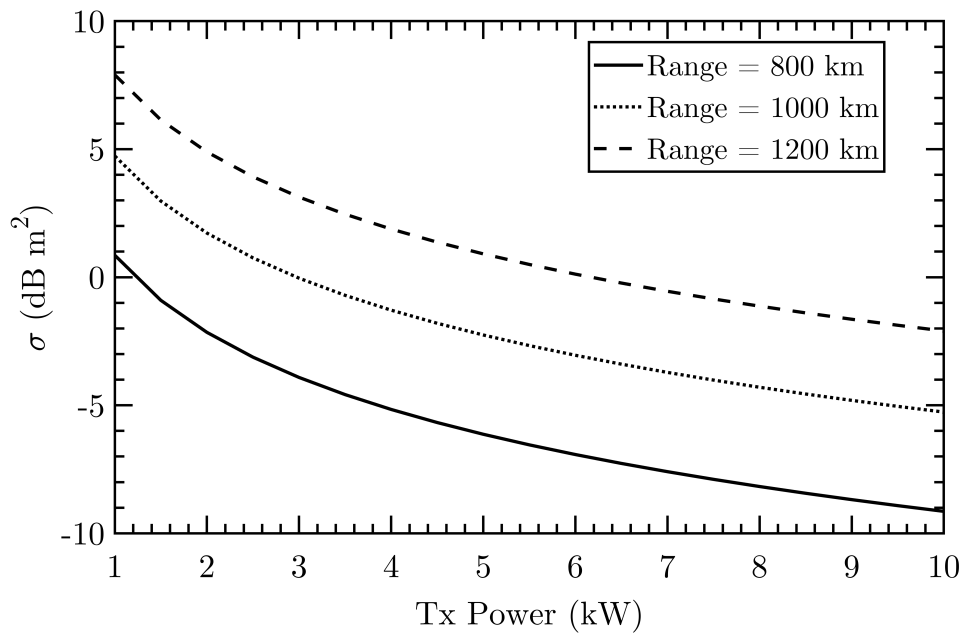


Figure 2.16: The theoretical range at which an object with a given RCS is detected if this is plotted as a function of the transmitter power

Europe's latest space surveillance radars. This novel instrument is introduced in the next chapter.

2.8 Conclusion

In this chapter, the theoretical background behind the remote sensing of objects using radar technology was presented. This work investigates the use of the BEST-2 phased array as a potential receiver for a new bi-static radar. Simulations have shown that if the BEST-2 array is coupled with a powerful transmitter, the system should be capable of monitoring space objects in LEO.

In Section 2.2.1, the beam pattern of the BEST-2 array, obtained through simulation, was presented. The model was validated against the data obtained empirically using received flux from an astronomical radio source. The agreement between the simulated and experimental data is positive. However, this agreement becomes less pronounced as the beam is steered away from broadside. The analysis of the model indicates that steering far off broadside in the azimuth direction would give rise to quantisation lobes. Moreover, large steering angles in the EL plane would introduce grating lobes. This is not desirable for tracking applications.

These errors can be minimised if the angle at which the beams are steered is reduced. The emergence of the grating lobes coupled with the pointing errors introduced by the quantisation lobes re-affirms the need for an accurate determination of the receiver's radiation pattern.

Consequently, a new drone-based verification system for large-aperture arrays was proposed in this work. Unlike other systems, this system can obtain the measurement data of an antenna in real-time. Future versions of this system will integrate with a new software backend that was developed for the BEST-2 array. This software backend is described in detail in the next chapter.

Chapter 3

The BIRALES bi-static radar

In Chapter 2, it was shown that the BEST-2 phased array is a suitable receiver for a bi-static radar for space surveillance in LEO. In this chapter, we extend the discussion to present the purposely built BIRALES radar. This radar is the fruit of an international collaboration between various institutions. The transmitter part described in this study was developed by the engineers at the Astronomical Observatory of Caligari, while the receiver chain is a collaboration effort between researchers at the University of Malta and the Medicina Radio Astronomy station. The discussion focuses on the receiver's software components developed in this study.

This chapter is organised as follows. An overview of the components making up this new bi-static radar will be discussed first. Then, the theoretical detection capability is derived using the equations presented in the previous chapter. This is followed by an in-depth description of the software architecture used for the receiver component of this radar.

3.1 The BIRALES radar

BIRALES is a bi-static radar consisting of the Radio Frequency Transmitter (TRF) fully steerable parabolic antenna located in the Italian Joint Test Range in the region 'Salto di Quirra', Caligari, Sardinia, Italy. The 7 m transmitter antenna (Figure 3.1) has a maximum speed of 3°s^{-1} with an accuracy of 0.1° , and is able to supply a maximum RMS power of 10 kW in the bandwidth 410 MHz to 415 MHz [89]. The receiver of this radar is the BEST-2 array, de-

scribed in the previous chapter. This gives the bi-static instrument, illustrated in Figure 3.2, a baseline of about 580 km.



Figure 3.1: The parabolic antenna in ‘Salto di Quirra’, Caligari, Sardinia [90]

The transmitter and receiver environments are characterized by strong RFI sources [74, 91] that may limit the usable bandwidth and thereby affect the performance of the receiver [90]. The B-band (250 MHz to 500 MHz) formerly known as P-band, is used by local TV radio links, WX weather balloon and military radio communication services such as the TERrestrial Trunked RA-dio (TETRA) system assigned to the Italian Ministry of Defence (MoD) [89]. These issues were put into considerations when selecting the operating frequency of the transmitter.

It is customary to plot the SNR as a function of the range of interest. The figure allows one to analyse the performance rating of the instrument. Figure 3.3 illustrates the simulated capability of the BIRALES radar. Assuming a minimum detection threshold of at least 10 dB, a target object having an RCS of 0.001 m^2 can only be detected at a distance of around 250 km from the receiver. The detection of such targets using the existing radar configuration can only be improved by either increasing the transmitter power or by lowering the threshold by introducing a more sensitive detection algorithm. Simulations suggests that the present configuration of the BIRALES radar is capable of detecting RSO whose RCS is greater than 0.1 m^2 . Targets having an RCS of 1 m^2 are expected to be detected at a distance of 1200 km from the receiver.

The radar range equation introduced in the previous section assumes that a single pulse is used to detect a target. In a pulsed system, several pulses are transmitted and received, usually in the order of 16 to 20 pulses [64].

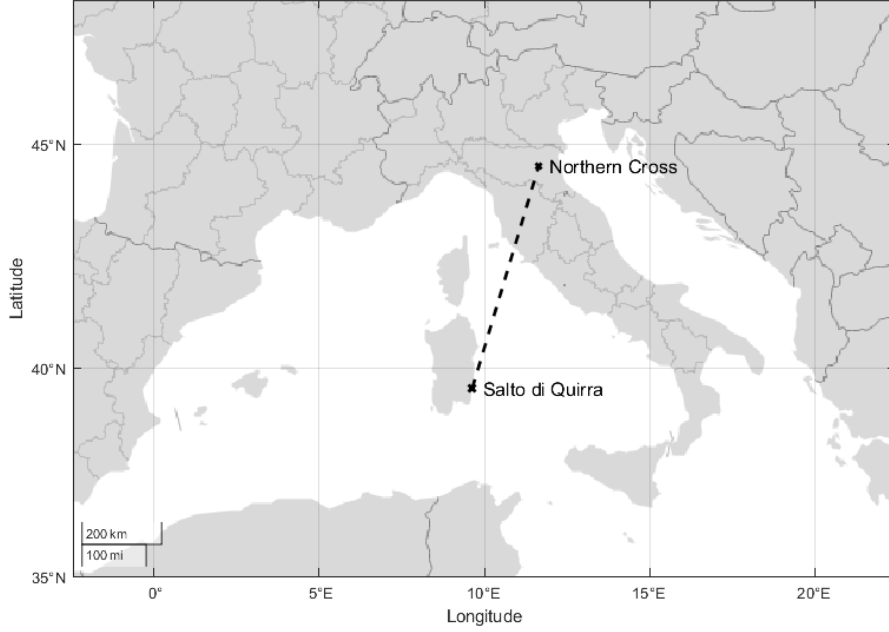


Figure 3.2: The BIRALES bi-static radar is composed of a transmitter in ‘Salto di Quirra’, Caligari, Sardinia and the BEST-2 antenna within the Northern Cross located in Medicina, near Bologna, Italy. This distance between the two instruments (baseline) is 580 km

The maximum radar range coverage is dependant on the power budget of the transmitter. In a CW radar, the mean power P_m of the transmitter is equivalent to its peak power P_p , given that it is being operated continuously. On the other hand, the mean power of a pulsed radar is given by,

$$P_m = P_p \frac{\tau_p}{T_d} \quad (3.1)$$

where $\tau_p = \eta\tau$ is the time taken to transmit η pulses of width τ and T_d is the dwell time. Equation 3.1 can be expressed as,

$$P_m = \frac{P_{m.cw}}{Q} \quad (3.2)$$

where $Q = \frac{\tau_p}{T_d} \gg 1$. Thus, all things being equal (system loss, detection threshold), the peak power of a pulsed radar should be Q times as large as that of a CW to obtain the same range coverage of a continuous wave radar with the same mean peak power [83]. Given that the radar usually transmits several pulses and processes the results of those pulses to detect a target, the

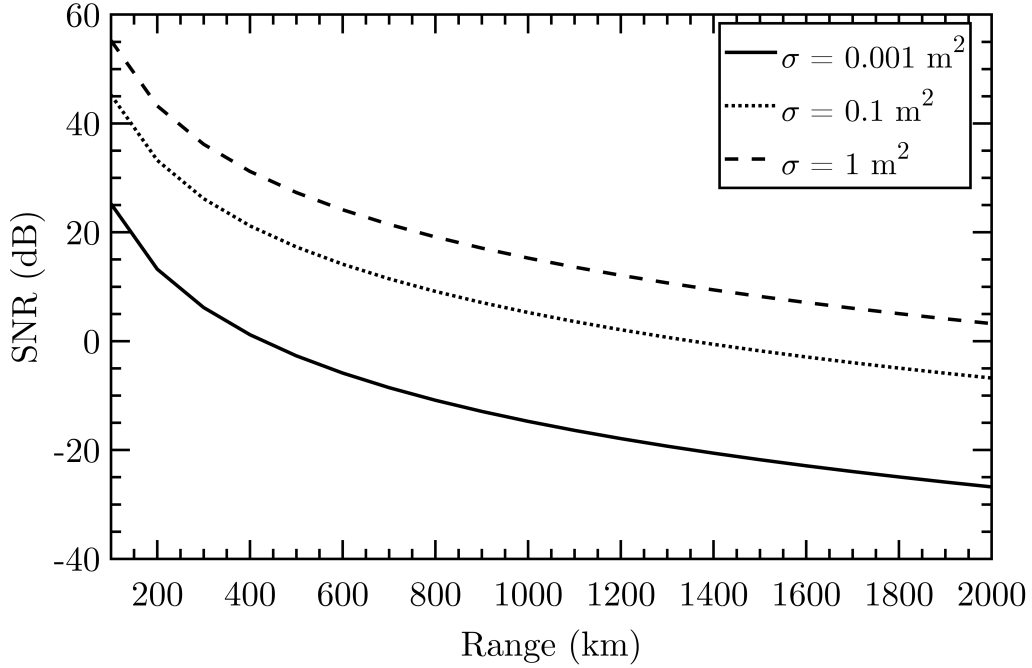


Figure 3.3: The simulated SNR as a function of range

peak power P_p in the radar range equation needs to be replaced by the mean power P_m that is given by,

$$P_m = P_p \tau \text{PRF} \quad (3.3)$$

Alternatively, this can be expressed in terms of the dwell time $T_d = \frac{\eta}{\text{PRF}}$,

$$P_m = P_p \tau \frac{\eta}{T_d} \quad (3.4)$$

The optimum receiver bandwidth, B , for a pulse of width τ is given by [64],

$$B = \frac{1}{\tau} \quad (3.5)$$

Substituting the term P_m , for the transmitter power P_t in the radar range equation gives,

$$\text{SNR}_p = \frac{P_m T_d \beta}{\eta} \cdot \frac{G_t G_r \lambda^2 \sigma \eta}{(4\pi)^3 R^4 k T L B} \quad (3.6)$$

Hence, the radar range equation for a pulsed system is given by,

$$\text{SNR}_p = \frac{P_m T_d G_t G_r \lambda^2 \sigma}{(4\pi)^3 R^4 k T L} \quad (3.7)$$

This suggests that the measured SNR can be altered by changing the dwell time, T_d , of the radar which can be altered by increasing the number of pulses or by lengthening the pulse width (or the decrease the PRF). In fact, long-range radars, such as those used in space surveillance, typically use pulse lengths in the order of 1 ms [92].

The capability of the BIRALES radar can be compared against two other European SSA sensors, the TIRA and the EISCAT radars in Figure 3.4. Care was taken to ensure that the real-world parameters of these instruments were used, when these were available. However, it was difficult to obtain the exact values for all the parameters. In the case where such parameters could not be found, the parameter, such as system loss, was assumed to be equivalent to that used in BIRALES. The results show a preliminary evaluation of the radar against existing state-of-the-art installations. A more rigorous comparison would entail the knowledge of the exact parameters of these instruments. Thus, these results have to be taken with some caution, given that the exact parameters of both radars are not publicly available. The parameters used as listed in Table 3.1.

	EISCAT ¹	TIRA ²	BIRALES
Operating frequency (MHz)	930	1300	410
Rx Area (m ²)	804	1735	1411
Tx Area (m ²)	804	1735	38
Tx Peak Power (kW)	1600	1500	10
Pulse length (ms)	1	1	n/a
PRF (Hz)	50	40	n/a
N. Pulses	20	20	n/a
Attenuation coefficient (dB km ⁻¹)	0.010	0.010	0.002

Table 3.1: Simulation parameters used to asses the SSA radar capabilities in Figure 3.4

One may observe that the theoretical detection ability of the BIRALES radar is not at par with the other more established SSA instruments. Using

¹ Data obtained from: www.eiscat.se

² Data obtained from: www.fhr.fraunhofer.de

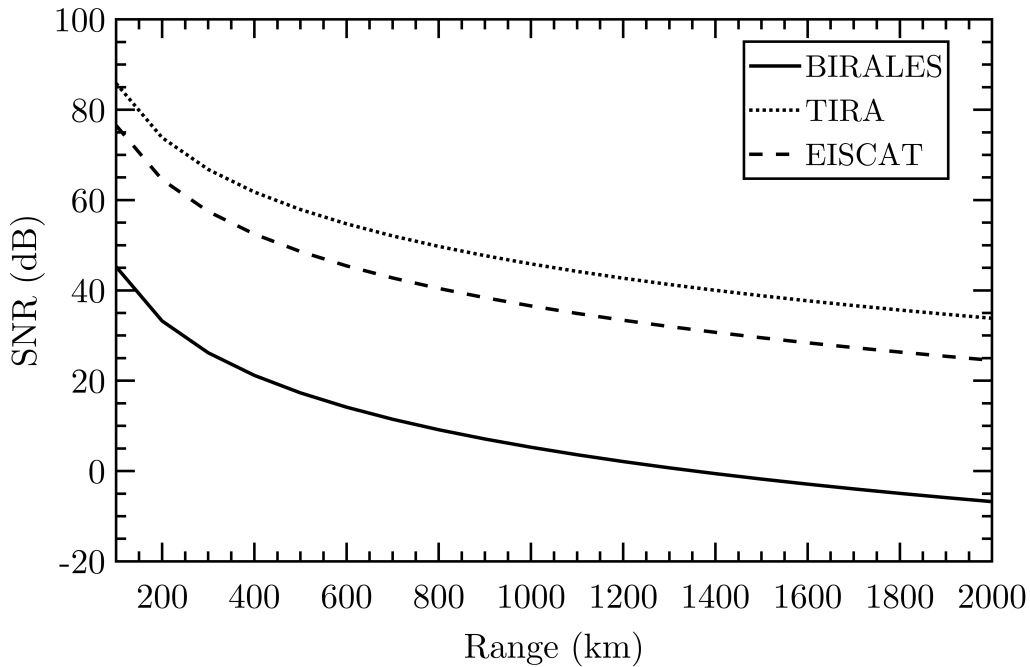


Figure 3.4: A comparison between the simulated performance of the established SSA radars EISCAT (Tromsø) and TIRA, with the proposed BIRALES radar

an expository target of 0.1 m^2 and a 10 dB detection threshold, one may note that the maximum range for such a target in the case of BIRALES is just over 750 km. When this is compared with the performance of other instruments, one can observe that such a target is still detectable at a range in excess of 1200 km. While the BIRALES radar is shown not as sensitive as the more established instruments, the results are encouraging.

The BEST-2 receiver is just a small section (8 out of 64 parabolic reflectors) of the Northern Cross. A fully upgraded Northern Cross would see the total collecting area of the receiver increase from the current 1411 m^2 to 7260 m^2 . Such an upgrade would make BIRALES one of the largest space monitoring instruments in the world. Additionally, the bi-static nature BIRALES means that its design is not tightly coupled with any transmitter. Thus, it can be easily be used with any other compatible transmitter in the Northern Hemisphere, thereby greatly enhancing its potential.

3.2 System overview

An overview of the radar, together with the main components making up the system, is shown Figure 3.5. One may observe that the receiver chain of this radar can be split into two major sub-systems. The first system is used to determine the range of a target object while the second system in the BIRALES radar, and the subject of this work, estimates the target's Doppler shift information and trajectory. These two very different systems require a transmitter that can simultaneously work in pulsed compression mode for range measurements and in CW mode for Doppler measurements.

The doppler system uses a single but continuous sinusoidal RF signal at a fixed narrow-band frequency. Continuous-wave radar uses the doppler shift of the returning signal to infer the velocity of the object efficiently. The change in velocity is derived from the difference in the received frequency and the transmitted one. However, unmodulated continuous wave radars, such as the system described in this work, cannot measure range. As a result, a separate system for range was introduced for a complete characterization of a target's attitude.

The output of these systems is amalgamated together at a data fusion step and saved in Tracking Data Message (TDM) [93] format. The TDM output serves as the input to the orbital determination block developed by researchers at the Politecnico di Milano, Italy [94]. The algorithm is used to estimate the trace of the transiting object within the receiver's field of view and refine the orbital parameters of known RSO or perform an initial orbit determination in the case of unknown objects [94].

3.2.1 Ranging system

A CW radar can also be used to detect the range of the target. Contrary to the doppler processing system, which makes use of an unmodulated transmission, the transmitted waveform is modulated by applying a frequency shift that changes linearly in time [72]. This is known as a FMCW radar and, as is the case with the BIRALES radar, can be used to establish the range of a target.

The ranging system illuminates the target with a saw-tooth chirped waveform having a bandwidth of 4 MHz and centred at 412.5 MHz. The principle of

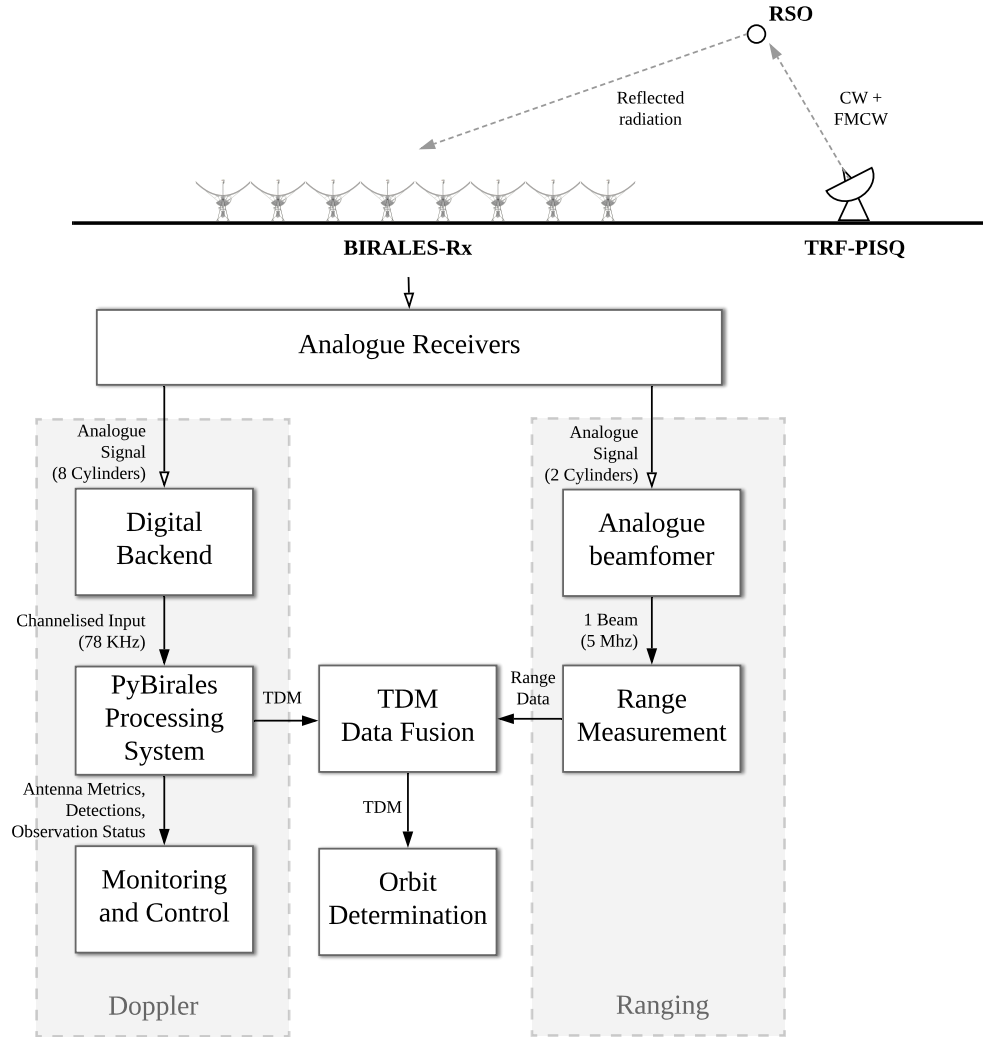


Figure 3.5: A block diagram illustrating the main components of the ranging and doppler detections systems making up the BIRALES bi-static SSA radar

FMCW radars are shown schematically in Figure 3.6 showing the relationship between the transmitted waveform and the received one.

The transmitted signal f_t is varied linearly in time in the range of $f_0 \pm f_m$. In the case where the target is stationary, the signal reflected off the target f_r , should follow the same frequency variation of the transmitted one but offset by a delay t_d [72], such that,

$$f_r(t) = f_t(t - t_d) \quad (3.8)$$

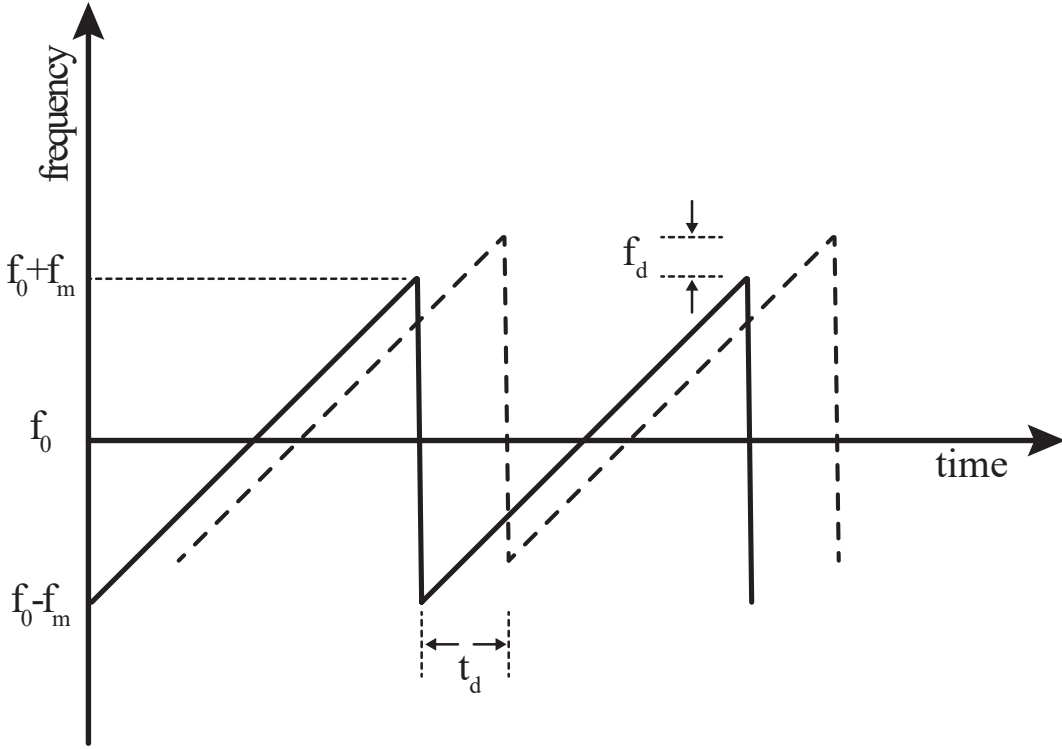


Figure 3.6: The transmitter signal (solid) and the reflected signal frequency (dashed) used by the ranging system

On the other hand, for a non-stationary target, the calculation has to take into account that the received signal will be shifted by a term f_d due to the target's motion. As shown in Figure 3.6, the range of a target can be calculated by comparing the transmitted signal to the received one. The correlation between the transmitted and the received signals can give a measure of both the target's range and radial speed. The target's range R can be determined if the time lag t_d is measured [95]. Thus,

$$R = \frac{ct_d}{2} \quad (3.9)$$

If the frequency, or doppler, shift between the frequency peaks is determined, a FMCW transmitter can be used to determine the radial velocity v_r , through [72]

$$v_r = \frac{\lambda f_d}{2} \quad (3.10)$$

For a ranging radar, the error in the range measurement is given by [96],

$$\Delta R = \frac{c}{2B} \quad (3.11)$$

where B is the frequency bandwidth. This means that the range resolution of the range component of the BIRALES radar working with a bandwidth of 5 MHz is around 30 m.

This system requires that the receiver and transmitter components of the radar are synchronized. GPS-disciplined oscillators installed in both the receiver and transmitter components give the ranging system a 10^{-7} s synchronisation error [90].

At the transmitter, a workstation running the system scheduler and waveform set is run. The scheduler reads the input data, such as epoch start and end time, signal power, frequency and pointings. This data is shared with the receiver at Medicina. The scheduler initiates the waveform set which sends the signal to the Universal Software Radio Peripheral (USRP)³ block through an Ethernet connection. The USRP block is a commercial field-programmable gate array (FPGA) which is used to generate the UHF signal to be sent to a control unit. The signal is passed through a radio frequency splitter that splits the signal into seven signals. These signals are individually amplified before being combined again, filtered using a low pass filter, and sent to the transmitter antenna for transmission of the RF signal [90].

At the receiver end, an analogue beamformer aggregates the signals from 2 cylinders (8 elements) to generate a single beam. The beamformed signal is fed to another USRP board at the receiver that digitalizes the 5 MHz signals before transferring the data to the workstation. At the workstation, the range from the target objects is determined. Consequently, range measurements from this block are combined with the data made available by the other system in BIRALES at a data fusion step.

3.2.2 Doppler processing

The amplified RF signals travel to a receiver room through 520 m long optical fibre links. These signals are down-converted to the intermediate 30 MHz frequency and then fed to a digital backend [97] adapted from [74]. The FPGA-

³ www.ettus.com

based system is based on the Reconfigurable Open Architecture Computing Hardware (ROACH) hardware developed by the researchers at the Collaboration for Astronomy Signal Processing and Electronics Research (CASPER)⁴. The reliability and performance achieved by these architectures saw hundreds of these boards deployed across many radio telescopes such as the MeerKAT [98] and Precision for Probing the Epoch of Reionization (PAPER)[99, 97] installations to name a few.

The BEST-2 digital backend used in this project has already seen extensive use beyond the SSA applications described here such as in search of radio transients such as pulsars [100]. The digital backend consists of a ROACH 1 board that is equipped with a CASPER 64ADCx64 ADC accepting the input from 32 single-polarization antennas. In this design, 32 signal streams are digitised at a rate of 40 MS s^{-1} for 20 MHz of digital bandwidth of which 16 MHz are useful [100].

The digital backend channelizes this band into a total of 256 frequency channels that are 78.125 kHz wide. Of the 16 MHz bandwidth available, a 5 MHz band is reserved for the ranging system. In contrast, a single channel is used by the doppler processing system given that the maximum Doppler shift corresponding to a RSO is expected to be in the order of a few tens of kHz. Consequently, setting the CW frequency at the centre of a coarse frequency channel band provides for a suitable detection window. At present, this is set to 410.085 MHz.

The output data rate D of digital backend processing A antennas at a sampling rate of T samples per second of word length W , across C frequency channels can be calculated using,

$$D = A \times T \times W \times C \quad (3.12)$$

Thus, for a single channel, $C = 1$, $T = 78\,125$ samples/s and $W = 64$ bit (32 bit real and 32 bit imaginary) the data rate requirements of the doppler processing system can be calculated to be 19.07 MB s^{-1} . While the output data rate is not as high as those typical of wide-band radio astronomy, it is not feasible to save the raw data. At this rate, the storage requirements would

⁴ www.casper.berkeley.edu

be 67 GB per hour, or 1.57 TB daily. This is the motivation behind the basis of processing the data in real-time.

The channel data stream is transferred as a User Datagram Protocol (UDP) stream to a processing server over a 10 Gbit link through the on-board 10 Gbe SFP+ mezzanine cards using the Streaming Protocol for Exchanging Astronomical Data (SPEAD) [101] packet format. At this processing server, the specialized data processing software developed in this work is used to analyze the incoming data stream for radar echo signatures of space debris objects or artificial satellites.

3.3 Stream data processing in radio astronomy

The ever-increasing computational requirements of modern radio astronomy instrumentation have led to the inception of high-performance, real-time computing installations such as those described in [102]. The application of this kind of software systems can be seen in large instruments such as the LOFAR [55] and the SKA [54] radio telescopes.

For instance, the SKA [54], is estimated to produce data in the orders of 10 EB per day [103]. This necessitates the implementation of systems that can process and analyze the data in real-time such that only the most important features of the incoming data are stored for later analysis. Processing of this vast amount of data is a computational challenge. To alleviate the problems arising from the large data volumes being produced by today's largest radio telescopes, many-core architectures, Graphical processing unit (GPU)s and FPGA boards have seen widespread use [97, 104, 105].

Apart from the enhanced capability introduced by state-of-the-art computing hardware, the real-time processing of the incoming data necessitates the use of specialized software algorithms that can operate on a continuous stream of data. Indeed, new stream processing software has become increasingly more popular due to the increasing data processing demand of modern digital telescopes.

In stream data processing, a set of operations are executing continuously on the incoming flow of data as it is received. The processing of data continuously extends beyond the applications of radio astronomy in today's Big Data-era. Nowadays, countless on-line applications generate rapid, continuous and large

volumes of stream data across a vast range of applications including credit transactions in banking and finance and web server logs in large networked infrastructures [106].

This programming paradigm has proved to be particularly useful in real-time processing of digitized voltages from radio telescopes. These radio telescopes make use of tailor-made software that is specifically developed for one particular instrument. The development of such tools requires specialized knowledge. For this reason, the scientific community has been developing more generalized software packages for radio astronomy applications. The aim of these packages is to reduce the development effort that is required to produce new data processing backends for new instruments. To name a few, one can mention Pipeline for Extensible, Lightweight Imaging and Calibration (PELICAN) [107], PSR-Distributed Acquisition and Data Analysis (PSRDADA)⁵ and High Availability Shared Pipeline Engine (HASHPIPE)⁶ data processing frameworks. These software applications are designed to deal with large data throughput. However, [108] reports that these software applications are hard to customize for other application domains. To address this, the Bifrost⁷ framework has been specifically developed to simplify the creation of new data processing software for radio telescopes. Bifrost uses a concise method of creating data processing pipelines in Python that leverage the computing capabilities of the GPU.

While the list of software in radio astronomy is substantial, the number of data processing systems designed explicitly for RADAR application is limited. This is particularly true for the monitoring and tracking of uncooperative space debris objects in Near Earth Orbit (NEO). The data rate of the narrow-band radar system is not as high as those found in radio astronomy applications. However, it is substantial enough to necessitate the introduction of a real-time detection system as shown in the previous section.

In LEO, RSO objects can reach speeds of up to 11 km s^{-1} . At these speeds, the debris crosses the coverage area of the radar very quickly. Previous studies [89] have highlighted the need for a responsive measurement and recording system that is suitable for measurements of highly transient objects such as

⁵ www.psrdata.sourceforge.net

⁶ www.github.com/david-macmahon/hashpipe

⁷ www.github.com/ledatelescope/bifrost

small space debris objects. Such a system can only be realized if the incoming data being streamed from the radio telescope is processed in real-time. In the optical regime, there have been several potential pipeline software, such as the one presented in [109]. However, it is not designed to operate on a continuous flow of data, but rather relies on user input of static images generated by optical instruments.

As the need for new SSA instrumentation grows, so does the need for an easy-to-use, reliable data processing system that are specially built for the detection of orbital objects and whose application extends beyond that of a single instrument. In this work, we present a new software architecture for SST that aims to address these issues. The aim is to simplify the development effort needed to realize a new data processing system that is designed explicitly for phased arrays. To the author's knowledge, this is the first in-depth description of a stream data processing software framework for a space surveillance radar. The architecture of this new software backend, named PyBiraes, is described in the next section.

3.4 Architecture

In recent years, Python⁸ has gained major popularity both within the scientific community and industry. This can be largely attributed to its intuitive syntax and availability of high-end libraries [110]. The developer is shielded from the underlying computing elements such as memory allocation and garbage collection. This expedites the development process and allows the developer to concentrate on the algorithms being implemented. These properties made Python an attractive solution on which to base this software framework presented in this work. Indeed, PyBiraes is written almost exclusively in Python.

Python's abstraction comes at a considerable performance cost [111]. Its reference interpreter, CPython, is considered to be inefficient when it is compared with lower-level languages such as C, C++, and Fortran. As an interpreted language, the Python code is executed line by line rather than compiled into efficient machine code [110]. Also, Python is limited by its Global Interpreter Lock (GIL) that makes sure that no two lines are executed simultane-

⁸ www.python.org

ously [111]. This means that parallelising Python code is impossible unless the GIL is released. Over the years, several strategies have been devised to address these performance shortcomings. Consequently, the fast development approach of Python is kept while its performance constraints are mitigated.

PyBiraless relies heavily on optimized libraries such as NumPy⁹ and SciPy¹⁰. Furthermore, computationally intensive tasks are written in C/C++ and imported in Python. This is achieved through the use of the ctypes library that makes it possible for a Python program to execute arbitrary C functions from a dynamically loaded shared library. In addition, PyBiraless makes use of Python's Numba [112] library¹¹. Numba speeds up the processing of the application by compiling native Python code to native machine instructions using the Low-Level Virtual Machine (LLVM) tool chain. Numba annotated parts of a Python application can achieve a level of performance similar to that achieved by their C or C++ equivalent. The library is still relatively in its infancy and at present, it does not support all statements or data structures such as class and function definitions [110]. This limits its widespread use throughout the codebase.

PyBiraless is a software backend that is made from several distinct components. A high-level representation of PyBiraless is illustrated in Figure 3.7. One may observe that the system follows a three-tier architecture that can be categorized into the presentation, data and application layer.

The presentation tier holds the components that allow an operator of this system to interface with and manage its underlying components. The data produced by the system, such as events and notifications, are presented to the operator at this level. Specifically, the information could include system metrics or detection data.

The managements of these components can become quite complex. This complexity is hidden from the operator through two user interfaces. At this layer, one finds a Command Line Interface (CLI) application and a web-based Graphical User Interface (GUI). Both systems are used to initialise, manage and monitor the software backend. The latter is described in detail in Section 3.10.

⁹ www.numpy.org

¹⁰ www.scipy.org

¹¹ www.numba.pydata.org

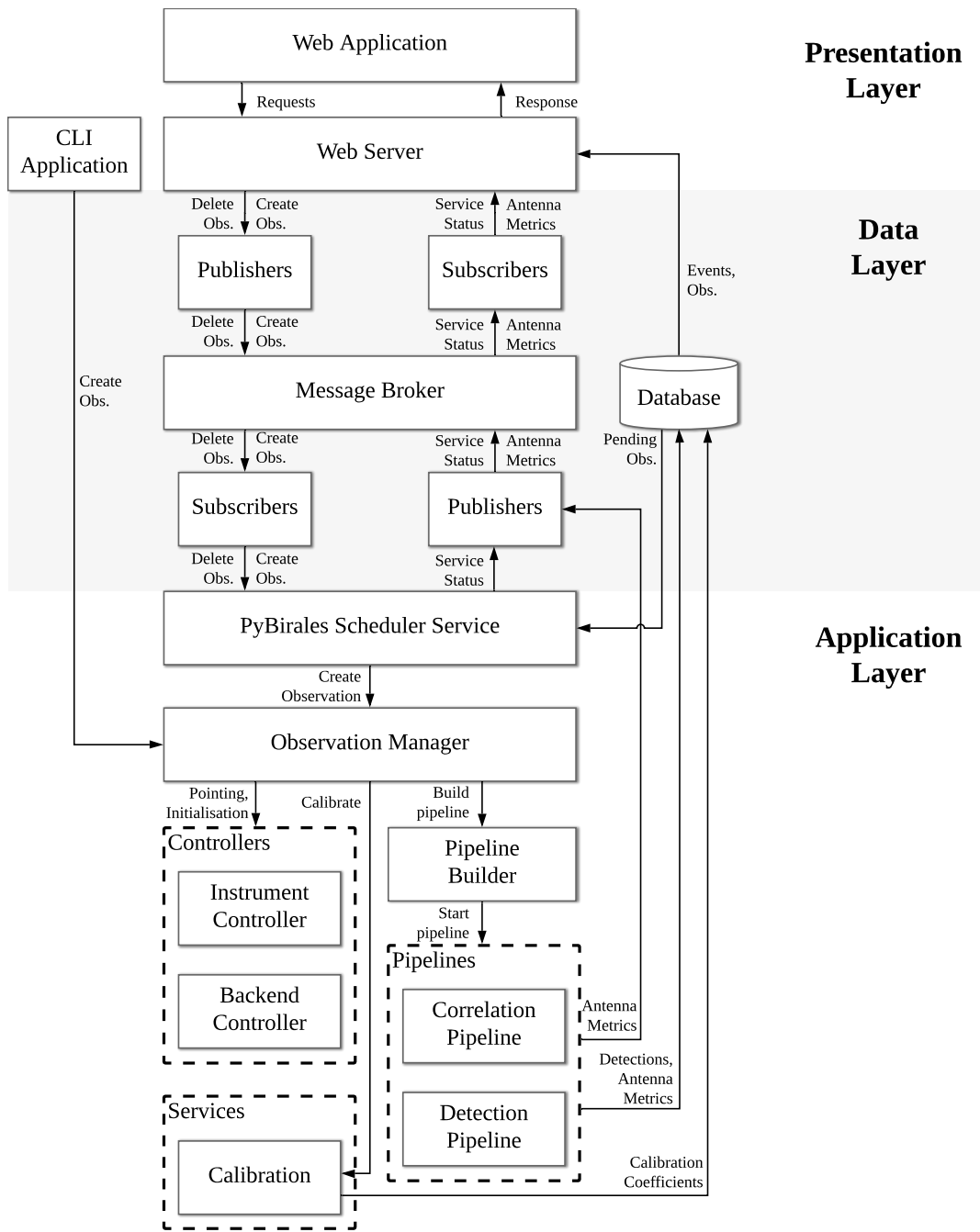


Figure 3.7: An illustration of the three-tier architecture of the PyBiraless space debris processing system

Communication between the application and presentation layers is done through a publish-subscribe messaging pattern implemented at the data layer. PyBiraless uses a REDIS¹² database as a messaging broker between publishers of events and their corresponding subscribers. Typically, the backend system publishes events to the message broker on a specified channel. These events are then consumed by any subscribers or listeners on that channel, such as the web-application.

Events can range from system warnings, or errors, to detection results. A single event can have multiple listeners or subscribers. This way, various aspects of the PyBiraless application, such as the web-application and the backend in the application layer, were decoupled entirely. The application layer contains the software components used in an observation. In BIRALES, an observation consists of several separate stages that are orchestrated by the `ObservationManager`.

An observation first starts by (mechanically) pointing the 8 parabolic cylinders of the BEST-2 array to the desired declination. Secondly, the digital backend is initialized and programmed, such that the antenna data starts flowing through the software backend running on a Fujitsu Celsius R940 processing server. Both the initialization of the firmware and the control of the antennas is achieved through hardware controllers. These controllers manage any hardware that is external to the PyBiraless system. Finally, results are saved to a MongoDB database and presented to the user at the presentation layer.

The `ObservationManager` can be started using either the CLI interfaces or through the PyBiraless scheduler service. This service is a long-running process that listens for user messages and events on the pub-sub system described earlier. The type of message received determines the action taken by the service.

The scheduler service employs a separate worker thread to listen for new events on the message broker. This worker thread interprets the control messages that are published on these channels by the front-end application. These control messages, encoded as JavaScript Object Notation (JSON) strings, can range from system kill messages to the submission of a new observation. For instance, when a new observation is created, the application publishes the details of this observation on the designated channel. This message is received

¹² <https://redis.io>

by the subscriber, in this case, the BIRALES service, which persists it to the database and adds it to the observation schedule. This schedule is a First In First Out (FIFO) queue which hosts the pending observations.

The scheduler service polls the database at frequent intervals to check whether the time for the next observation has elapsed. In such an instance, the observation parameters are sent to the Observation Manager, which orchestrates the separate stages of a SST observation.

3.5 Observation scheduling

In a sophisticated radar system, the allocation of the instrument's resources needs to be carried out in a coordinated fashion. This is mainly because the radar is composed of different components that were not necessarily designed to be used together. This schedule, is the process of allocating the resources ahead of time to perform a series of tasks [113]. In the case of the BIRALES radar, observation time windows from both the transmitter at Sardinia and the receiver at Medicina need to be allocated ahead of time.

The availability of these instruments is typically subject to several constraints, including scheduled maintenance and meteorological conditions. Moreover, both these instruments are not dedicated exclusively to the BIRALES space surveillance program. Instead, the instruments are shared amongst other projects in radio astronomy or SSA. For instance, the transmitter is also used in a separate experimental installation called BIstatic RAdar for LEO Tracking (BIRALET) based in Sardinia [90]. At present, an operator needs to coordinate between both facilities in order to find a suitable time window in which both instruments are available.

Previous studies [114, 115] have identified the difficulty in coordinating an appropriate schedule between different instruments. This is inherently more complex in an optical network of instruments given that their observation window is more limited. To alleviate this problem with optical instruments, Muntoni [89] proposes a unique approach that uses a genetic algorithm to find the optimal schedule for a network of optical instruments. Similarly, this scheduling problem is also present for bi-static radar such as BIRALES.

Figure 3.8 illustrates a typical 24-hour schedule for the bi-static radar. One may observe that one needs to allocate time not only for targeted observation

campaigns but also for calibration purposes. The operator needs to ensure that these observations do not conflict with either a calibration observation nor other time slots reserved for other projects.

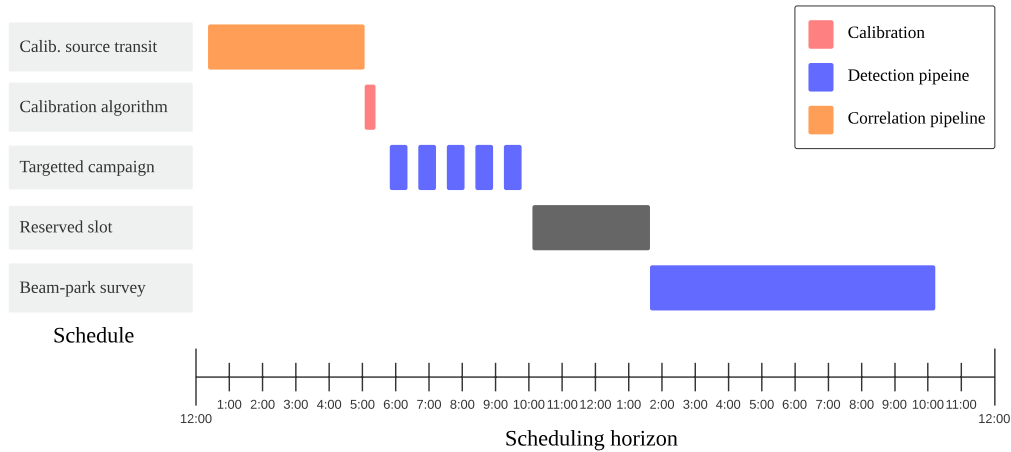


Figure 3.8: An illustration of a typical observation window for the PyBiraless schedule. This schedule illustrates the scheduling of the correlation (orange) pipeline for calibration purposes. The schedule includes short (target) observations for known objects and beam park campaigns for unknown objects (blue). Reserved slots in which the system is not available is shown in grey

An optimized scheduling capability, though useful, is difficult to implement for the BIRALES radar given that the transmitter and receiver are independent and physically separate from each other. This physical separation makes it difficult to automate the allocation of resources. For instance, the transmitter and receiver system is operated by two different schedulers running on two different platforms. Moreover, the ranging and doppler detection block are separate, making the automated start of the two system challenging. This issue is particularly exacerbated by the fact that the two instruments are operated by different institutions.

One proposal is the introduction of a single control system whose purpose is to manage and orchestrate all the components of the whole radar. This centralized approach would then transmit the specific instructions to the inter-networked facilities making up the BIRALES radar. Only with the introduction of this parent control system can a more advanced scheduler be put into place. Potentially, the introduction of such a system could pave the way

for the experimentation of a Multi-Static radar system such as the ones investigated in EISCAT [45] and MeerKAT [116] space debris radar installations.

In the absence of such a system, the current version of the PyBiraless scheduler has allowed the operators of radar to efficiently allocate the observation windows ahead of time in a semi-automated fashion. In a targeted campaign, the targets of interest are supplied to INAF by the Italian MoD. A preliminary schedule is generated by INAF together with researchers from the Politecnico di Milano. In a targeted campaign, the schedule includes the time at which the targets are predicted to cross the bi-static radar's coverage area along with the respective pointings of the transmitter and receiver antenna.

Once the targets of interest are agreed upon by all the participating parties the schedule is submitted to the BIRALEs processing server in the TDM format. The TDM file is processed and persisted to the database. Alternatively, individual observations can also be queued manually through the web-based front-end.

3.6 Hardware Controllers

A controller encapsulates the logic needed to interface with a component. For instance, the BEST-2 array can be controlled using the `InstrumentController`. On initialization, this controller loads the antenna singleton object. Singleton objects were used to make sure that a single instance exists across the whole application. This avoids the scenario in which multiple objects send conflicting commands to the same hardware component. The `InstrumentController` can be used to get the current pointing of the antenna. It can also be used to instruct the antenna to move to a new declination.

Similarly, the `BackendController` is used to interface with the ROACH-based digital backend. Principally, this controller is used to load and start the digital backend singleton object. The singleton object, in this case, makes use of the Corr Python library¹³ to interface with the digital backend. The Corr library is a general-purpose control framework for ROACH-based devices such as the ones used for the BEST-2 digital backend.

¹³ <https://casper.berkeley.edu/wiki/Corr>

Controllers provide an abstract representation of the instruments together with a concise method of interacting with the underlying hardware. This way, the intricate implementation details are hidden from the developer. Indeed, both the aforementioned controllers facilitate the initialization and termination of the component that they are responsible for. Upon initialisation of the digital backend, the data starts to flow to the processing server on which the data processing facilities implemented in this work are installed.

3.7 Data processing pipelines

The incoming data is processed using what are known as data processing pipelines. In computer science, pipelines are a popular design pattern that are used in the processing of a continuous stream of data. Pipelines are administered by a pipeline manager that is responsible for the initialization, processing and graceful termination of a pipeline.

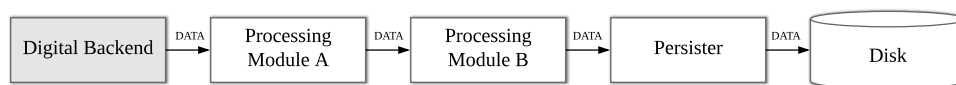


Figure 3.9: A graphical representation of a linear software pipeline illustrating the processing of data through a chain of modules. In this pipeline, antenna data received from the digital backend are processed at modules A and B and persisted to the disk using a dedicated module

A pipeline is made up of a chain of separate processing stages, as shown in Figure 3.9. At each processing stage or module, the incoming data are mutated and passed over to the next processing stage in the chain. This process is repeated indefinitely until the processing module, together with the rest of the modules, is stopped by the pipeline manager. A processing module is stopped by flipping a stop event flag. In PyBiraless, several modules are available. These can be split into three categories.

Generator modules read data from an external entity and encode the data in such a manner that is forwarded to the next processing module as output. Generator modules include the `ReceiverModule` that reads the incoming antenna voltages and the `RawDataReader` which is used to read raw antenna data that has been previously persisted to disk from a past observation using

the corresponding `RawDataPersister` module. Generator modules are usually used at the start of the processing pipeline. They are designed to feed the processing data continuously until the processing pipeline is stopped (in the case of the `Receiver` module) or data is finished (in the case of the `RawDataReader` module).

Processing Modules consume and transforms a chunk of the data stream. This chunk of data, also known as a data blob is forwarded to the next module in the pipeline. Processing modules include the `Channeliser` module that is tasked with channelizing the antenna signals, and the `Beamformer` module which is used to generate several beams within the instrument's FoV.

Lastly, **Terminator** modules accept data as input but do not forward the data to another module. This module is usually the last module of a processing pipeline.

In PyBirales, different pipelines can be built depending on the problem being solved. For instance, one pipeline can be built to correlate the antenna signals offline while another would be used to process the data for radar echoes. In either case, the processing pipelines in PyBirales are designed to process the data in real-time. This means that the following real-time condition at each module is met,

$$\text{processing time} < \frac{\text{Number of samples}}{\text{Sampling rate}} \quad (3.13)$$

For instance, if PyBirales is processing 2^{18} samples, at a sampling rate of 78 125 samples/s, the data should be processed in less than ~ 3.36 s for the real-time condition to be satisfied.

The construction of these pipelines can become a bit cumbersome for advanced applications. To facilitate this, and speed up the development process, PyBirales implements a framework that can generate a processing pipeline with ease. This framework makes it possible for a pipeline to be assembled by chaining together several pre-built modules that are shipped with PyBirales.

3.7.1 Pipeline builders

A pipeline manager builder implements the Builder design pattern to simplify the process of creating a complex pipeline manager. As shown in Figure 3.10, a detection pipeline is built by calling the `build()` function of the corresponding

(concrete) builder class. This class takes care of the assembling the processing modules into a pipeline.

A pipeline is started through a call to the pipeline `start()` function. This function starts the processing modules which are run in a separate thread. Once started, the data flows from one module to the next in a linear fashion. In PyBirales, this is achieved through data blobs.

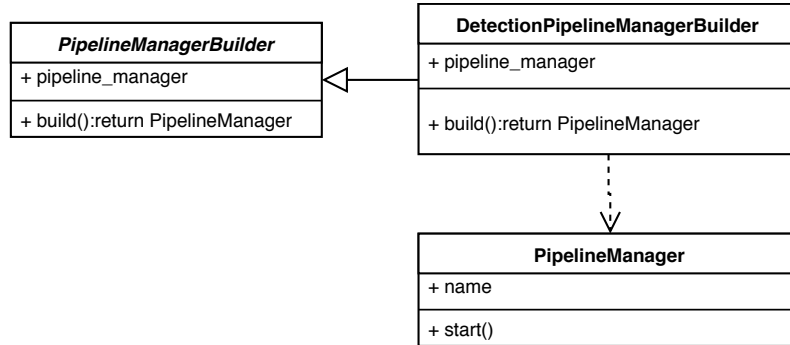


Figure 3.10: A UML Class diagram of the pipeline manager builder

3.7.2 Data blobs

The unit of data on which modules operate are known as data blobs. A module consumes a data blob and outputs a new data blob to the next processing module within the pipeline. The output blob can consume one particular data blob type and output another of a different type.

Data blobs are encoded as multi-dimensional NumPy arrays that act as fixed-sized circular buffers between two processing modules. Circular or Ring buffers are a popular data structure in the management of memory buffers in the processing of stream data in radio astronomy. In PyBirales, the data blob is made up of several blocks as specified by its buffer factor. These blocks are the smallest unit of data being consumed or produced by a processing module in PyBirales. A module reads or writes a single block into a blob at any given time.

A block can be described by its data type and dimension. These two parameters are used as a validation check to make sure that the data blob used between a producer and a consumer module is compatible. For instance, Figure 3.11 illustrates a graphical representation of a single block within a typical data blob. The blob consists of three blocks each of size $N_s \times N_c \times N_b$,

where N_s is the number of samples, N_c is the number of channels and N_b is the number of beams being processed.

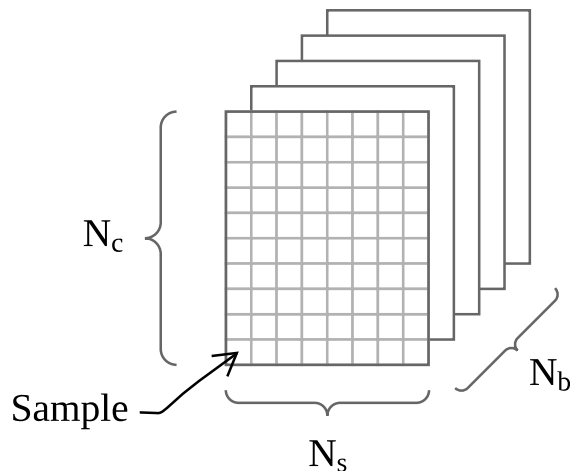


Figure 3.11: A graphical representation of a data block in PyBiraes of size $N_s \times N_c \times N_b$

The memory complexity of a pipeline in PyBiraes is largely dependent on the number of data blobs that are used to solve a given problem. This also depends on the buffer factor. For a blob of buffer factor B , the memory complexity is given as $\mathcal{O}(BN_cN_bN_s)$. In a pipeline making use of N such data blobs, this becomes $\mathcal{O}(NBN_cN_bN_s)$. Thus, for 5 double-precision 8 byte blobs, with a buffer factor of 3, operating on 8192 channels, 32 samples and 32 beams, the memory requirements of such a pipeline is 0.96 GB.

Figure 3.12 shows how data flows from one module to the next. The circular buffers make use of two pointers or indices; a read and a write pointer. A producer module writes the processed data to a block in the array specified by the write index. Upon completion, the write index is incremented to the next location. When the index reaches the end of the array, it is reset to the start, thereby overwriting the oldest block of data in a circular fashion. Similarly, a read pointer keeps track of the last location read by a consumer module. Once a block is read by module B, the read index is incremented. Data can be lost if the producer module tries to overwrite a block in a location which has not been read by the consumer module.

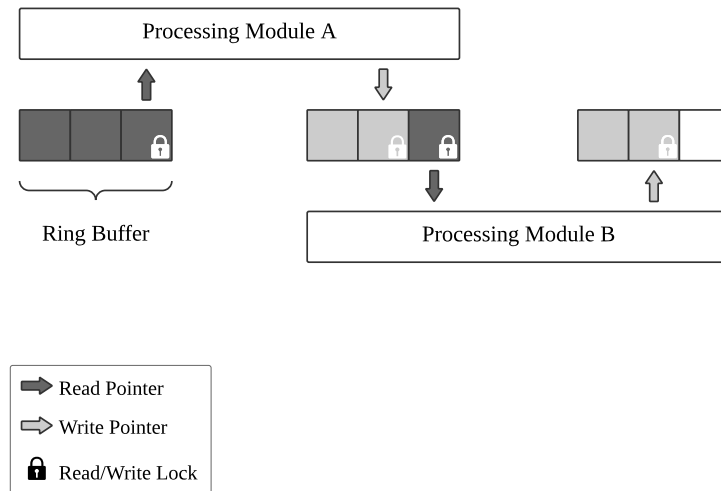


Figure 3.12: An illustration of the use of ring buffers (buffer factor = 3) by two Processing modules A and B acting as a producer and consumer respectively

Furthermore, a race condition could arise given that the data blobs are being accessed by a least two module threads at any one time. One module could be trying to write to a block in an array while the other module is trying to read. This is avoided by using a locking mechanism upon reading and writing. As shown in Figure 3.13, when a module tries to modify its output blob, which is an input blob to the next module, a write lock request is issued. When the module is finished with writing to the blob, the lock is released. A similar approach is used for reading requests.

The architecture of the PyBiraless system, together with the main components making up a streaming data processing pipeline was discussed in the previous sections. In the next sections, two data processing pipelines will be described to demonstrate the use of the concepts introduced thus far. First, the correlation pipeline is described. This is followed by the introduction of the PyBiraless detection pipeline.

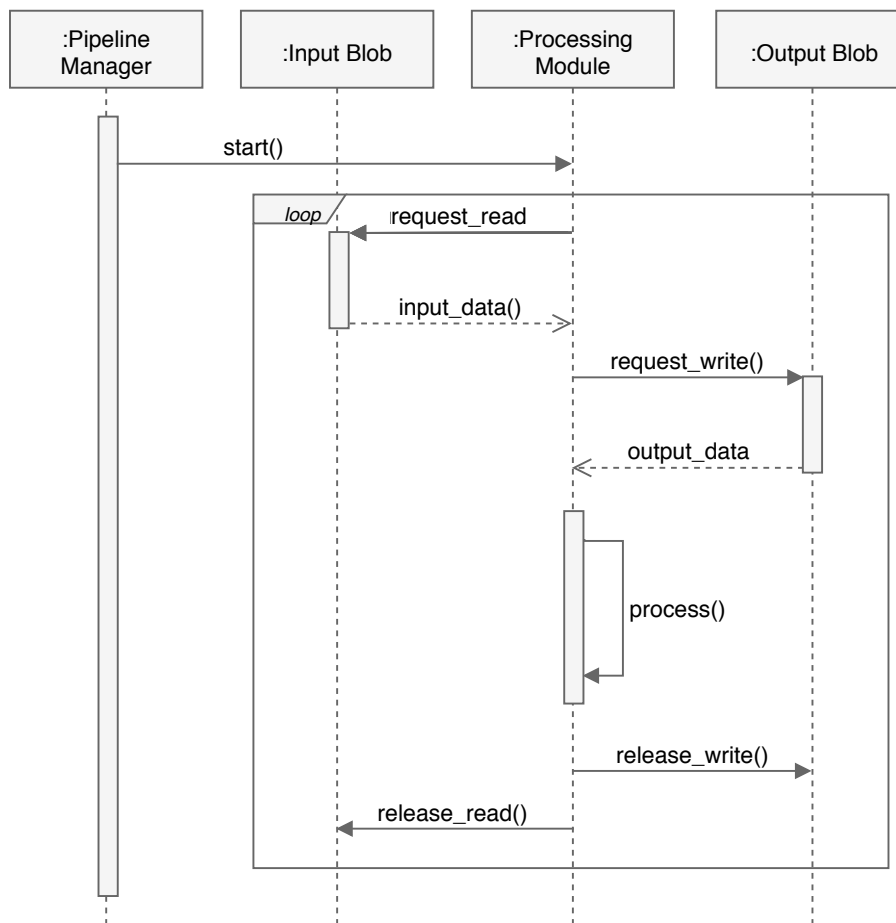


Figure 3.13: A UML sequence diagram of the concurrency pattern of a typical processing module in PyBiraes

3.8 Correlation pipeline

The correlation pipeline, shown in Figure 3.14, is used to generate the correlation matrix that is used for calibration purposes. This correlation matrix is populated with baseline visibilities as a calibrator radio source transits over the FoV of the radio telescope. The pipeline is started several minutes before the radio source transits the local meridian, with the radio telescope being pointed at the source's declination.

The correlation module receives data from the digital backend and computes the correlation between the input from each pair of antennas, or baselines. This is performed for all the channels at each integration step which is currently configured to be 131 072 samples (~ 1.667 s).

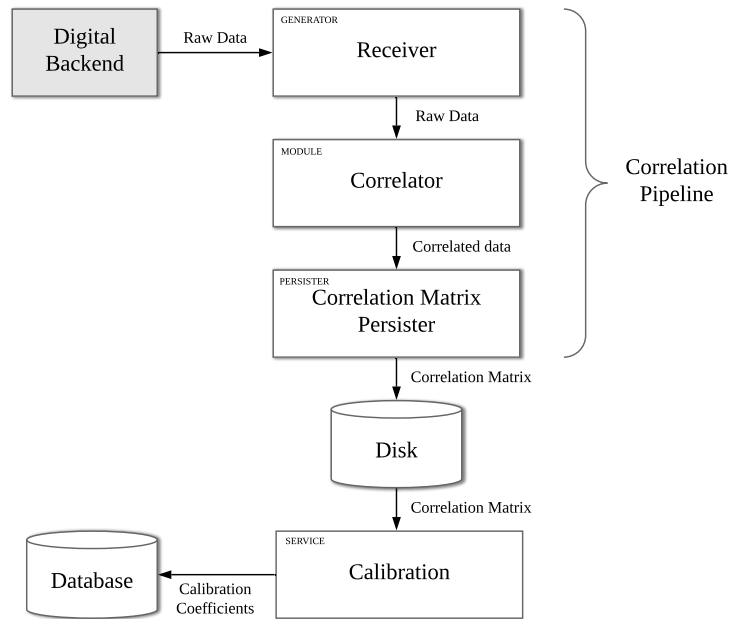


Figure 3.14: Illustration of the BIRALES correlation pipeline that is used to calibrate the BEST-2 array

In the correlation pipeline, the correlated data from the correlation module is fed to the `CorrelationMatrixPersister` module, which dumps the matrix to disk as a Hierarchical Data Format 5 (HDF5) file. As described in Section 2.3, the correlation matrix is used by the calibration algorithm to generate the calibration coefficients. These coefficients are used to compensate for the instrumental phase and gain errors.

3.9 Detection pipeline

The PyBiraless pipeline framework was used to build a detection pipeline that is tailored for the detection of high-velocity RSO in LEO. A schematic representation of the modules making up the space debris detection pipeline is shown in Figure 3.15. The data from the digital backend is interpreted using the `Receiver` generator module. The incoming array signals are subsequently beamformed and channelised before being fed into the detection system. The detection system is central to the detection pipeline, and it consists of three distinct modules. The detection data extracted by the `Detection` module is

then saved to the database. A detailed description of each step in the detection pipeline is given in the following sections.

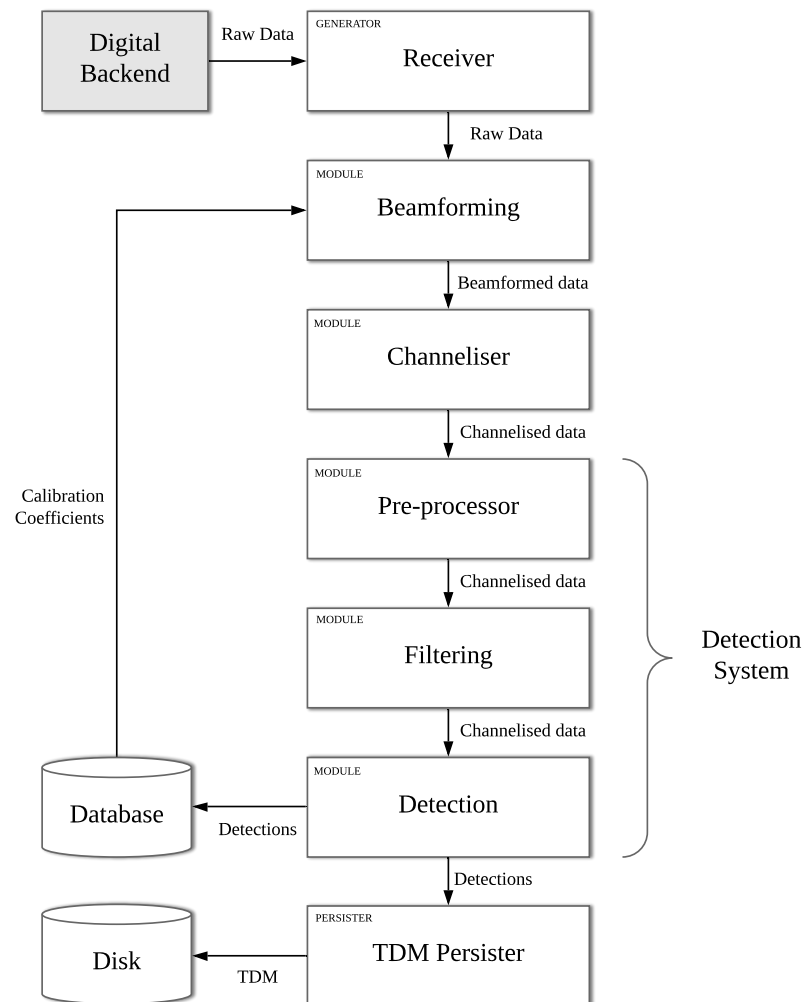


Figure 3.15: Illustration of the BIRALES data processing pipeline for the detection of orbital debris

3.9.1 Data acquisition

The first module in the detection pipeline is the **Receiver** generator module which reads the data coming from the digital backend. The format of the transmitted data is a 32-32 complex fixed-point format, which is translated to floating-point. In order to do so, the receiver uses the Data Acquisition (DAQ) library developed for the Antenna Verification System (AAVS) prototype of the

Low-Frequency Aperture Array (LFAA) [117] which was extended to accept the BIRALES data format. The receiver module reads the incoming data in chunks, converts the data into data blobs and forwards this data to the second module in the pipeline. The data generated by the receiver can also be persisted to disk. This is achieved by chaining the receiver module to a persister module that can persist the raw input data to disk. This file encodes the phased array's raw data which can be subsequently processed in offline mode.

In offline mode, the pipeline uses a separate data reader module that reads this binary file in chunks in a similar fashion to the `Receiver` module. Each chunk is converted into a `RawDataBlob` that is forwarded to the next processing module in the pipeline. Hence, the system can run both in offline mode using the `RawDataReader` module and in online mode using the `Receiver` module as the first module of the pipeline. This way, the next module in the pipeline is not concerned as to whether the pipeline is running in offline or online mode, as both reader modules output the same data blob format.

3.9.2 Beamforming and multi-pixel generation

The next module of this pipeline is the `Beamformer`. Beamformers are designed to enhance the signals coming from some directions while suppressing the signals and noise arriving from other directions. In conventional beamforming, the weights and parameters that define the resultant beam pattern of an array are fixed. The weights are chosen to produce a specific antenna array response in a particular direction in the presence of interference [118].

In Section 2.2 (Equation 2.18), it was shown that the pointing direction of a phased array can be steered to point in any direction within the instrument's FoV. The point at which the signals add constructively can be changed by varying the phase shift applied to the antennas signals. Thus, a beam can be steered to point in any direction within the instrument's FoV. In PyBiraless, the generation and steering of a beam from the individual antenna signals is realised by the `Beamformer` module. Additionally, the calibration coefficients, correcting for any instrumental errors, are applied on the received signals at this stage.

As the number of antenna elements combined to form a single beam is increased, so does the sensitivity of the instrument. Figure 3.16 shows the

received power of a single beam as a function of the number of elements used for an observation of an astronomical source (Cassiopeia A). One may observe that upon doubling the number of elements, and hence the collecting area, the antenna gain is increased by around 3 dB. This indicates that the element pattern is being summed coherently.

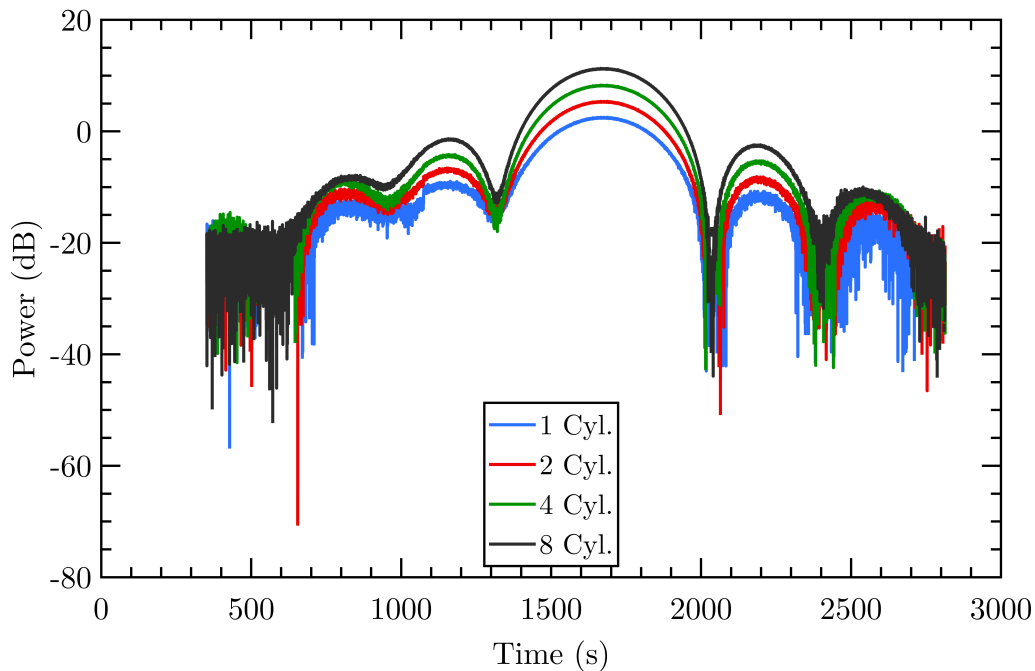


Figure 3.16: The increase in sensitivity of the instrument as the number of elements is doubled. Cassiopeia-A observation on the 14th of September 2019

This work investigates whether the trajectory of an orbiting object can be estimated by a multi-beam receiver. In BIRALES, multiple beams, each with a different pointing direction, can be created from the same input by copying the input signal and applying a different phase shift. The arrangement of these beams within the FoV instrument is referred to as the multi-beam configuration.

As the high-velocity object crosses the FoV of the BEST-2 array, the doppler echo is received across multiple beams. A successful detection of this echo within a beam is henceforth referred to as a *beam illumination*. Each beam is associated with a specific pointing in azimuth and elevation. The sequence at which these beams are illuminated can be used to extrapolate the path taken by the orbiting object over the array. This data, together with the doppler shift and ranging data, are used by the tailored orbit determination algorithm

to determine an initial orbit for the object [119]. The implication is that an accurate model of the BEST-2's multi-pixel is an important prerequisite for the BIRALES SSA radar.

The arrangement of these beams within the FoV of the array is completely configurable. Earlier studies [120] used a multi-pixel of 32 beams which are electronically steered inside the instrument's 5.7° by 6.6° FoV. This configuration is shown in Figure 3.17. The elevation and azimuth angles are the angular deviations with respect to the array's pointing direction.

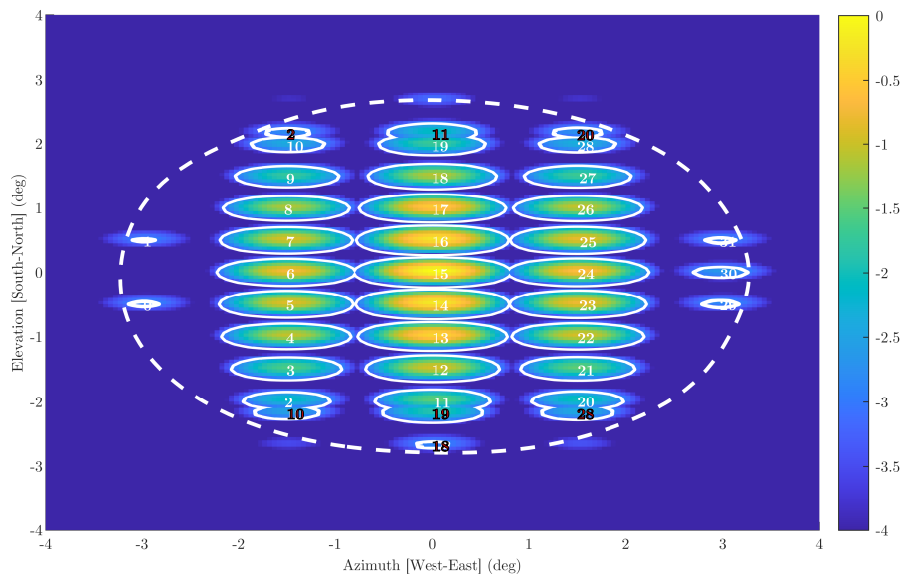


Figure 3.17: The default multi-pixel configuration of the BIRALES radar. The large ellipse (dashed) shows the single element pattern at -3 dB. The beams that are affected by ambiguity due to grating lobes are highlighted in red

This approach tries to fill the available FoV in order to increase the coverage area, thereby increasing the probability of detection of an object. However, one may note that grating lobes, marked in red, appear at an offset of 4.2° in the H-Plane (for the end-fire case). Moreover, pointing errors as a consequence of quantisation, can be noted at large steering angles in the E-Plane.

In Chapter 2, we saw how these ambiguities can be minimised if the steering angle from broadside is decreased. Inevitably, this reduces the radar coverage area since the beams are more densely packed together. An optimal beam configuration should minimise the pointing errors associated with spatial aliasing while maximising the total area covered by the beams. Moreover, the arrangement of the beams should make the most efficient use of the FoV possible use

of the available area by minimising the overlap between the beams. Thus, one needs to find a compromise between beam coverage and the effect of spatial aliasing. Figure 3.18 shows an alternative beam configuration that attempts to minimise the pointing errors while making the most efficient use of the available area.

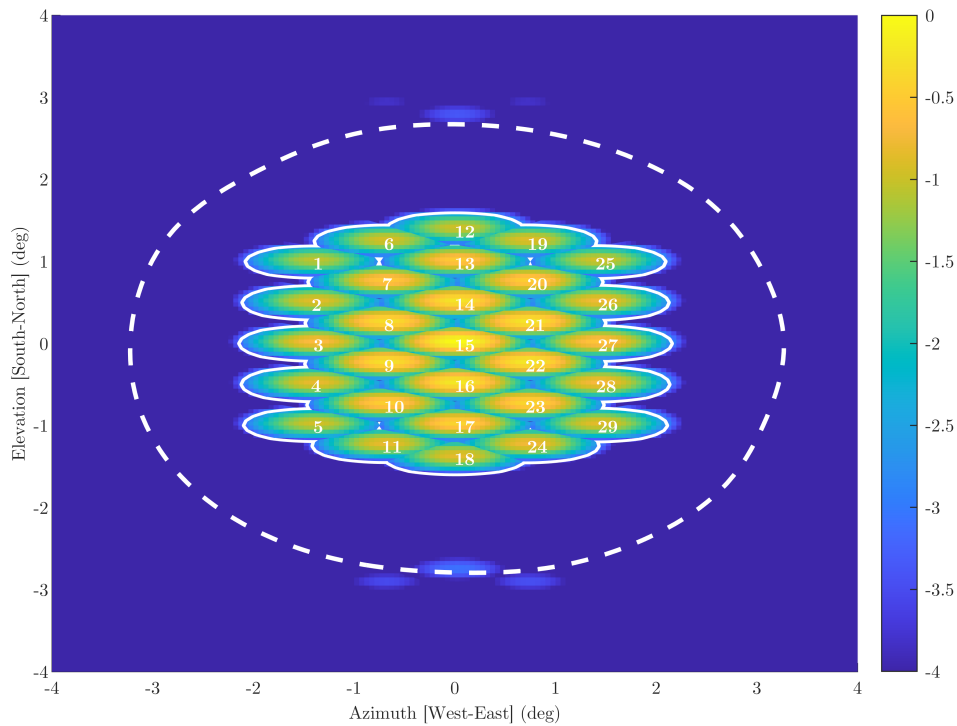


Figure 3.18: An alternative multi-pixel configuration of the BIRALES radar showing the reduction of the pointing errors as well as spatial aliasing if the beam packing factor is improved. This improvement compromises the coverage area when one compares it to the previous multi-pixel configuration

One can note that tessellating these beams in such a configuration effectively reduces the pointing deviation, thereby reducing the uncertainty in the target's trajectory. Additionally grating lobes do not appear at -3 dB using this configuration. Given the number of parameters, it could be interesting to investigate the use of evolutionary techniques, such as genetic algorithms, to find the optimal configuration of beams. In this case, the fitness function for the genetic algorithm would take into consideration the number of beams used to form the multi-beam, the area covered, degree of beam overlap and pointing deviation.

The number of beams generated, together with their pointing, is configurable and can be specified by the operator of the PyBiraless software backend.

The computational expense grows with the number of beams generated. In fact, the complexity of the module is $\mathcal{O}(N_c N_b N_s N_a)$, where N_b is the number of beams, N_c is the number of channels, N_s is the number of samples and N_a is the number of antennas.

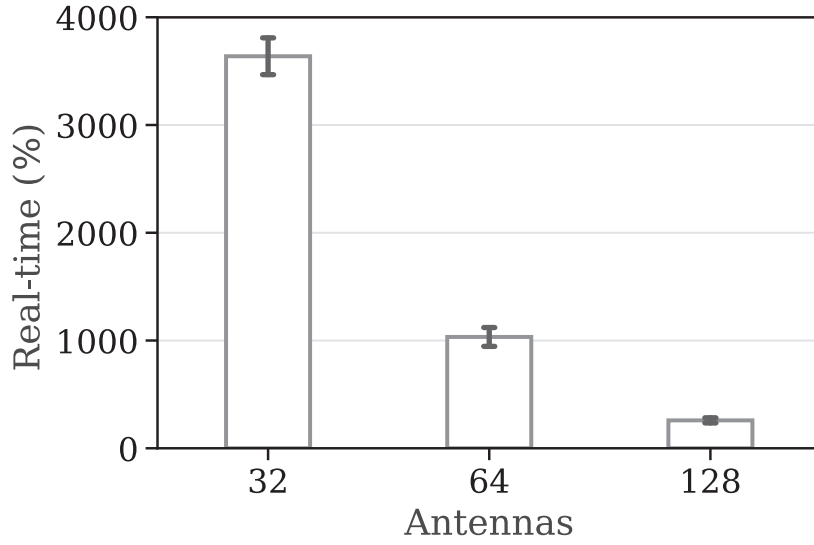


Figure 3.19: Benchmarking of the `Beamformer` module. The mean processing time is normalised to the real-time criteria. Error bars represent the associated standard deviation

Figure 3.19 shows the performance benchmark for the `Beamformer` module in `PyBirales`. The `Beamformer` module is a Python wrapper to a multi-threaded routine written in C++. The beamformed data is encoded as a `BeamDataBlob` of shape (channel, sample, beam) where B_n represents the beamformed data in beam n .

One can note that the module can process up to four times the current data rate within the real-time constraint. This is equivalent to generating up to 128 independent antennas. The benchmarks described in this section were measured on a processing server running the latest version of the `PyBirales` software (ver. 3.0.1) running on Ubuntu 16.04 on an Intel Xeon E5-2686v4 CPU with hyper-threading enabled and having 32 GB of memory.

3.9.3 Channeliser

The wide-band nature of most radio telescopes means that they cannot be used directly as for the monitoring of LEO objects. The channel bandwidth is too wide for the detection of small signature objects such as space debris. The bandwidth selection of a radar system needs to take into account several considerations. On the one hand, Chang et al. [71] state that the advantage of using a narrow bandwidth reduces the receiver noise since it is less likely to be affected by RFI sources within that narrow band. On the other, the channel needs to be wide enough to allow a drift in the central frequency that will enable accurate and precise measurement. Thus, the channel bandwidth cannot be smaller than the maximum Doppler shift that is expected by the targets, in this case, high-velocity RSOs.

Analysis of the expected doppler ranges from TLE data reveals that the expected doppler shift is in the range of a few kilo Hertz. In the case of the BEST-2 array, the 78 125 Hz input channel needs to be channelised further. The power spectrum of the incoming signal $x(n)$ of length N can be computed by making use of a Discrete Fourier Transform (DFT), denoted by $X(k)$,

$$X(k) = \sum_{n=0}^{N-1} x(n) \exp(-2\pi ink/N) \quad k = 0, \dots, N-1 \quad (3.14)$$

Evaluating this expression directly requires $\mathcal{O}(N^2)$, which is computationally expensive. As an alternative, the Fast Fourier transform (FFT) is often used. The FFT is a computationally efficient algorithm that computes the DFT and reduces the computational complexity to $\mathcal{O}(N \log_2 N)$ [121]. An unwanted consequence of FFT channelisation is a phenomenon called spectral leakage in which the unitary response of a channel with a central frequency μ_c is not uniform, but is characterised by a non-zero response outside its pass-band. This results in leakages into its neighbouring frequency channels. This is a major concern in applications that are characterised by strong narrowband signals such as RFI.

Another undesirable effect of channelisation is the non-ideal shape of a channel's response, causing a narrowband signal to be attenuated at the edge of the channel. Thus, a Polyphase Filter Bank (PFB) channelizer was used since leakage is significantly less. A PFB is an implementation of a filterbank, that consists of a prototype polyphase Finite Impulse Response (FIR) filter frontend

followed by an FFT [122, 123, 124]. The input signal $x(n)$ is decomposed into P branches, or phases, denoted by $x_p(n')$.

The branches are put into a buffer of length M until $M \times P$ samples are buffered. Each branch is multiplied by the corresponding filter coefficients $h_p(m)$ which was decomposed into M taps. The output from each branch-coefficients product is summed over all the taps to obtain $y_p(n')$ [125],

$$y_p(n') = \sum_{m=0}^{M-1} h_p(m) x_p(n' - m) \quad (3.15)$$

Subsequently, the output of each branch is then fed to into a DFT with P inputs and the next P samples are read in an iterative fashion,

$$Y(k, n') = \sum_{p=0}^{P-1} y_p(n') \exp(-2\pi i k p / P) \quad (3.16)$$

Substituting Equation 3.15,

$$Y(k, n') = \sum_{p=0}^{P-1} \sum_{m=0}^{M-1} [h_p(m) \exp(-2\pi i k p / P)] x_p(n' - m) \quad (3.17)$$

The incoming data from the 32 antennas, is fed into the PFB `Channeliser` module implemented in PyBirales. The `Channeliser` splits the coarse channel of bandwidth B into N channels with a channel resolution given by $\Delta\mu = B/N$. The channel is split into 8192 separate channels giving a spatial resolution of ~ 9.5 Hz. This gives a temporal resolution Δt of ~ 0.10 s as given by the FFT constraint,

$$\Delta t \Delta \mu = \frac{1}{N} \quad (3.18)$$

While the PFB minimises the spectral leakages in adjacent channels, a radar signature can be detected across multiple channels within the same time epoch. This phenomenon, known as doppler migration, manifests itself in radar streaks with a high SNR. This causes the reflected radiation to be detected in one channel to leak into the adjacent channels as a consequence of the FFT channelisation being used. The PFB channeliser minimises this effect when compared to a standard FFT channelizer. In this work, doppler migration is handled by considering only the channel with the highest SNR per time epoch. This is usually the one at the centre of the Doppler spread.

Channelising the data using a PFB as opposed to a direct FFT adds a slight overhead. The computational complexity is $\mathcal{O}(N_c N_a (\log_2(N_c) + 8N_t))$, where N_a is the number of antennas, N_c is the number of channels, N_t is the number of taps. The PFB channeliser implemented in PyBiraes run on a single thread and makes use of the Numba library [112] in order to speed up this computation.

Figure 3.20 shows the performance benchmark of the `Channeliser` module with an increasing number of antennas. The channeliser is capable of processing the incoming data from 32 antennas at 4-times the real-time criteria. Indeed, even if the data rate is doubled, the channeliser can still handle it comfortably. However, one can note that when scaling to 128 antennas, the channeliser can barely process this data in real-time. This suggests that the current version would need to be optimised further for it to be able to handle the data rate from 128 antenna elements, or half, of the parabolic reflectors installed at the Northern Cross.

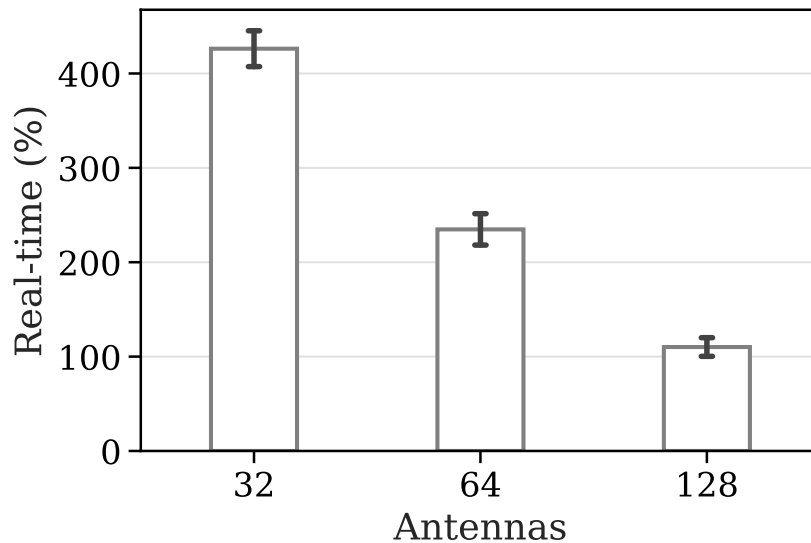


Figure 3.20: Benchmarking of the `Channeliser` module. The mean processing time normalised to the real-time criteria. Error bars represent the associated standard deviation

The PFB channeliser produces channelised data blobs that are essentially a spectrogram of M channels by N time samples. The spectrogram is a series of Fourier transforms combined together such that the image becomes a visual

representation of the power P_n received across a band of frequencies w over time [126]. Therefore, the generated spectrogram can be formally defined as:

$$S = [S_{ij}]_{N \times M} = \begin{pmatrix} P_0(w_0) & P_0(w_1) & \cdots & P_0(w_{M-1}) \\ P_1(w_0) & P_1(w_1) & \cdots & P_1(w_{M-1}) \\ \vdots & \vdots & \ddots & \vdots \\ P_{N-1}(w_0) & P_{N-1}(w_1) & \cdots & P_{N-1}(w_{M-1}) \end{pmatrix}$$

where $i = 0, 1, \dots, N - 1$ is the time frame, $j = 0, 1, \dots, M - 1$ is the frequency bin. If this is represented as an image, the vertical axis represents time whilst the horizontal axis represents the discrete frequency steps. The intensity in a spectrogram image represents the power measured at each time-frequency point.

High-velocity objects crossing the field of view of the instrument are characterised by a frequency signal that changes linearly with time. Figure 3.21 illustrates a typical spectrogram generated by the `Channeliser` module. One can note that this spectrogram shows the radar echoes of two distinct RSOs objects at $t = 100$ and a faint streak at $t = 280$. The former was correlated with a US CELESTIS TAURUS rocket body¹⁴ (launched in 1998) having a RCS of 3.752 m^2 at a perigee of 782.1 km. The latter and fainter streak could not be correlated with a catalogued object.

In radio astronomy, the spectrogram is used to record and measure the spectral content of the signals received by astronomical sources [105]. Similarly, the analysis of the spectral contents of a spectrogram generated after channelisation reveals the details of the radar echoes reflected off the target objects entering the radar coverage area of the BIRALES radar. This linear streak in the generated spectrogram is the pattern that is to be detected by the subsequent modules in the detection pipeline.

3.9.4 Detection

The final stage of the space debris detection pipeline is the `Detection` module. The aim of this module, described in detail in the next chapter, is to analyse the spectrogram for radar echoes backscattered from space debris targets. When

¹⁴ <https://www.n2yo.com/satellite/?s=25160>

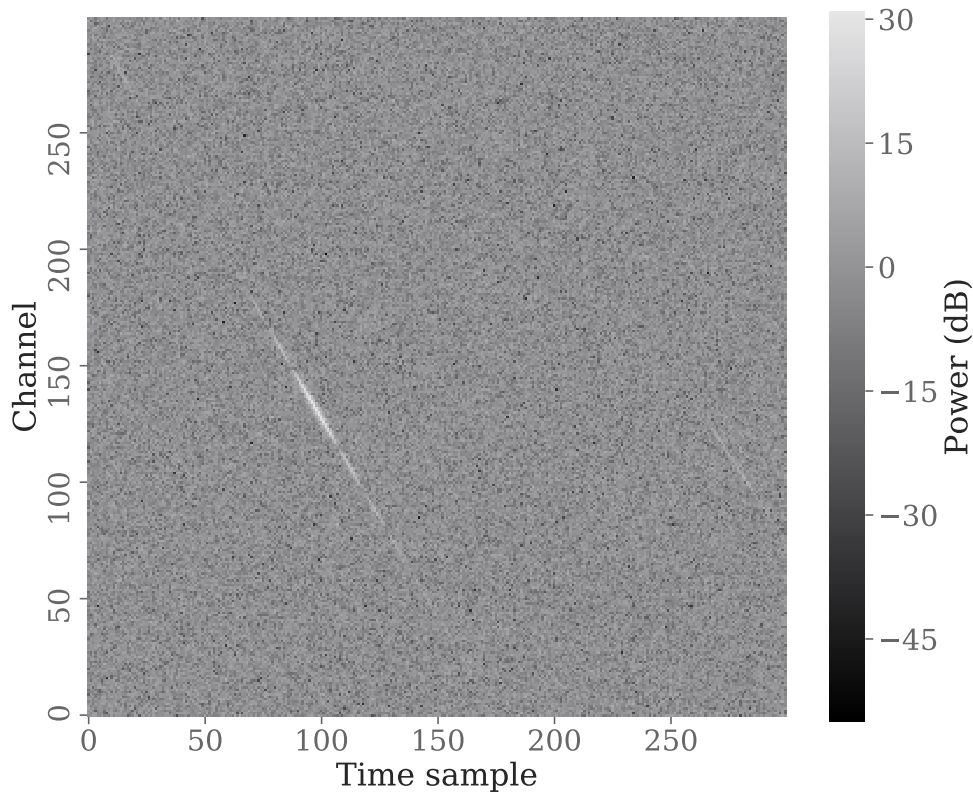


Figure 3.21: A subset of the channeliser output for a single beam that illustrates the radar signature of a US CELESTIS TAURUS rocket body in the presence of background noise. NORAD 25160 detection on February 11th, 2019

detection of a space debris target is made, an asynchronous event is fired. The space debris event listener handles such events by persisting the detection data to the database to be later retrieved by the monitoring front-end described.

The detection data is saved in TDM [93] format, which encodes metadata of the observation, such as the start time of the observation, transmitter frequency and instrument information. The file is sent over an SFTP connection to a remote server owned by the MoD. On the remote server, the orbital determination block developed by researchers at the Politecnico di Milano, Italy [94] is run.

The tailored algorithm makes use of the beam illumination sequence, SNR, slant range and Doppler shift together with the configuration of the multi-pixel. These parameters are used to both estimate the path taken by the transiting object within the receiver's field of view and to refine the orbital parameters of known RSO. In the case of unknown objects, the algorithm performs an initial

orbit determination for the object. A detailed description of the algorithm is given in [94].

3.10 Frontend

In this chapter we have described the components of the BIRALES radar processing backend ranging from its hardware controllers to its data processing facilities. The orchestration of these various components can become quite complex. The operation of this radar is facilitated through the use of a web-based front-end application that comes shipped with PyBirales. This front-end was designed to be a consolidated approach for both the monitoring and control of the BIRALES radar. A web-based monitoring and control application that is decoupled from the inner workings of the processing framework has also been adopted amongst newly-commissioned radio instruments such as the AAVS SKA path-finder [127] and the Mexican Array Radio Telescope (MEXART) radio telescope [128]. Indeed, such an application has been in the works for the more-established BiFrost pipeline framework [108].

Figure 3.22 illustrates the components that make the front-end part of the system. One can observe that the front-end makes use of two servers. A Flask web-server is used to render the web pages to the client. The web server is also used to issue commands to the PyBirales backend. This is done through the pub-sub system described in Section 3.4.

Events and metric information are sent to the client-side through a Socket.IO¹⁵ server. Socket.IO is a real-time transport protocol that is used to realise an event-driven communication between a web browser and a server. In traditional applications, the client-side component polls for changes to a server. In a socket-based implementation, events are pushed to the client as soon as they arise. Using Socket.IO, PyBirales implements a monitoring framework that pushes notifications, antenna metrics or events to the user in real-time.

This event-driven approach was used to monitor the status of the PyBirales system that is running as a separate process. The system pushes a Keep Alive (KA) message to the web-server which is subscribed on the pub-sub channel.

¹⁵ <https://socket.io/>

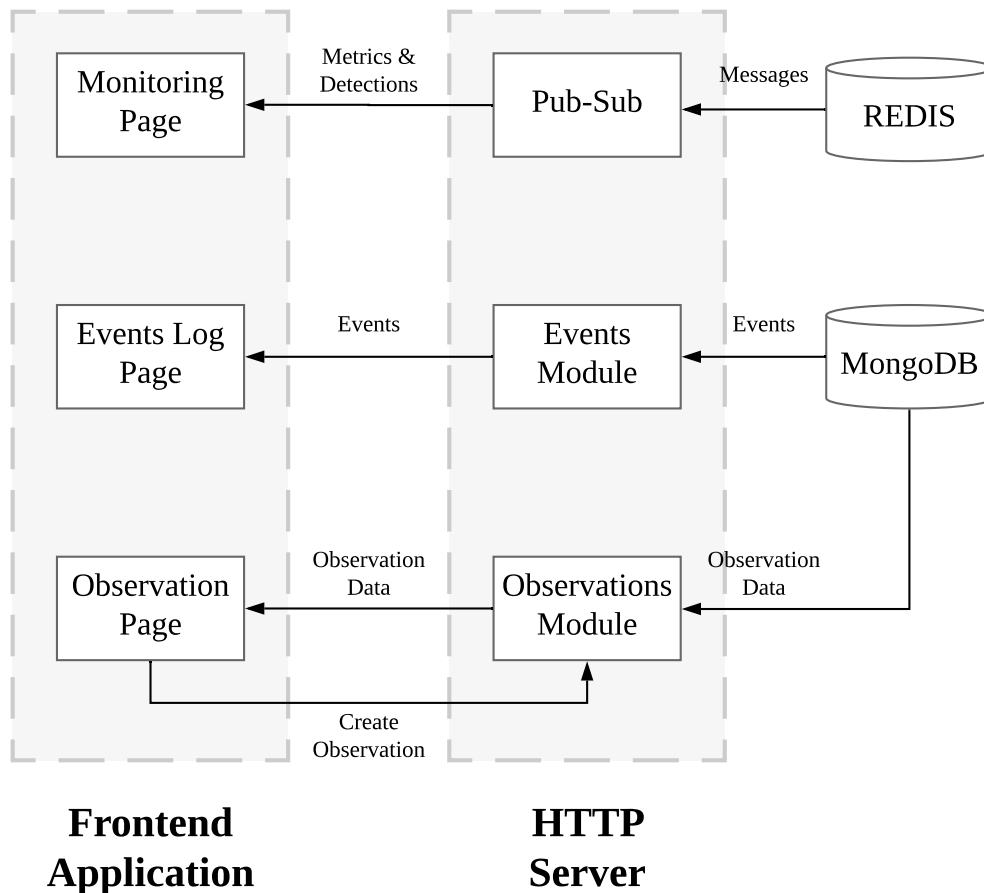


Figure 3.22: A block diagram of the web-application

The web server forwards this message through Socket.IO. If this message is not received at the client-side after a specified period, the web-application informs the user that the system is offline. A similar approach was implemented when an observation is running. In such an event, the operator can turn-off the data processing pipeline at any point of the observation should the need arise.

This approach of decoupling the front-end components from the PyBiraes backend by introducing a message broker presents several advantages. For instance, the system is scalable to any number of connected clients. This also means that different clients can subscribe to the data exposed through the messaging broker.

This approach makes the front-end independent of the backend's internal implementation. Indeed, the front-end component was built to be easily adapted for other instruments so long as the command interface is the same. In fact, a modified version of this front-end has been adapted to monitor and control the MEXART radio telescope in Mexico [128].

PyBirales is a real-time space debris system, and hence, it is paramount for the operator to be presented with all the system information in real-time. In the monitoring page of the PyBirales front-end, shown in Figure 3.23, the operator is presented with the detections as they are detected in the processing backend. As one can note, the operator is presented with an overview of the detections that were made in the specified time range. The operator is also able to monitor the Root Mean Squared (RMS) voltages of the BEST-2 arrays when an observation is running. This feature is intended to give a quick overview of the status of each antenna in the array. The operator can decide to disable any antenna should a problem be detected.

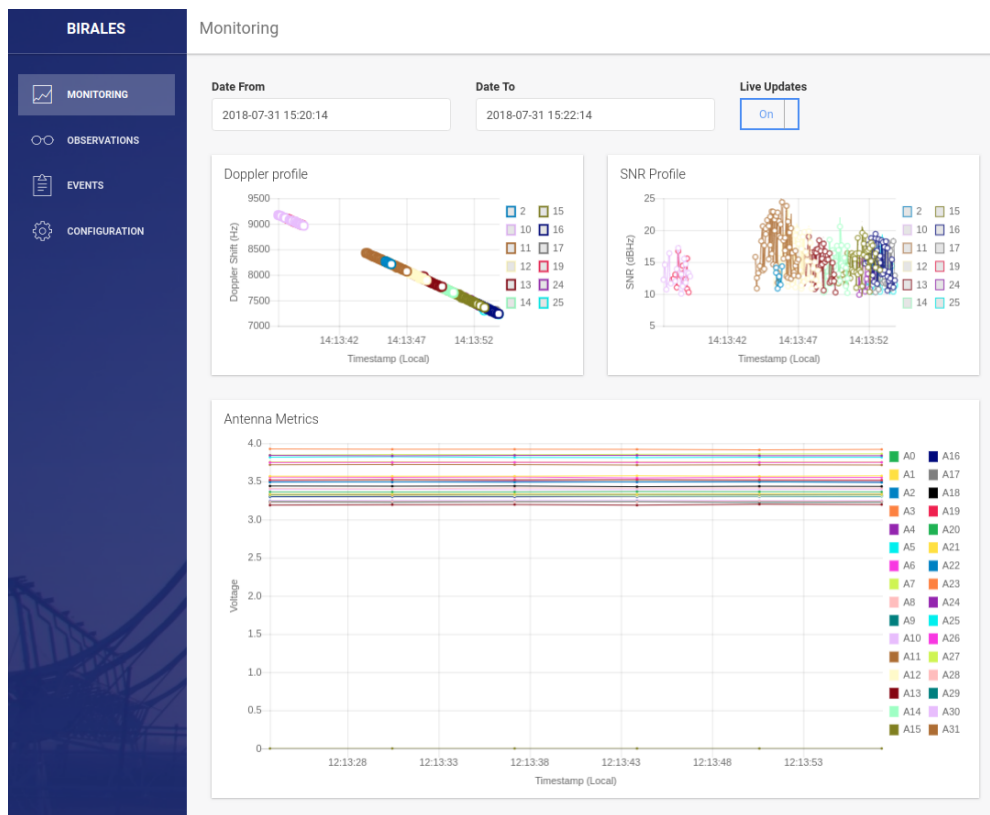
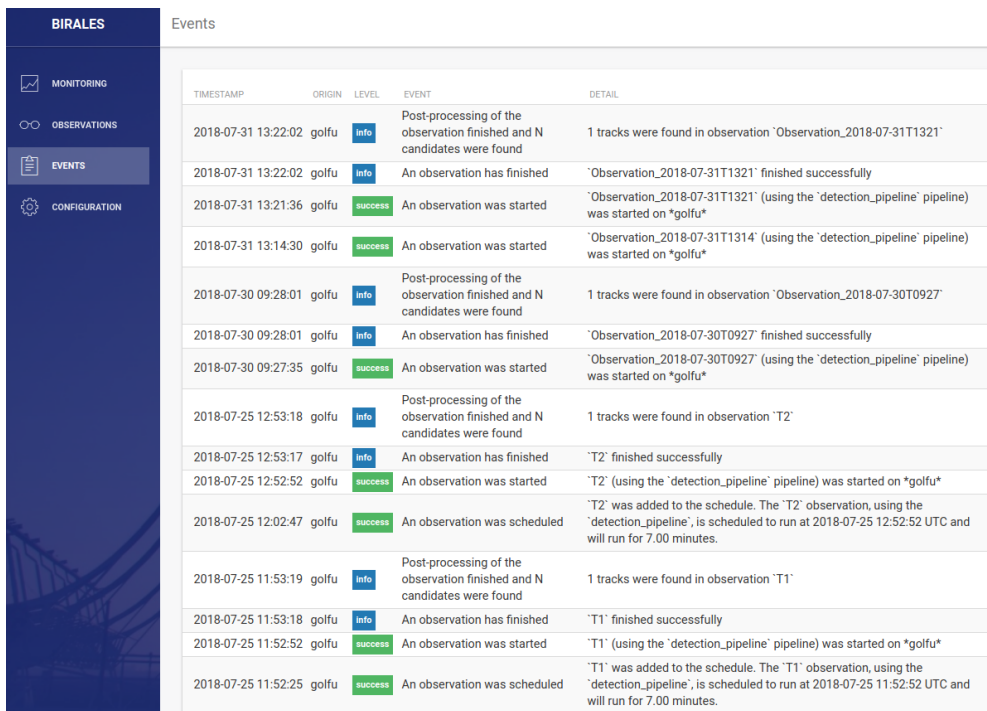


Figure 3.23: The monitoring dashboard of the BIRALES control application

A complete overview of the state of the system can be obtained through the dedicated events page. In the events page, the operator has access to a log of events in a dedicated events page. These events were described earlier in Section 3.4. This log gives the user a detailed history of the status of the system. A typical event log is illustrated in Figure 3.24.



TIMESTAMP	ORIGIN	LEVEL	EVENT	DETAIL
2018-07-31 13:22:02	golfu	info	Post-processing of the observation finished and N candidates were found	1 tracks were found in observation 'Observation_2018-07-31T1321'
2018-07-31 13:22:02	golfu	info	An observation has finished	'Observation_2018-07-31T1321' finished successfully
2018-07-31 13:21:36	golfu	success	An observation was started	'Observation_2018-07-31T1321' (using the 'detection_pipeline' pipeline) was started on *golfu*
2018-07-31 13:14:30	golfu	success	An observation was started	'Observation_2018-07-31T1314' (using the 'detection_pipeline' pipeline) was started on *golfu*
2018-07-30 09:28:01	golfu	info	Post-processing of the observation finished and N candidates were found	1 tracks were found in observation 'Observation_2018-07-30T0927'
2018-07-30 09:28:01	golfu	info	An observation has finished	'Observation_2018-07-30T0927' finished successfully
2018-07-30 09:27:35	golfu	success	An observation was started	'Observation_2018-07-30T0927' (using the 'detection_pipeline' pipeline) was started on *golfu*
2018-07-25 12:53:18	golfu	info	Post-processing of the observation finished and N candidates were found	1 tracks were found in observation 'T2'
2018-07-25 12:53:17	golfu	info	An observation has finished	'T2' finished successfully
2018-07-25 12:52:52	golfu	success	An observation was started	'T2' (using the 'detection_pipeline' pipeline) was started on *golfu*
2018-07-25 12:02:47	golfu	success	An observation was scheduled	'T2' was added to the schedule. The 'T2' observation, using the 'detection_pipeline', is scheduled to run at 2018-07-25 12:52:52 UTC and will run for 7.00 minutes.
2018-07-25 11:53:19	golfu	info	Post-processing of the observation finished and N candidates were found	1 tracks were found in observation 'T1'
2018-07-25 11:53:18	golfu	info	An observation has finished	'T1' finished successfully
2018-07-25 11:52:52	golfu	success	An observation was started	'T1' (using the 'detection_pipeline' pipeline) was started on *golfu*
2018-07-25 11:52:25	golfu	success	An observation was scheduled	'T1' was added to the schedule. The 'T1' observation, using the 'detection_pipeline', is scheduled to run at 2018-07-25 11:52:52 UTC and will run for 7.00 minutes.

Figure 3.24: The event-log page of the BIRALES control application

The operator can administer and schedule new observations using the dedicated observation page. The page gives a quick overview of the pending, past or currently running observations. When a new observation is submitted by the user, the web-server submits the observation through the pub-sub system. The backend, subscribed to the appropriate channel, validates the observation details. If the observation details are correct, an observation is created and saved to the database. The observation is run by the PyBiraless scheduler service once the time of the observation is up. In the case of monitoring observations, the detection results are shown to the user as illustrated in Figure 3.25.

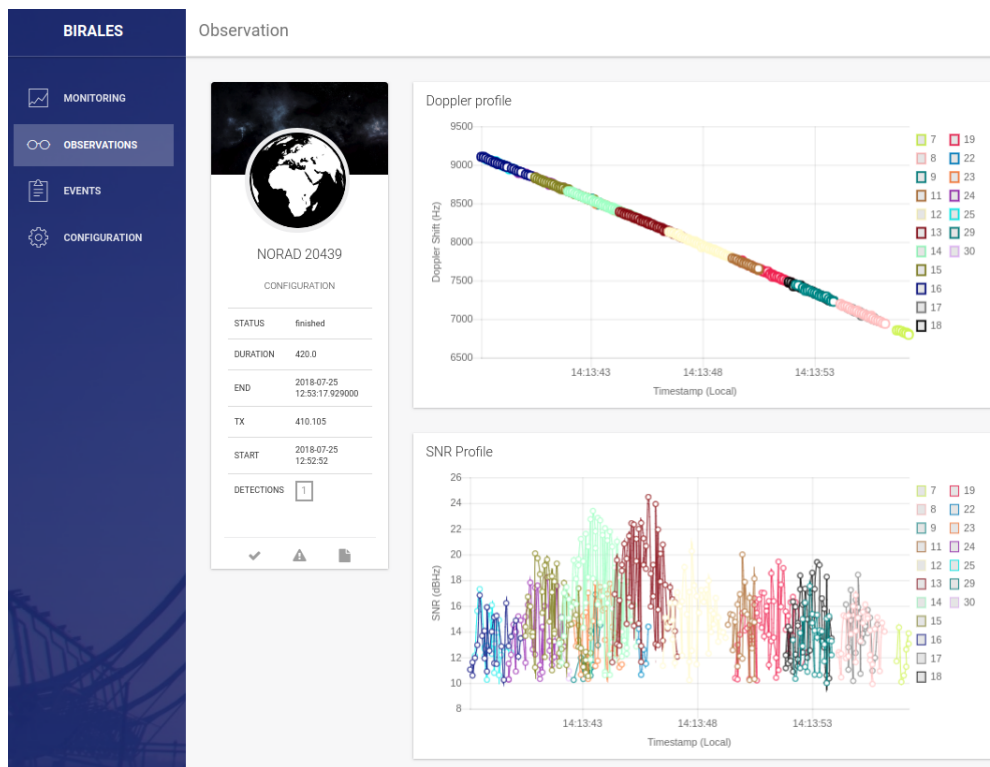


Figure 3.25: The results page for a typical observation of the BIRALES control application

3.11 Conclusion

This chapter presented the components making up the BIRALES bi-static radar. The range and doppler information of the target objects is obtained through two separate systems. It was shown that the BIRALES radar has the capability of detecting small ($RCS \geq 0.1 \text{ m}^2$) targets in LEO.

The data processing system, called PyBiraless, processes the incoming data from the BEST-2 digital backend in real-time. The pipeline framework, which was explicitly designed for this digital backend, was discussed in Section 3.7. Using this framework, different pipelines can be created with ease by chaining different processing modules. These modules modify the incoming data before forwarding it to the next module in the chain. The pipelines in PyBiraless are linear, and hence two processing modules cannot be chained to the same processing module or node. Thus, the pipeline framework can be upgraded such that a processing module could fork its output to two modules which would enable a pipeline to modify the same data differently in two different modules.

Work has started on upgrading the PyBirales system to cater for more antennas. The upgrade is planned to scale to 128 antennas, thereby increasing the sensitivity of the instrument. Performance issues were identified when the data rate is quadrupled. In this case, the PyBirales processing modules may need to be optimised to account for the increased data rate.

The planned upgrades are part of the ongoing effort of enhancing the capability of one of the latest space surveillance systems in Europe. This work presented a complete software system from the processing of phased array signals to the visualisation of the detection results. The next chapter describes the detection algorithms that are used in PyBirales to detect orbital objects in LEO.

Chapter 4

Detection of Orbital Debris

Chapter 3 introduced the modules making up the PyBirales detection pipeline. The pipeline uses a chain of modules that generate channelised data blobs, or spectrogram images, in real-time. Subsequent models within the detection pipeline search these spectrogram images for the presence of radar echoes that are indicative of high-velocity objects, such as orbital debris, crossing the radar coverage of BIRALES. This chapter is concerned with the frequency-domain methods of detecting faint echoes in spectrograms. These echoes, or tracks, are characterised by a sharp increase in intensity when compared to the background levels.

A track detection algorithm tries to identify the presence of radar echoes within non-uniform time-variant background noise. This background noise is often unique to the instrument and introduces points of high energy that distort the tracks, causing them to appear disjointed. This effect is particularly noticeable in radar echoes having a weak SNR. Consequently, a critical criterion was the development of a detection algorithm that can identify faint, low SNR radar echoes. The higher the sensitivity of the detection algorithm is, the farther the detection range of the radar becomes.

The track reaction time of the algorithm was also an important prerequisite given that the timely identification of the transients is essential. Track reaction time can be defined as the time taken between the target's entrance in the instrument's FoV and the creation of the track. The shorter this time is, the quicker a detection event can be broadcast to the interested parties. This ties in with the motivation behind a real-time data processing system.

The third criterion was the quality of the track retrieved by the algorithm. In practice, this means that measurements that do not belong to a target echo

are minimised while the number of data points belonging to the targets echo is maximised. It follows that the higher the track quality is, the better the orbit determination prediction.

The complete retrieval of the radar echoes is made more challenging in the presence of multiple tracks within a single chunk of data or spectrogram. Multiple tracks occur when various high-velocity objects transit the FoV simultaneously. Thus, an optimal detection strategy should be able to correctly resolve multiple, sometimes closely spaced, radar echoes as belonging to distinct targets. Similarly, the detection algorithm should be able to correctly associate all the tracks belonging to the same source even if these are disjointed. In the next section, we look into some of the algorithms that have been employed to date. This is followed by the PyBirales detection strategy that is used to detect faint radar echoes emanating from multiple high-velocity objects within spectrogram images.

4.1 Track detection in spectrograms

The problem of track detection within spectrogram data shares several similarities with asteroid-identification algorithms applied to images obtained by optical telescopes. Of particular note is the work done by the ESA-funded StreakDet framework [129]. More recently, Tagawa et al. [130], describe a method of skewing and compressing a sequence of images to improve on the detected SNR of objects to increase their probability of detection. Kim et al. [131] propose an automated streak detection algorithm, called Automated Streak Detection for Astronomical Images (ASTRiDE), for fast-moving objects in astronomical images. The input image is first thresholded to obtain a binary image. Subsequently, streaks generated by artificial satellites or space debris are identified by a contour-finding method called marching squares [132], that draws contour-lines around regions above the threshold value. ASTRiDE evaluated these regions identified by the marching square algorithm against several criteria (inertia ratio, region area and perimeter) that define a typical streak.

While several streak detection algorithms have been proposed in the optical regime, the number of detection algorithms for high-speed objects in spectrogram images has been limited. Consequently, one can source from other research fields, such as, acoustic analysis.

The space debris detection problem can be boiled down to the identification of tracks within spectrograms (also known as LOFARgrams, sonograms or spectral waterfalls). Track detection in spectrogram images, especially in underwater environments, has been an on-going area of research since the invention of the spectrogram in the 1940s by Koenig et al. [133]. Since then, track identification within spectrogram images has been employed in a plethora of applications ranging from the monitoring of a patient's heart rate [134] to the tracking of a vehicles [135, 136] or humans motion [137, 138, 139]. In the acoustics field, sonograms have been used to identify marine mammals through their calls [140, 141] and track torpedoes, submarines or ships via the noise generated by their machinery [142, 143]. The interdisciplinary nature of the problem has attracted contributions from several research fields including statistical modelling [144], image processing [145, 146, 147] and expert systems [148].

In recent years, track detection techniques in spectrograms have been applied to the problem of detecting meteors entering the Earth's atmosphere [149], [150] and [151]. These studies showed that signal processing thresholding techniques can be used to identify the radio echoes emanated from meteor objects. In 2015, Roman et al. presented a meteor detection solution that uses a Artificial Neural Network (ANN) approach to detect meteor radio echoes in spectrogram data. Using a self-organising map and multi-layered perceptron neural networks, the authors report a detection rate of 85% of the included meteor samples obtained from the Belgian Radio Detection System (BRAMS). However, it reports a high false-negative rate [152].

A survey of the current track detection technology employed in spectrogram data is given in [126]. The review focuses on the track detection algorithms used in acoustics and passive sonar systems. These techniques range from maximum likelihood, neural networks, statistical models, relaxation methods and expert systems. The study reports that traditional line detection methods, such as the Hough transform, and the Laplacian detectors [153] degrade in performance when they are applied on spectrograms containing low-SNR signals. Thresholding techniques are limited by the result in a high true positive rate but also detect many false positives.

Lampert et al. [154] draw a distinction between 'unconstrained' and 'constrained' track detection algorithms. Unconstrained methods, such as Bayesian techniques [155, 156] and the 'bar' detector in [154] use the original unprocessed

data and perform an exhaustive search of the feature space. As a consequence, they are computationally expensive. On the other hand, constrained methods such as Principal Component Analysis (PCA) techniques [157] utilise dimension reduction techniques to reduce the complexity of the problem. In the process, some information relating to the feature space is lost. The best performing method is the unconstrained ‘bar’ detector which has an False Positive Rate (FPR) of 0.10 at True Positive Rate (TPR) of 0.70. This, however, comes at a cost. It took 5.5 min for the detector to go through a 398 by 800 px spectrogram [154].

Approaches based on neural networks presented in [158] do not account for multiple or crossing tracks. Statistical models such as dynamic programming [159] and the Virtebi line detection algorithm [160] assume that only one track is in a spectrogram. Hidden Markov Model (HMM) have also been used in the identification of low SNR tracks within spectrograms. However, the research presented [160] were tested on relatively stationary tracks (gradients of 1 Hz over minutes). Lampert [126] concludes that ‘no algorithm combines all the desirable features to fully realise a viable solution’. It was shown that the SNR limit of the presented techniques presented in this survey to be in the region of 2 dB to 4 dB in the frequency domain for tracks which exhibit a low shape variation (quasi-straight tracks).

The pattern to be extracted can vary across applications and largely depends on the nature of the observed phenomenon. In acoustics, the structure of the signal of interest can range from straight tracks to a periodic pattern [154]. Sonar tracks are characterised by long (>100 s) lines within a spectrogram. A typical spectrogram image showing the tracks that are typically found in passive sonar data, is shown in Figure 4.1 [126]. One can conclude that these properties distinguish them from those that are typical of radar echoes emanating from a high-velocity orbital object. As shown in Chapter 2, the latter are characterised by an oblique track having at a quasi-constant gradient resembling a frequency ramp. Moreover, these tracks are very short (<20 s) in nature and require a very high time-resolution that is typically less than one second.

In the absence of a standard dataset, the data on which the algorithms are evaluated is not consistent. Some of the performance results are generated from synthetic data, while others are from data generated by instruments. Furthermore, the system noise is unique to the instrument. These considerations

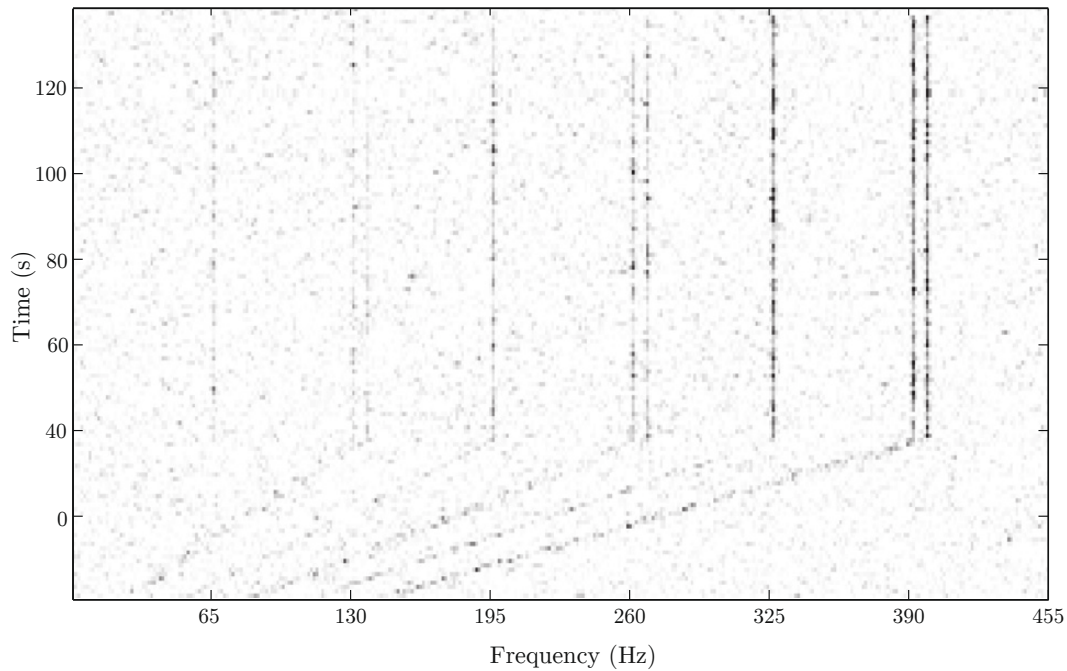


Figure 4.1: A set of 9 tracks that are typically present in passive sonar spectrogram images. First 3 tracks are at 3 dB, 2nd three are at 6 dB and the last 3 tracks are at 9 dB [126]

make it difficult to present a direct comparison between the aforementioned techniques. While the amount of literature in pattern recognition in acoustic analysis has been substantial, the same could not be said for the identification of the high-velocity object in spectrogram data. In light of this, this investigation attempts to bridge this gap by introducing new detection strategies that are tailored for the real-time detection of orbital debris objects in spectrogram images.

4.2 Detection strategy in PyBirales

In the PyBirales detection pipeline, the detection strategy is decomposed of several distinct stages. The first step is the acquisition of the data using the PyBirales pipeline. The raw antenna voltages incoming from the 32-element phased-array are channelised and subsequently beamformed. The detection algorithm sieves through this stream of data for new radar echoes that are unique to high-velocity objects crossing the field of view of the instrument. Upon detection of such a radar echo, or streak, a track is initiated. The

track initiation stage is responsible for the creation of new radar tracks. New measurements are correlated with the existing tracks and updated correctly in a stage called track maintenance. The correlated measurements continue to increase the length of the track until the track termination condition is met. Finally, validated and correct tracks are reported back to the operator and saved in TDM format.

4.3 Pre-processing

The `Pre-Processor` module takes in beamformed, channelized data blobs and calculates the power by taking the square of the received antenna voltages. In a BIRALES observation, the detection pipeline is designed to be started a few seconds before the transmitter starts transmitting. This way, an estimate for the background noise can be determined. This noise estimate is obtained for each channel given that the instrument noise value is not assumed to be uniform across the band. An estimate for the background noise at a channel was taken to be the mean value of the power of the N samples at that channel c . The noise estimate P_ϵ at a given channel was given by,

$$P_\epsilon = \sqrt{\frac{1}{N} \sum_{i=0}^N V_i^2} \quad (4.1)$$

A running average of the noise estimate is computed to minimise the impact of spurious RFI events. The noise estimates are cascaded to the following modules through the header information of the channelized data blob. The pre-processed data is passed on to the `Filtering` module.

4.4 Filtering

The `Filtering` module consists of a number of separate filters that are applied on the data sequentially. This process reduces the number of data points that the detection algorithm has to process thereby simplifying the detection problem at a later stage. The first filter removes the RFI noise that may be introduced by the transmitter when this is in close proximity to the BEST-2 instrument.

4.4.1 Transmitter filter

The RFI signature introduced by the transmitter can be distinguished by two unique characteristics. First, due to the relative proximity of the transmitter, the measured power is very high, usually orders of magnitude higher than that corresponding to a radar echo. Secondly, the transmitter frequency does not change in time and is present within the same frequency channels across time. These two features are exploited in the transmitter line filter.

The channels at which a high power is measured are identified by performing a simple peak search on the data. Each channel is integrated over N time samples and evaluated against a predefined threshold τ . Channels whose summed power is greater than this threshold are considered to be peaks. At these channels, the power P_c across all time samples was replaced by the mean noise P_ϵ as described by Equation 4.2.

$$f_{tx}(P_c) = \begin{cases} P_\epsilon, & \text{if } \sum_{n=0}^N P_\epsilon \geq \tau \\ P_c, & \text{otherwise} \end{cases} \quad (4.2)$$

4.4.2 Background noise filtering

This study investigates the use of image processing techniques for the removal of background noise within a spectrogram image. In image processing, image segmentation refers to the process of attributing different labels to different regions of the image. It is a pre-processing step that often precedes feature extraction algorithms that infer patterns from the data. The goal of segmentation is to simplify the data or change its representation in a way that is easier to process and analyse by other algorithms. Typically, segmentation techniques are used to identify regions which have edges, boundaries or curves.

In our case, we use image segmentation techniques to differentiate regions on the image which belong to a radar echo from noise or any other interfering signal. It is a very effective tool in removing the background noise from the target signal. In this study, a number of algorithms were tested given the limited literature available showcasing the application of these techniques on radar data. In simple thresholding, pixels that are lower than a threshold value are labelled as noise. The advantage of this method is its simplicity and computational efficiency. However, determining an optimal threshold is

difficult. This is especially true when data is received in chunks and the noise value changes across the band.

In sigma-clipping, a data point is marked as noise if its power value P is n standard deviations σ away from the mean noise power P_ϵ calculated in Equation 4.1. Such a filter is defined formally as,

$$f(P) = \begin{cases} P, & \text{if } P \geq 3\sigma + P_\epsilon \\ 0, & \text{otherwise} \end{cases} \quad (4.3)$$

Filters that apply a different thresholding value across an image are called adaptive thresholding techniques. Other techniques, such as the Otsu's method, can determine the optimal threshold automatically from the power spectrum of the image. This method assumes that the power spectrum of an image is bimodal. Such an image is characterised by two peaks, one for the source signal and another for the background noise. In such an image, the optimal threshold is found to be in the middle of these two peaks. Otsu's method tries to determine the optimal location of this point [161]. The problem with this method is that if the histogram does not contain two peaks, such as in the presence of RFI or multiple tracks, the results would not be accurate. Other classical thresholding methods that were used were the minimisation [162, 163] and yen [164, 165] and triangle thresholding [166]. In the latter, a line joining the maximum of the histogram and its lowest value is constructed. The distance d between this line and the histogram values are calculated for each bin. The global threshold is identified as the bin at which the maximum distance is obtained. The algorithm is effective in images whose object of interest results in weak peaks in the histogram [167]. This property makes it attractive for our application given that radar echo streaks usually result in weak peaks within the power spectrum.

4.4.3 Salt-and-pepper noise filter

The background filters described earlier are very effective in removing the majority of the background noise within a spectrogram. However, the image is still characterised by isolated noise pixels or salt-and-pepper noise. These data points can be considered to be isolated pixels with no neighbouring pixels. These pixels can be removed by applying a binary hit-or-miss transform to

find the location of these pixels. It uses an iterative process where a kernel, or mask, is moved through-out the target image. Thus, if the kernel is applied to a subset of the image S , the pixel p at the center of S is deemed to be a ‘hit’ if S matches the kernel’s pattern. Otherwise, the pixel p is considered to be a ‘miss’. In this case, the transform finds the pixels with no immediate neighbouring pixels as specified by the kernel represented in Figure 4.2. Once these pixels are identified, the power value at these locations is set to zero.

0	0	0
0	1	0
0	0	0

Figure 4.2: A graphical representation of the binary mask (kernel) used for the filtering of speck noise

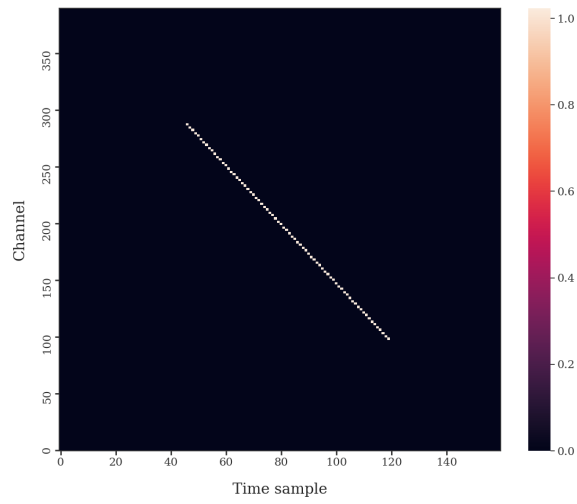
The effectiveness of this filter however comes at a computational cost given that the computational complexity of the filter is $\mathcal{O}(N_c N_t N_k)$ where, N_c is the number of channels, N_t is the number of samples and N_k is the size of the kernel.

4.4.4 Evaluation

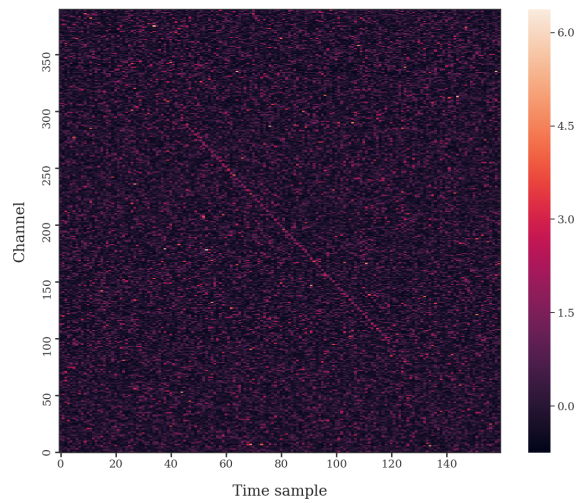
The aforementioned filters are tested on synthetic raw images that reproduce the background noise environment that is typical of the BEST-2 array. Linear streaks are introduced in the dataset at different SNR levels and inclinations in order to simulate the radar echoes that are typical of RSO objects. In this work the SNR is defined as,

$$\text{SNR}_{\text{dB}} = 10 \log_{10} \left(\frac{P_s - P_\epsilon}{P_\epsilon} \right) \quad (4.4)$$

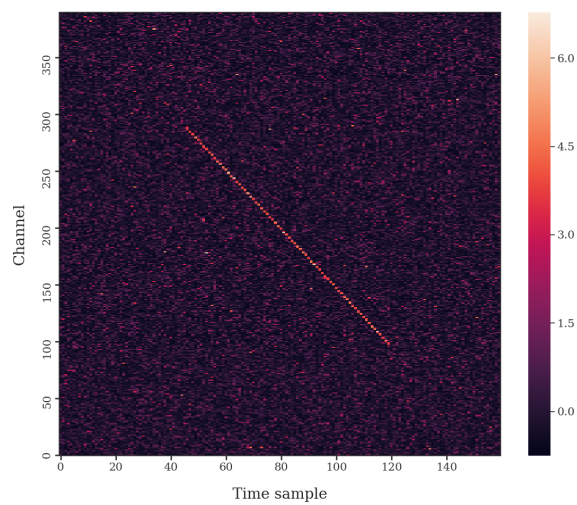
where P_s is the power from the instrument and P_ϵ is the estimated power of the background noise that was obtained by the **Pre-Processor** module. Figure 4.3 illustrates a typical ground truth image (Figure 4.3a) together with the corresponding synthetic test images (in different SNR) on which the filtering algorithms are applied (Figure 4.3b and Figure 4.3c). One can observe that at lower SNR levels, the tracks are barely visible to the eye, thereby highlighting the non-triviality of this problem being solved.



(a) Ground truth track represented as a binary image



(b) SNR = 1 dB



(c) SNR = 5 dB

Figure 4.3: A typical test track at various SNR levels and the corresponding ground truth track. One may note that at an SNR of 1 dB, the radar echo is barely visible to the naked eye

The typical output of the Triangle image segmentation algorithm is shown in Figure 4.4a. The output of this filter is passed through the hit and miss transform and the results is illustrated in Figure 4.4b. One may note that the majority of the noise pixels are removed using this filter. In this case, the Triangle thresholding method, followed by a hit-and-miss transform removed up to 95% of the data points thereby drastically reducing the complexity of subsequent stages in the detection process.

The performance of the filters is evaluated by comparing the ground truth data with the binary output of the filters. A True Positive (TP) is a data point that is present in the ground truth data. This data point is a frequency, time pair that represents a single data point of a radar echo streak. Conversely, a True Negative (TN), is a data point that has been correctly identified as noise.

It was essential to choose an algorithm that struck a balance between retrieving as much possible of the target echo while maximising the removal of noisy data and RFI. Sensitivity, commonly referred to recall, is a metric that measures the ability of a classifier to retrieve all the data points that are present in the ground truth image. This is defined as:

$$\text{Recall} = \frac{\text{TP}}{\text{TP} + \text{FN}} \quad (4.5)$$

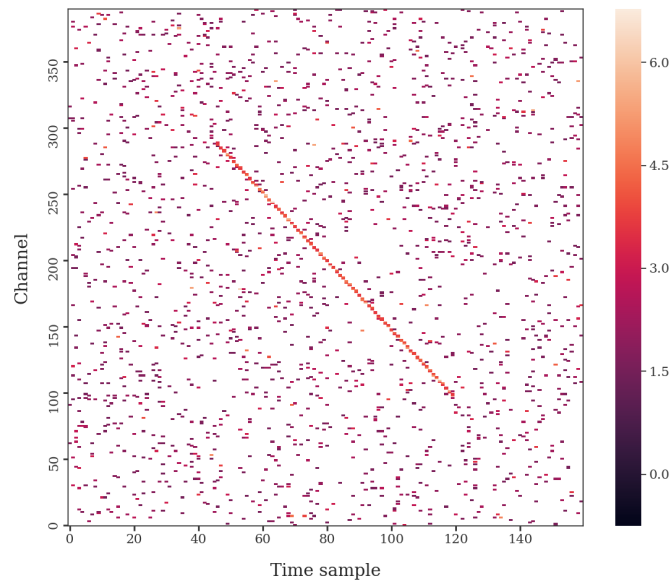
Furthermore, we are after an algorithm that can reduce the complexity of the subsequent detection algorithm by removing true negatives as much as possible. Specificity, or true negative rate, measures the proportional number of data points that were correctly classified as true negatives. Formally, it is given by,

$$\text{Specificity} = \frac{\text{TN}}{\text{TN} + \text{FP}} \quad (4.6)$$

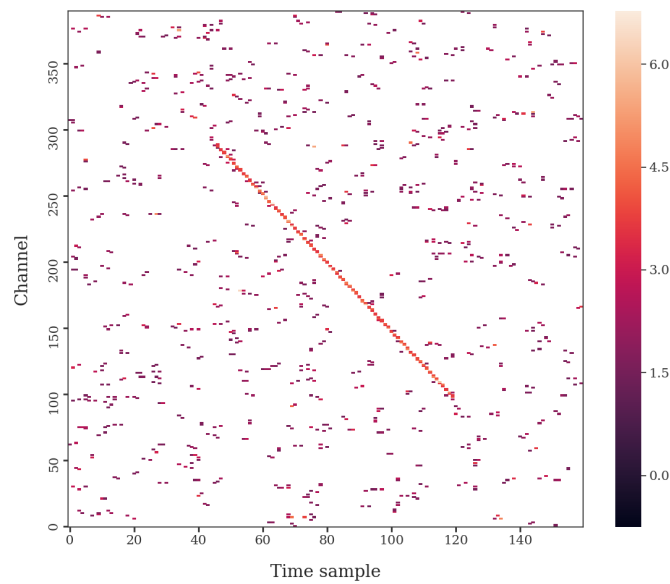
The combination of both metrics was used to identify the best image segmentation algorithm to use for this data reduction step. Thus, the harmonic mean of the two was used to identify the optimal algorithm for the application.

$$\text{Score} = 2 \cdot \frac{\text{Recall} \cdot \text{Specificity}}{\text{Recall} + \text{Specificity}} \quad (4.7)$$

The filtering algorithms were applied on the same test image containing several tracks of different lengths and inclinations, at different SNR levels. The results of these tests are shown in Figure 4.5. It is clear that both specificity



(a) Visualisation of the output of the Triangle image segmentation algorithm applied on a spectrogram containing a track at 5 dB



(b) A spectrogram of the data after the salt and pepper noise filter is applied

Figure 4.4: A typical test track at 5 dB being filtered by the Triangle filter followed by the salt-and-pepper filter

and recall of the algorithm increases as a function of the SNR. At an SNR higher than 5 dB, most of the filtering algorithms reach recall and specificity of unity. This suggests that if the signal strength is strong enough, all the

filtering algorithms tested are adequate for filtering the target signal from the background noise.

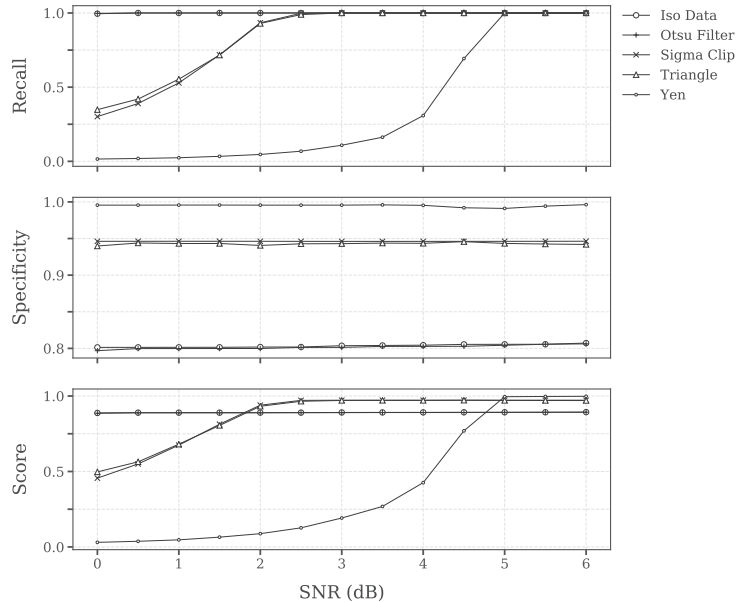


Figure 4.5: Comparison of the performance obtained from different image segmentation algorithms applied on different spectrogram images containing tracks at different levels of SNR. These results, including standard deviations, are presented in Table A.1 in Appendix A.2

As the target signal gets weaker, there is a sharp drop in the recall levels of the minimum and yen algorithms. On the other hand, the rest of the algorithms maintain a 90% recall score down to SNR of 2 dB. Below this threshold, the Otsu and Iso Data filter obtain a better performance. However, this comes at the expense of a low true negative rate when compared to the Sigma Clipping and Triangle thresholding methods. In view of all this, the results indicate that the triangle and sigma clipping methods achieve the best results overall. The triangle method appears to be more sensitive at lower levels of SNR, while the sigma clipping method has a slightly better specificity score.

The time taken for the processing of a (4100 by 160) pixel image is shown in Figure 4.6. The results show that sigma clip filter is the most computationally expensive. It can also be noted that the hit-and-miss transform takes a considerable chunk of the filtering stage. This suggests that a more optimised solution needs to be found. However, all the approaches are well below the real-time criteria. Passing the spectrogram through the image segmentation filters reduces the number of possible measurements. The aforementioned fil-

tering techniques, such as Triangle and sigma clipping thresholding have been shown to be effective in greatly reducing the computational complexity of the next stage of the detection process; track initiation.

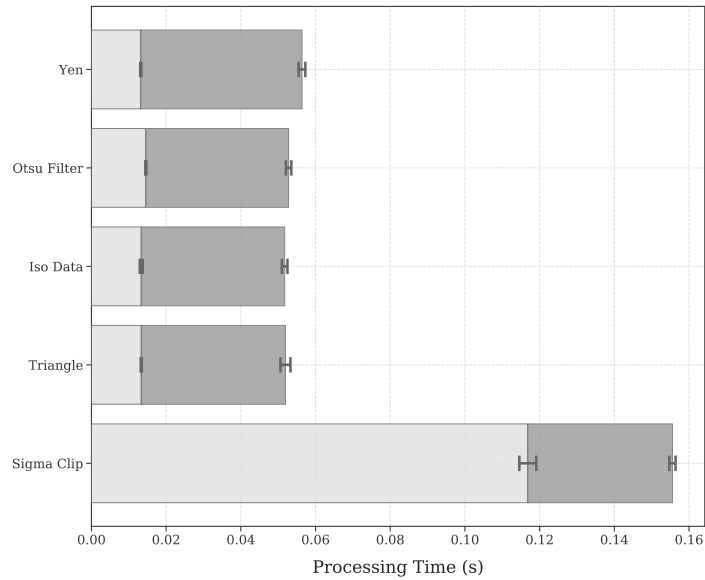


Figure 4.6: Performance benchmark of the image segmentation algorithms tested in this study. The computational time taken by the salt-and-pepper filter is shown in grey

4.5 Track initiation

The pre-processed and filtered data is passed on to the detection module in which the track detection algorithms are implemented. The image segmentation process results in a set of unconnected points, or pixels. These algorithms exploit only the intensity information at each pixel and thus do not take into account their relationship with other neighbouring pixels.

A track detection algorithm tries to identify a series of these points, known as tracklets, that are likely to form part of a radar track. Tracklets can be considered as low-quality tracks that may be part of a radar track. Target initiation refers to the process of establishing track candidates from these tracklets.

In this study, a number of different feature extraction algorithms were investigated. Classical edge detection algorithms such as Hough transforms were initially investigated. The Hough transform solves the edge detection problem

by converting the problem to a local peak detection search in parameter space [168]. In earlier work [50], this method proved to be effective in the identification of RSO. However, the algorithm proved to be less effective in the presence of noise and targets with a low SNR.

As a result, clustering techniques were investigated instead. Clustering is the unsupervised organisation of unlabelled data into groups called clusters. Patterns within one cluster are considered to be more similar to each other than to any other pattern associated with a different cluster [169]. The number of clusters, or tracks, present in a single image is not known a priori. Additionally, the clustering algorithm should be able to account for any residual noise artefacts which were not caught at the filtering stage. This meant that popular clustering techniques such as k-Nearest Neighbors (k-NN) or spectral clustering were not investigated given that they do not cater well for noisy data [170] and the number of clusters present needs to be specified as an input to the algorithm [171]. Consequently, this study presents two new track detection strategies that are tailored for the identification of tracks in spectrogram data. The first approach uses the Density-Based Spatial Clustering of Applications with Noise (DBSCAN) [172] clustering algorithm.

4.5.1 DBSCAN clustering

As a hierarchical clustering technique, the DBSCAN clustering algorithm does not make any assumption on the number of clusters within an image [173]. This property makes it possible to detect and distinguish between multiple tracks within a single spectrogram. An added advantage of this clustering algorithm is that it is able to classify isolated pixels as noise thereby distinguishing them from valid clusters.

DBSCAN starts by retrieving all the points that are *density-reachable* from an arbitrary point p . A point p is *density-reachable* from a point q if there is a chain of points $p_1, \dots, p_n, p_1 = q, p_n = p$ such that p_{i+1} is *directly density-reachable* from p_i . A point p is said to be *directly density-reachable* from a point q if $p \in N_{Eps}(q)$ and $|N_{Eps}(q)| \geq \text{MinPts}$ where MinPts is the minimum number of points in a cluster. The *Eps-neighbourhood* of a point q is defined by

$$N_{Eps}(q) = \{p \in D \mid \text{dist}(q, p) \leq Eps\} \quad (4.8)$$

where D is the set of data points on which the algorithm is applied, $dist(q, p)$ is a distance function and Eps is a constant that defines the maximum distance between p and q to be considered to belong to the same cluster. In this work, both the Eps and the $MinPts$ parameters were set to be 5. These values were obtained empirically.

The point p can either be treated as a *core* point or a *border* point. A *core* point is defined as a point within a cluster whilst a *border* point is one that is at the edge of a cluster. In both cases, a cluster C is considered to be a non-empty subset of D if the following conditions are satisfied.

- $\forall p, q$: if $p \in C$ and q is *density-reachable* from p *w.r.t.* Eps and $MinPts$, then $q \in C$. (Maximality)
- $\forall p, q$: if $p \in C$ and q is *density-connected* to q *w.r.t.* Eps and $MinPts$. (Connectivity)

A point p is considered to be *density-connected* to a point q if there is a point o such that both p and q are *density-reachable* from o . This relationship is both transitive and symmetric. Points which do not satisfy these conditions are regarded as noise such that if C_1, \dots, C_k are clusters of D , then $noise = p \in D | \forall i : p \notin C_i$.

Once the point p is classified as either a *core*, *border* or noise, the algorithm moves to the next point in D . Thus, this approach groups points that are closely packed together, expands clusters in any direction where there are nearby points using a density-based metric. This way, it is able to deal with different shapes of clusters making it ideal for the detection of radar echoes.

Figure 4.7 shows the groups identified by the DBSCAN for a typical dataset. One may observe that the algorithm is very effective in grouping most of the pixels related to the target detection. However, one may also observe the presence of clusters which are clearly false positives.

False positives are dropped through a validation process that consists of a set of rules on the track quality. For instance, clusters made up of a few data points are ignored. Furthermore, the shape of the cluster is also taken into account. Tracklets are expected to be linear where the frequency and time of a detection are strongly correlated.

The algorithm searches for clusters with a high degree of correlation between frequency and time. A cluster is deemed to be a linear cluster if it has

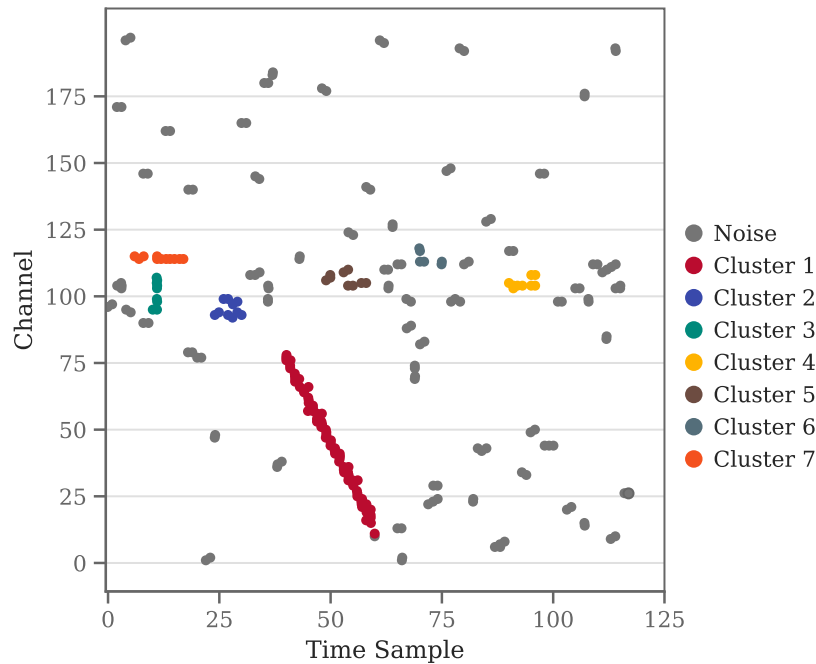


Figure 4.7: The detection clusters identified by the DBSCAN algorithm including the data points that were classified as noise

an r^2 value greater than 0.99. In order to do so, the Random sample consensus (RANSAC) regression was used.

The RANSAC algorithm, gives a lesser weight to outlier, data points which effectively means that these data points are ignored. In so doing, the track quality is improved. Another optimisation that was introduced was to ignore clusters with an unrealistic doppler shift value. Analysis of the typical doppler shift and altitude of catalogued objects put the expected doppler shift Δf to lie between,

$$-12\,143\text{ Hz} \geq \Delta f \geq 13\,245\text{ Hz} \quad (4.9)$$

Clusters with a doppler shift value outside of this range were dropped. Similarly, a range for the detection gradient can be obtained. The rate of change in the measured doppler is expected to lie between

$$-291.47\text{ Hz s}^{-1} \geq \frac{\Delta f}{\Delta t} \geq -69.62\text{ Hz s}^{-1} \quad (4.10)$$

These optimisations ensure that only valid RSO tracklets are passed on to the next stage. This detection strategy has been used to date in the detection module of the BIRALES radar. While the results have been encouraging, observations have highlighted several possible avenues for improvement. For instance, tests have shown that the algorithm becomes less effective in detecting low-SNR targets. These limitations were the motivation behind a new approach for the detection of orbital debris. This approach is discussed in the next section.

4.5.2 A multi-beam streak detection algorithm

This work presents a new detection algorithm, called Multi-beam streak detection strategy (MSDS), that uses a clustering approach to identify streaks in spectrogram images. The aim is to propose a clustering approach that attempts to solve the aforementioned limitations of other techniques. In particular, we sought to develop an algorithm that is sensitive to low-SNR tracks that exploits the unique characteristics of the BIRALES radar. In this section, the input data is assumed to be pre-processed by an image segmentation algorithm such as the Triangle method. A representative example of the input data for a single spectrogram is shown in Figure 4.8.

A kd-tree binary tree is used to subdivide the spectrogram into rectangular boxes to guide the decomposition of the space. The point at which the split occurs depends on the ‘sliding midpoint’ rule where the domain is split along its the longest axis [174]. In the case where a split results in no data points in one side of the rectangle, the mid-point is moved to the closest data point. Each rectangle is further split along an axis (vertical or horizontal) in a recursive fashion until the number of points within the rectangle reaches a predefined bucket or maximum leaf size l_{\max} [175]. The construction of the d -dimension tree for a spectrogram with n data points is done in $\mathcal{O}(dn \log_2 n)$ time [176].

The algorithm uses a bottom-up approach that tries to identify small linear streaks in each of the kd-tree’s leaves. These calculations on each leaf are identical, the only difference being the data they operate on. This problem is said to be ‘embarrassingly parallel’ since the operations can be executed in any order. Thus, they can be trivially parallelisable since there is no need to synchronise the different threads as there is no need to share data amongst them [177]. This makes it possible to achieve a high computing throughput.

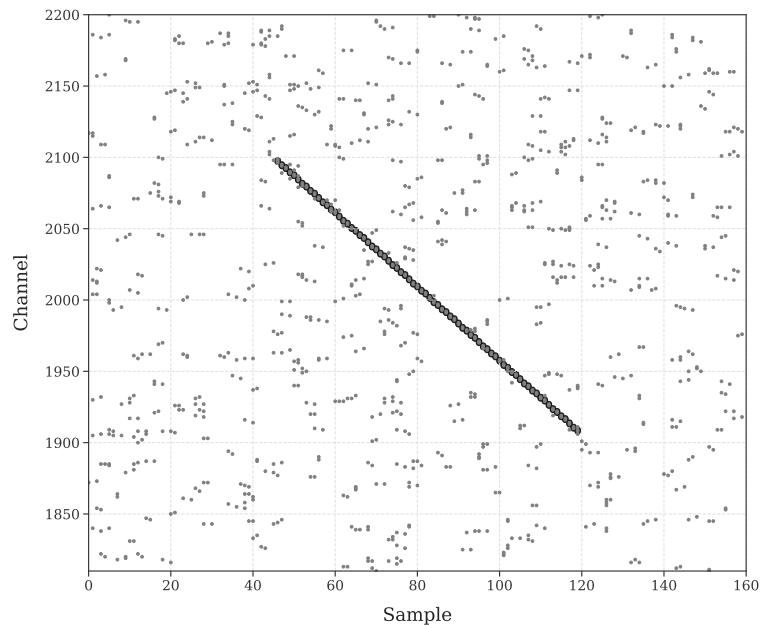


Figure 4.8: Visualisation of the input data to the feature detection algorithm (MSDS)

In order to decrease the computational costs in high-SNR environments, each leaf is passed through a sigma clipping function. This function compares the intensity value of each data points against the mean within the leaf. Data points that are 5 dB below the mean intensity within the leaf are dropped. This filter makes it possible to further remove false positives in a computationally efficient manner.

An unsupervised hierarchical clustering algorithm processes the kd-tree leaves in search for group of points that together form a linear track. Agglomerative hierarchical clustering is a bottom-up approach where each data point is initially treated as a potential cluster. Subsequently, the most similar pair of clusters are merged recursively until a single cluster remains [173]. The similarity of two clusters \mathbf{p} and \mathbf{q} , is determined by the distance function $d(\mathbf{p}, \mathbf{q})$ given by,

$$d(\mathbf{p}, \mathbf{q}) = \begin{cases} \sqrt{\sum_{i=1}^2 (q_i - p_i)^2}, & \text{if } S_{\min} \leq m(\mathbf{p}, \mathbf{q}) \leq S_{\max} \\ \text{inf}, & \text{otherwise} \end{cases} \quad (4.11)$$

The spacing between two points p and q is given by their Euclidean distance if the slope m of the line joining the two points $m(\mathbf{p}, \mathbf{q})$ is within a range $[S_{\min}, S_{\max}]$ (Equation 4.10). This range was obtained through simulation and represents the expected rate of change in doppler shift of the targets. Conversely, if the gradient is not within this range, the two points are assumed to be infinitely far away.

The pairwise distance is computed for all points $\mathbf{p}_1, \dots, \mathbf{p}_n$ in a set D such that a distance matrix D_m is obtained. Once the distance matrix is obtained, the data points are organised into clusters using single linkage clustering or nearest neighbour criteria. The algorithm has a time and memory complexity of $\mathcal{O}(n^2)$ [178].

In single-linkage clustering, the similarity of two clusters X and Y is determined by the closest pair of members x, y where $x \in X$ and $y \in Y$ [179] such that,

$$D(X, Y) = \min_{x \in X, y \in Y} d(x, y) \quad (4.12)$$

where $d(x, y)$ is the distance between two points x and y . The clustering algorithm groups data points in pairs by this distance function. Similarly, the resulting groups are in-turn merged recursively until all data points are merged into one group. This group can be represented as a hierarchical tree (dendrogram) showing the distance at which the individual groups were combined. Groups separated by a distance greater than a maximum inter-cluster distance t are treated as distinct clusters. This way, a set of clusters is obtained for each leaf node.

The shape of a cluster can be represented by the two principal axes P_1 and P_2 corresponding to the eigenvectors of the covariance matrix. An example of this is illustrated in Figure 4.9. The ratio of the corresponding eigenvalues, referred to inertia ratio I_r , gives a description of the degree of elongation of the cluster's shape. In this formulation, an inertia ratio of 1 indicates a circle while a perfect line has an value of 0 [180]. Calculating the inertia ratio I_r for each of the identified clusters makes it possible to filter out non-linear tracks. The I_r threshold is set to 0.15. This cluster filtering process yields to the results shown in Figure 4.10.

One may note that a set of small linear clusters, called tracklets (in green), within the spectrograms. One may also note that the algorithm is robust to

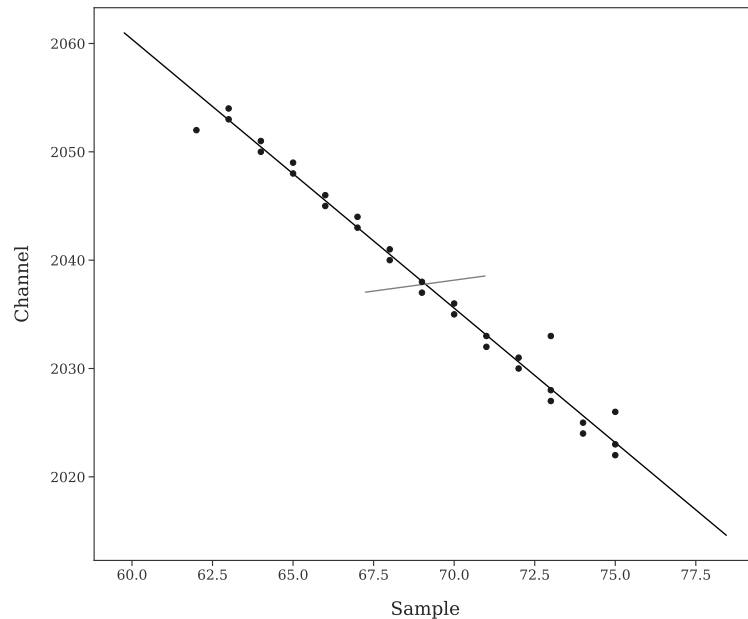


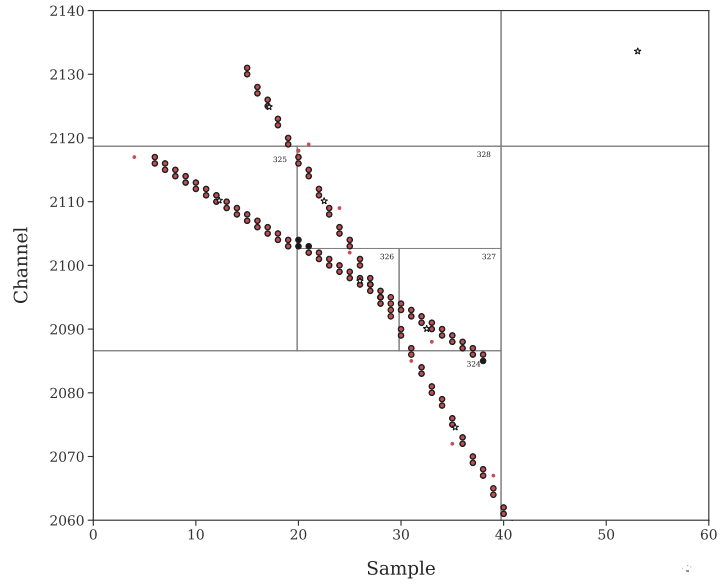
Figure 4.9: Visualisation of a linear streak with an inertia ratio of -0.002 (MSDS). The two principal axes are shown as solid lines

noise with a low false-association ratio. The next stage is to correctly merge the individual tracklets detected across the leaves into larger tracks. To do so, the same clustering approach, discussed beforehand, is used.

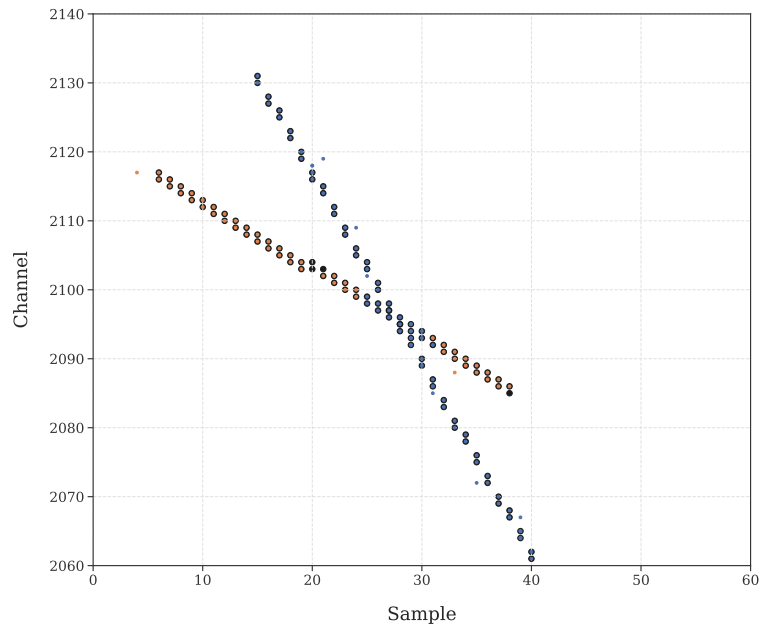
Each cluster is represented by its centroid in order to reduce the computational expense. The inter-cluster distance threshold is calculated automatically from the mean length of a leaf's diagonal. In doing so, the linear clusters within adjacent leaves are merged together to form the full track. The resultant output of this step is visualized in Figure 4.11.

Figure 4.11 shows that the resulting tracklets have been correctly merged together to form a single track. Similar to the DBSCAN approach, RANSAC [181] is used to identify data points that are outliers. Data points that were identified to be outliers are also tested for linearity. A separate track is created in the case when a linear model can be fitted on the outlier data points. This method is particularly useful for distinguishing between crossing streaks.

Crossing streaks occur when two objects, having a similar doppler shift, cross the field of view of the instrument at the same time. Figure 4.12 illustrates how two separate linear tracks, that were labelled to belong to the same cluster (Figure 4.12a) are correctly separated using the aforementioned step (Figure 4.12b). The reliability of this approach can be limited for short tracks



(a) Crossing streaks detected as a single cluster (MSDS)



(b) Correct track separation of two crossing streaks (MSDS)

Figure 4.12: An example of a crossing track test data

that do not contain a substantial number of data points. In fact, a robust method for the correct delineation of crossing tracks is still an open problem and is the subject of further work.

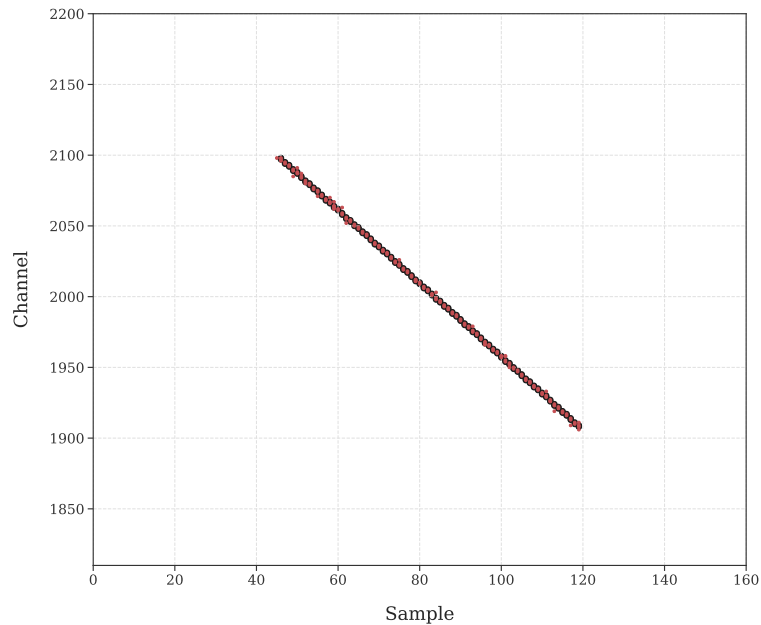


Figure 4.13: The resultant track upon track validation (MSDS)

The level of ‘linearity’ of the resulting inlier set of measurements is determined by a linear least squares regression. The probability of false positives is minimised by dropping tracks with a relatively low r-value (≤ 0.99), a high p-value (≥ 0.05). These thresholds were determined empirically. The effectiveness of this validation process is illustrated in Figure 4.13. One can observe that outliers are correctly removed using this validation process. The following section examines the performance achieved by this algorithm against that obtained by other techniques.

4.5.3 Evaluation

The algorithms developed in this study were first tested on synthetic data before being deployed in observation campaigns. These tests shed light on the performance of the chosen algorithms in a more controlled, and reproducible, environment. Tests were performed on synthetic spectrogram images that emulated the response of the BIRALES radar. In order to simulate the radar’s

response as close as possible, RSO tracks, were injected in spectrogram images. It was made sure that these ‘blank’ spectrograms contained no radar echoes.

A test consists of a spectrogram image containing multiple tracks of different lengths, doppler shift and inclination. The value of each of these parameters was selected at random from a range that is expected from LEO objects. Each detection algorithm was applied on a set of such tests at different SNR levels.

The performance of the two approaches used in this work, DBSCAN and MSDS, were compared against that achieved by a standard Hough transform and the Astride streak detection algorithm. The output of each algorithm is a set of data points (or pixels), which are predicted to belong to an RSO echo. The recall and precision metrics were obtained by performing a pixel-by-pixel comparison between the predicted data points and the ground truth data.

The precision of the detector is defined as,

$$\text{Precision} = \frac{\text{TP}}{\text{TP} + \text{FP}} \quad (4.13)$$

where FP (false positives) is the number of data points that were incorrectly classified as belonging to an RSO echo. The harmonic mean of these two metrics is often used to present a single representative measure of the performance of a detector. This metric is defined as the F1 score, that is defined as,

$$\text{F1} = 2 \cdot \frac{\text{Recall} \cdot \text{Precision}}{\text{Recall} + \text{Precision}} \quad (4.14)$$

The recall, precision and the subsequent F1 score of the detectors implemented in this study are summarised in Figure 4.14. One observes that both DBSCAN and MSDS approach achieve better recall and precision scores than both Astride and the Hough transform. The latter two algorithms do not register a substantial improvement in both recall and precision measures as the SNR level is increased beyond 2 dB.

In the case of the DBSCAN approach, recall improved with increasing levels of SNR. At an SNR level of 2 dB, the recall score is reduced to less than 50%. In contrast, the proposed MSDS algorithm is still able to recall 90% of the track information at an SNR of 2 dB. This represents a substantial improvement in recall rates when compared to the other approaches.

The increased sensitivity of the MSDS algorithm, however, comes at a computational cost. This is illustrated in Figure 4.15. As one can observe, the

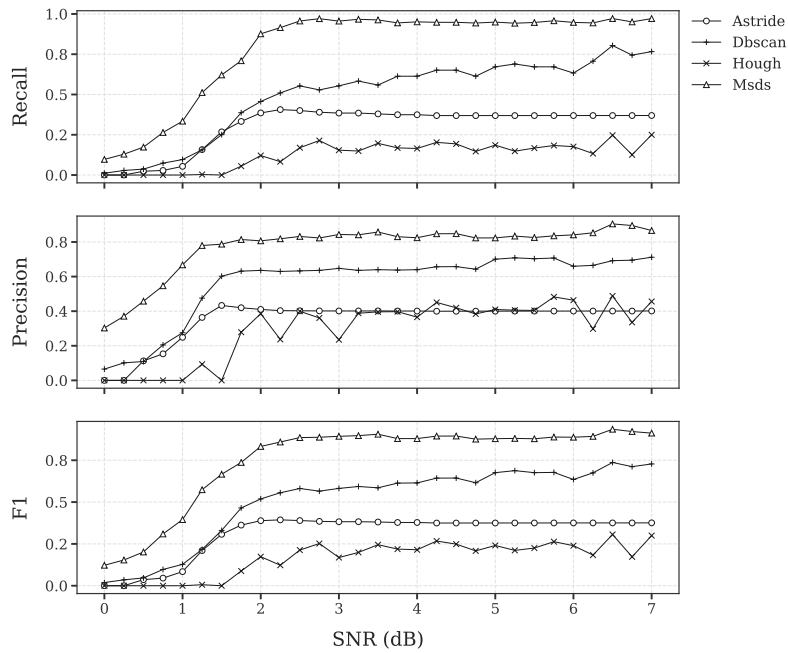


Figure 4.14: Performance metrics of four streak detection algorithms. These results, including standard deviations, are presented in Table A.2 in Appendix A.2

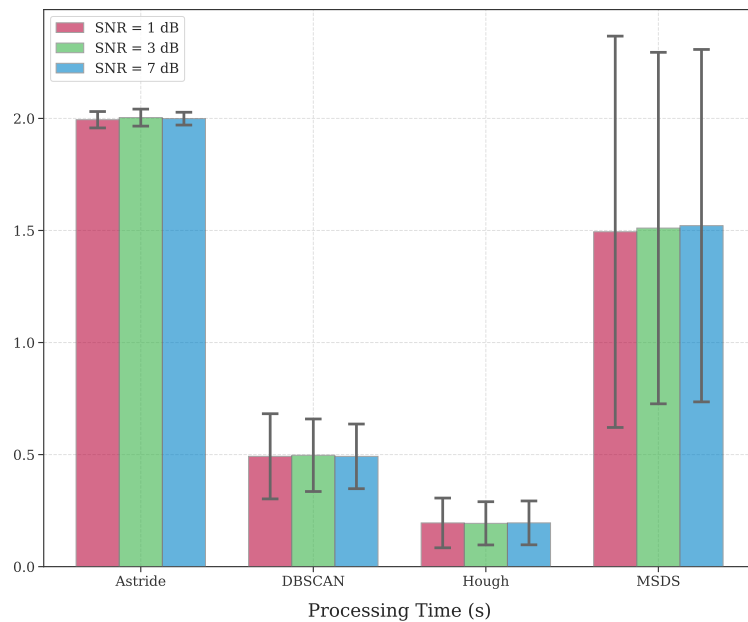


Figure 4.15: Performance benchmark of four streak detection algorithms

MSDS algorithm is computationally expensive when it is compared with the other algorithms. Furthermore, one may also observe the substantial variabil-

ity in the time taken by the MSDS algorithm. This variability is expected given that the processing time is dependant on the number of clusters identified at each stage of the detection process. However, these performance issues can be addresses through a multi-processing. As will be shown in the next chapter, the appropriate implementation of a multi-processing version of the MSDS algorithm is able to process the data in real-time.

4.6 Track association

In the previous sections we saw how the detection algorithms proposed in this work are able to identify multiple tracks present in a spectrogram. A track can span multiple iterations and thus be present across multiple, subsequent, data blobs. As a result, different clusters in subsequent data blobs can belong to the same RSO track. Thus, a system of merging, or linking, these tracklets belonging to the same RSO was put in place. This process is called tracklet linking or track association. Tracks identified in subsequent data blobs should also be associated with any tracks identified in the previous spectrograms or pipeline iterations. Data association of these tracks ensures that a single TDM file is created for a transiting object.

The data association algorithm used in detection module is described in Listing 4.1. New tentative tracks detected in blob i are iteratively compared against the tracks present in this queue (detected in blob $i - 1, i - 2, \dots$). This comparison consists of a similarity score between a candidate track parameters and the validated tracks. The similarity s is calculated as the coefficient of variation between the slopes of the track and the candidate track being compared. This is calculated as,

$$s = \frac{\sigma}{\mu} \quad (4.15)$$

where σ is the standard deviation and μ is the mean of the slopes being compared. If the similarity is below a threshold $\epsilon = 0.1$, the candidate track data is merged, or associated, with the ‘parent’ track. Thus, the track grows as new tracks are detected and associated with it. Tracks which were created or modified during an iteration are persisted to the database.

```
for tracklet in tracklets:
```



```

for track in tracks:
    # If tracklet is similar to track: associate
    if track.is_similar_to(tracklet):
        track.associate(tracklet)

        break
    else:
        # If tracklet does not match any track,
        # create a new track from the tracklet.
        track = SpaceDebrisTrack(tracklet)

        # Add the RSO track to the tracks queue
        tracks.append(track)

```

Listing 4.1: Tracklet linking

On the other hand, when no track exists in the queue, the candidate track is put on the queue as a tentative track. The track is kept in memory in order to compare it with any future detection of new candidate tracks until the quality of the track increases to a point where it becomes a confirmed track. A track is considered to be valid if it is detected across more than 2 beams, has a track length of at least 3 s and a correlation coefficient greater than 0.99. In the case where the quality of a track does not meet the predefined criteria after a number of iterations, the track is cancelled. When a track is cancelled, it is removed from the database. On the other hand, valid tracks are kept in memory until the track termination criteria is met.

4.7 Track termination

At a certain point in a track's lifetime, a decision has to be made as to when the track should be terminated. Failure to do so at the correct time, can be detrimental to the quality of the track. In the case when the track is terminated too quickly, would result in a track with missing data. On the other hand, when the track is not closed, new tracklets belonging to a separate source can be incorrectly associated with the track. In PyBirales, a track is terminated if it is not updated for a specified time span τ . The threshold is based on the

expected maximum transit time of an object in LEO. At present, this was set to 3 s.

This simple track termination method proves to be adequate for this application since the number of track initiation events is low. A more precise approach is to calculate the theoretical time at which the space candidate exists the instrument FoV based on its velocity. However, it is difficult to obtain this estimate without ranging information of the target.

Upon track termination, the track is saved in TDM format and an ‘New Tracked Detected’ event is fired. The event is pushed in real-time to PyBiraes monitoring dashboard described in the previous chapter. An operator is immediately notified of any detection data.

4.8 Conclusion

In this chapter, a review of the existing track detection algorithms in spectrograms was given. The review highlighted the research gap in the detection of radar echo in spectrogram data. Consequently, this work proposed two detection algorithms for the detection of orbital objects in spectrogram data. The algorithms make use of image segmentation techniques to remove the background and RFI noise artefacts in the received data. Filtering techniques reduce the number of pixels, or data points, which are processed in the detection algorithm.

Experimental results on synthetic data showed that the Triangle image segmentation algorithm is particularly effective in segmenting low-SNR signals. However, a feature detection step is required to identify the valid tracks from the background noise. Apart from the intensity value of the pixels, a feature detection algorithm takes into consideration the structure of the track and the relationship of the pixels with other neighbouring pixels. The tracks initiated by the feature detection algorithm are validated against a number of criteria. The tracks are kept in memory until their track lifetime expires. On creation and update, these are saved to a database and made available to the real-time monitoring front-end.

Simulations on synthetic data have shown that the two detection strategies developed in this investigation, can achieve a significant performance improvement when they are compare against existing methods. The MSDS approach is

particularly effective in detecting low SNR tracks. Its F1 score was also shown to be consistently better than the other approaches across all SNR levels. However, the improved detection rate of this approach comes at a computational cost. Future work on this algorithm can investigate if a computational speed up can be achieved using GPU architectures.

Future research should consider the realisation of a higher fidelity simulator of the real-world radar echoes emanating from LEO objects. Rather than relying on idealised track lines, this simulator should emulate the real-world echo emanating from an orbiting object such as those shown in Chapter 2. It could also model doppler migration effects which were not modelled in this work. The creation of such a simulator can be used to create a standard data set of spectrograms against which future detection algorithms can be benchmarked.

In the last couple of years, the BIRALES system has been routinely engaged in several observation campaigns. The algorithms discussed in this chapter were used to detect hundreds of orbital debris objects using this novel radar system. In the next chapter, we present some of the results obtained during these campaigns.

Chapter 5

Experimental Results

Since 2018, BIRALES has been engaged in hundreds of observation campaigns¹ that were meant to test its space surveillance capability. These campaigns amount to more than 1100 hours of observation time. Moreover, the radar has collected over 20 hours of raw antenna data that has been mostly used for the development and verification of the data processing pipelines and detection algorithms described in this work². A historical overview of the observation campaigns conducted by the BIRALES radar is shown in Figure 5.1.

This verification process led to the system's first operational use in the Tiangong-1 re-entry campaign in April 2018. Since then, this new SSA radar has generated over 3100 TDM of objects in LEO during both targeted campaigns as well as beam park experiments. These files have been used to obtain the target's orbital parameters using the tailor-made orbit determination algorithm, designed by the researchers of Politecnico di Milano.

The method uses the measured beam illumination sequence, range, and SNR profile to reconstruct the trajectory and estimate the complete orbital state of the object. The algorithm, called Multibeam Orbit Determination Algorithm (MODA), generates several possible first guesses of the object track by identifying the relative gain peak sequences that are consistent with the measurement beam illumination sequence. These tracks are passed through a filtering process that removes unrealistic paths and instances with large angular displacements between two consecutive gain peaks. The remaining trajectories are sorted according to the track that gives the best linear fit. Results on

¹ 910+ detection and 95+ calibration observations

² 9.2+ hours detection campaigns and 17+ hours calibration observations

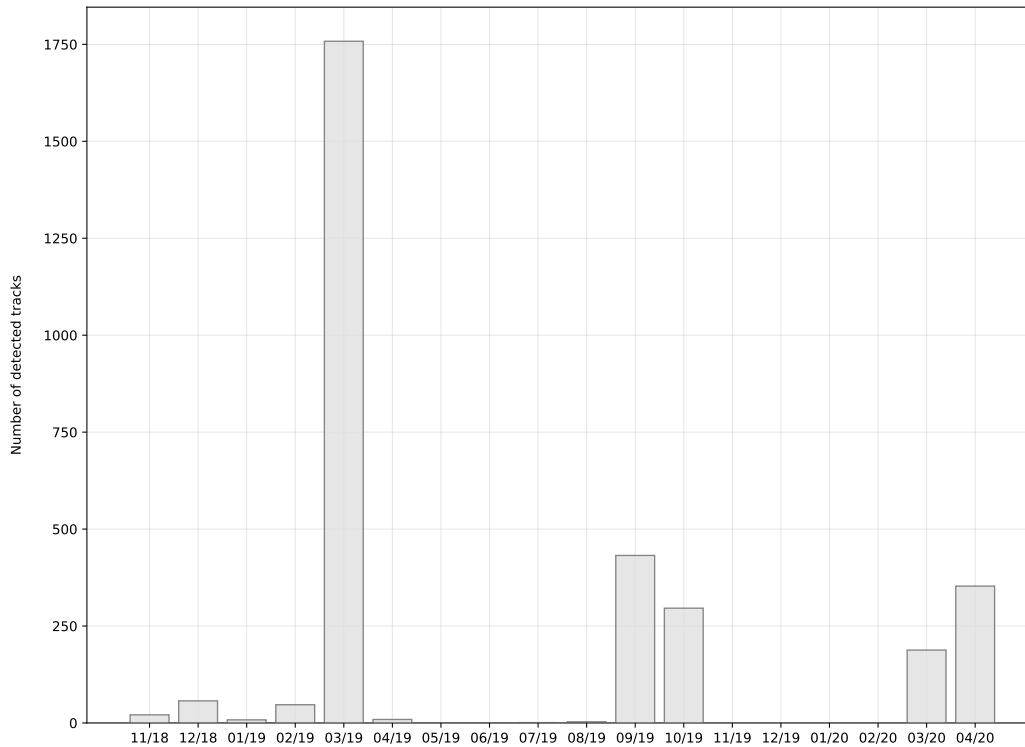


Figure 5.1: An overview of the observation campaigns conducted by the BIRALES radar

simulated data show that the theoretical error is expected to range from $1e-3$ to $1e-2$ deg. Further information on this algorithm can be found in [53].

To the author’s knowledge, this approach represents the first algorithm that exploits the multi-beam configuration of this radar for the reconstruction of the trajectory of an orbiting object. As an alternative approach, this study proposes a simple method of estimating the path of an object by considering only the data from the doppler system. This chapter presents some of the more notable results that were acquired since the inception of this novel SSA radar. These results represent the culmination of the work put into the present state of BIRALES.

5.1 Experimental results

In Chapter 2, the BIRALES radar was shown to be theoretically capable of detecting RSO targets in LEO. Throughout the last couple of years, the capability was experimentally proven during the aforementioned observation cam-

paigns. Some of these results obtained from these observation campaigns are illustrated in Figure 5.2 and Figure 5.3.

The results presented in this section were obtained using the MSDS algorithm using the tessellated multi-pixel configuration described in Chapter 3 (Figure 3.18). Prior to each observation campaign, a calibration observation was scheduled in order to obtain a calibration solution for the array. The target's RCS, range, transit time and Doppler information were taken from the object's TLE. These parameters were manually correlated with the detection data. A target was deemed to be successfully detected if the difference between the expected and measured transit time, δt , and doppler shift, δf , were very close ($\delta t \leq 15$ s and $\delta f \leq 400$ Hz).

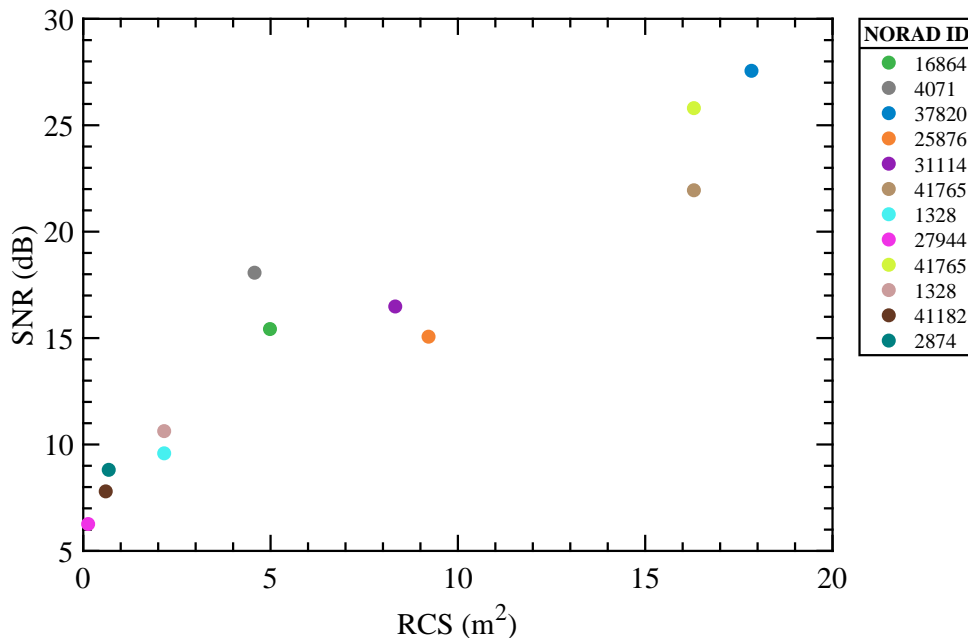


Figure 5.2: Detections of 12 known RSO targets acquired during various observation campaigns. Figure shows the SNR level measured as a function of the target's RCS

One may note that, as expected, the radar has no difficulty in detecting the larger objects (>10 m²). Indeed, these objects are detected at an SNR level in excess of 20 dB. The high SNR measured can also be attributed to the fact that the slant range of these targets was less than 1000 km.

The detection of smaller targets is more challenging. However, one may observe that the radar has shown that it is capable of detecting objects down to an RCS of 1 m². These targets were measured at an SNR level of less than

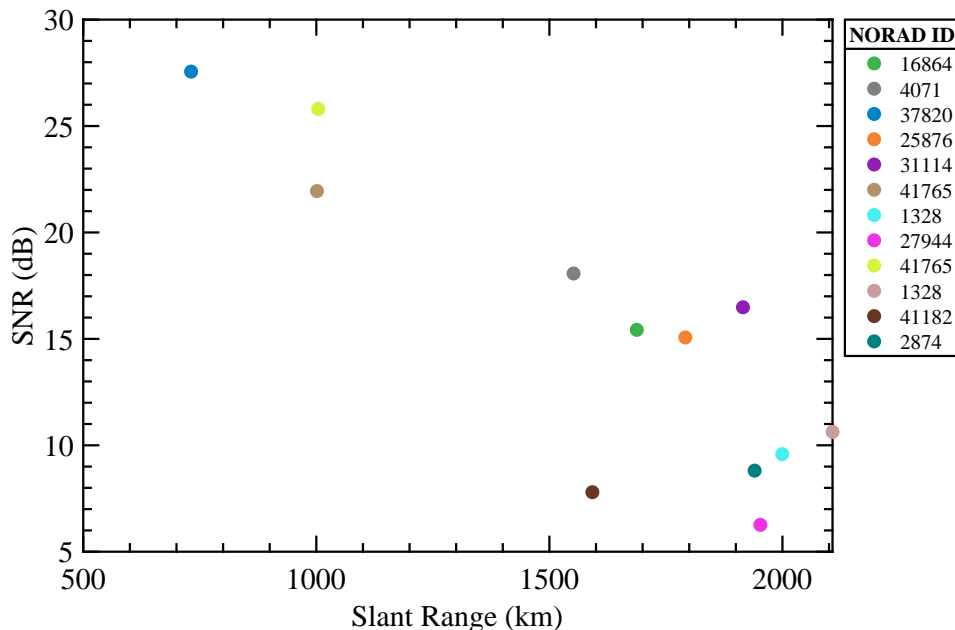


Figure 5.3: Detections of 12 known RSO targets acquired during various BIRALES observation campaigns. Figure shows the slant range of the target objects as a function of the SNR level measured

10 dB which is less than the detection threshold used in simulations presented in Chapter 2. For instance, NORAD 27944, having an RCS of 0.13 m^2 was detected at an SNR level of 6 dB at a slant range of over 1900 km. The detection of these radar echoes at these SNR levels are testament to the sensitivity of the detection algorithm employed.

The results from these observations can also be used to obtain an estimate for the system loss of the BIRALES radar. Re-arranging Equation 2.45, the total loss L of the radar can be calculated using,

$$L = \frac{\sigma_{\min} G_t A_e P_t}{\rho k B T \pi^2 4 (R_1 R_2)^2} \quad (5.1)$$

Thus, the system loss L_{sys} for the radar can be obtained by subtracting the atmospheric loss from the total loss. The mean system loss, calculated from the system loss obtained for each of the aforementioned targets, was estimated to be 15.98 ± 4.49 dB.

A limitation of this method, however, is that the target information was retrieved using TLE, which is not guaranteed to be precise. A precise value for the system loss can be obtained if calibration spheres, such as Lincoln

Calibration Sphere (LCS), whose orbital parameters are known accurately, are used as targets.

It is important to highlight the fact that the detection data was correlated manually with the catalogued objects. Such a process is laborious and not feasible for long running campaigns such as beam park experiments. Thus, further studies should investigate new techniques that automatically correlate these detections with catalogued objects. This should also make it possible to identify uncatalogued objects, such as new orbital objects, automatically.

In the next sections, we analyse the detection data obtained for two of the aforementioned targets. The intention is to showcase the typical detection vectors, such as Doppler shift and transit time, that are obtained. Additionally, we investigate the use of the beam illumination sequence within the multi-pixel configuration as a means of determining the target's trajectory over the FoV of the instrument.

5.2 The re-entry of the Tiangong-1 space station

One of the first operational uses of the BIRALES system was in the monitoring of the re-entry of China's first prototype space station, the Tiangong-1. The 8.5 t space station was in orbit for six years until it was decommissioned in 2013. The Chinese space station was scheduled to have a controlled re-entry in which the station is manoeuvred into a safe unpopulated zone on Earth. However, in March 2016, the Tiangong-1 operators reported that they have lost control of the station. It had been falling uncontrollably ever since.

In satellite re-entries, the heat generated by the friction with the atmosphere can completely destroy the satellite. In some cases, the satellite is not completely burnt up and parts of it make it to the surface of the Earth. Experts predicted that the Tiangong-1 space station would not burn up completely and may result in pieces of debris of up to 100 kg hitting the Earth's surface over an area a few hundred kilometres in size. While the probability of the space station falling on populated areas is small, it is difficult to estimate when and where this will land to a high degree of accuracy. In fact, such a prediction is only available just a few hours before it starts its decent.

Consequently, several SST sensors were engaged in the monitoring of its descent. Its decaying orbit was being monitored and updated with each pass

of the Tiangong-1 over the instruments. The BIRALES system was one of the European sensors within the European Union (EU)'s SST consortium that were actively engaged in monitoring its descent. This campaign consisted of daily measurements of the stations decaying orbit. The measurements were exported in TDM format to the competent Italian authorities and European partners.

On the 29th of March 2018, the BIRALES system was the first instrument to detect the ill-fated space station after more than 15 hours as the station passed through a no-visibility area for the US radars. This detection was a welcomed result by the international community. It represents the orbital state of the station just three days before its fiery re-entry on April 2nd at 00:15 UTC.

Transit time (UTC)	07:56:15
TRF Elevation ($^{\circ}$)	25.61
TRF Azimuth ($^{\circ}$)	28.80
BEST-2 Declination ($^{\circ}$)	-4.65
Range _{Tx} (km)	430.60
Range _{Rx} (km)	297.14
Slant Range (km)	727.74
RCS (m ²)	17.84
Doppler shift (Hz)	-4453.52

Table 5.1: The parameters for the Tiangong-1 observation campaign on 29th March, 2018

The parameters of this observation are represented in Table 5.1. The detected doppler-shifted radar echo reflected off the space station is illustrated in Figure 5.4. The figure shows the Doppler shift relationship with time as the station passed through the instrument's FoV. As one may observe, a strong linear relationship between frequency and time (r-value = -0.9994).

The SNR profile of this detection is presented in Figure 5.5. As expected from a target object of the size and at this range, a strong SNR is measured across all the 29 beams within the multi-pixel. One may also note that the target was detected at within the side-lobe and grating lobes of the beam. These detections can introduce ambiguities in the path taken by the object.

The transit time of the target object was expected at 07:56:15 UTC at a Doppler shift of -4453.52 Hz. The transit time of the space station was registered in the central beam at 07:56:02 UTC at a Doppler shift of -4549.94 Hz.

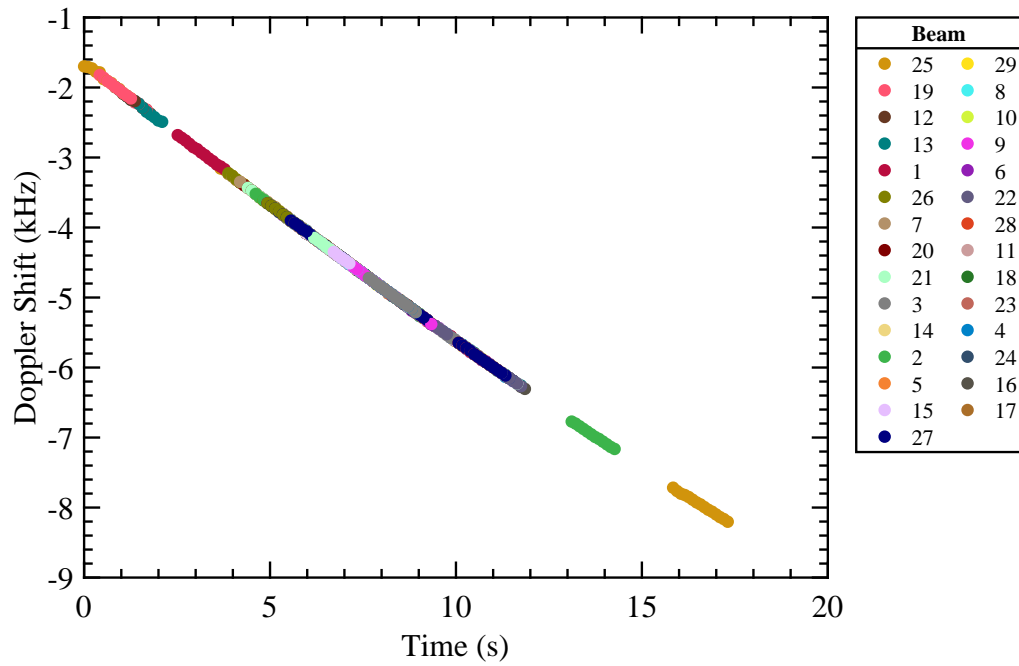


Figure 5.4: The measured Doppler shift against time sample. Tiangong-1 detection on March 29th, 2018

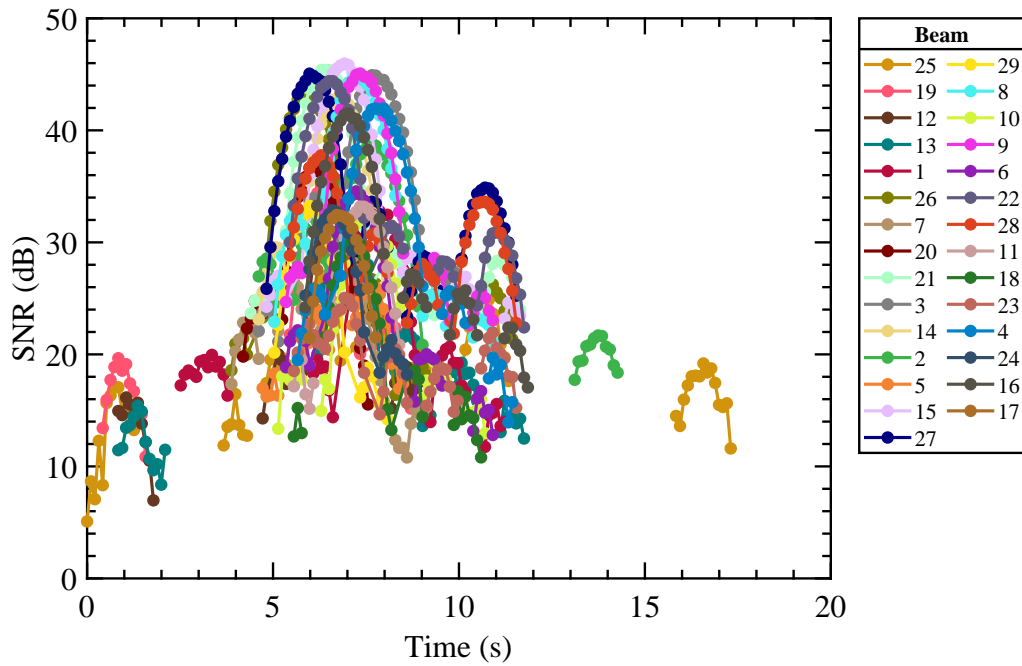


Figure 5.5: The SNR profile across the activated beams. Tiangong-1 detection on March 29th, 2018

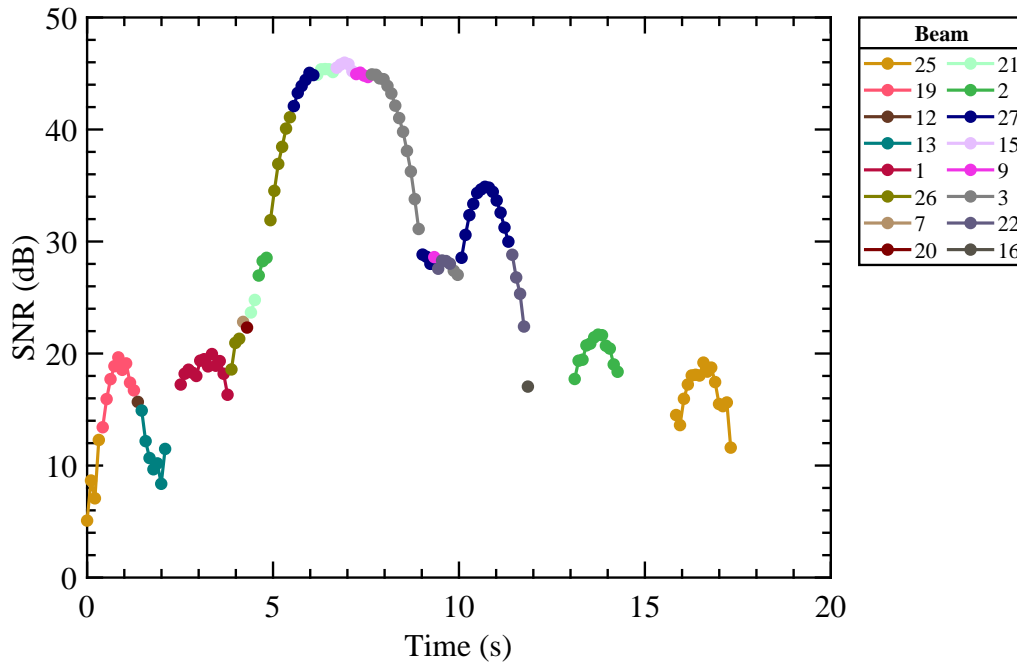


Figure 5.6: The SNR profile across the activated beams produced by taking the beam at which the maximum SNR, per time epoch, was measured. Tiangong-1 detection on March 29th, 2018

This meant that the transit time was detected more than 13 s earlier than expected. This disagreement was attributed to the unpredictable nature of the object’s orbit as it enters the denser parts of the atmosphere during its final re-entry. This unpredictability highlights the importance of these monitoring campaigns.

The sequence delineating the time of transit of an object within the individual beams is known as the beam illumination sequence. It was determined by considering the peak SNR at each time epoch. The results of this approach are shown in Figure 5.6. We assumed that the target passes at the points where the maximum SNR is measured. This also implies that only the main lobe profile, for each beam, has to be taken into account.

The beam illumination sequence can be used to derive the path taken by the target object as it crosses the FoV of the instrument. This can be achieved by analysing which beams within the multi-pixel were illuminated and at which order. If the pointing of each beam is known, the AZ and EL pointings through which the target passed can be determined.

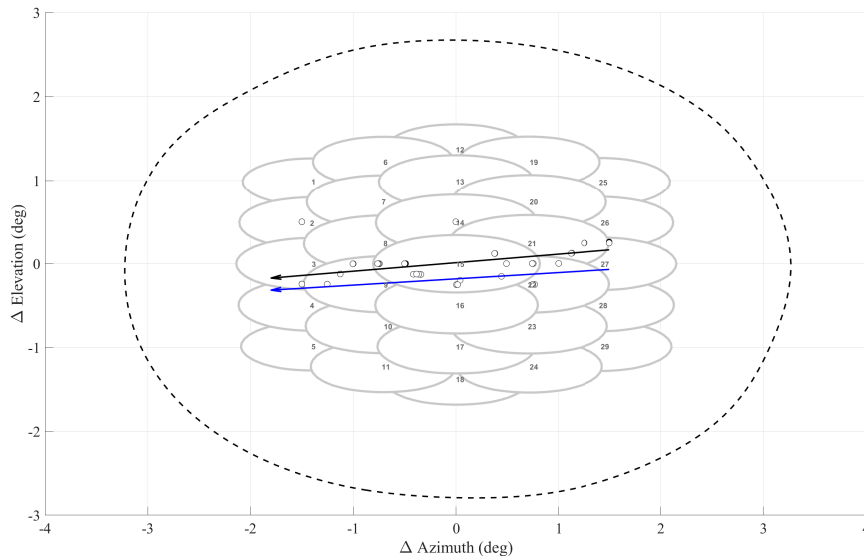


Figure 5.7: The reconstructed trajectory of the RSO (black), together with the trajectory predicted by the latest TLE (blue). Data points represent the weighted mean of the beam pointings in which a detection is made. Pointings are expressed as angular deviation from the reference pointing (EL = 41.14°, Azimuth (AZ) = 180°). Tiangong-1 detection on March 29th, 2018

A track \mathbf{T} spanning k time samples and detected across N beams can be represented as $\mathbf{T}(\mathbf{t}) = [f(t), s(t), b(t)]$, $t \in \{0, 1, \dots, k-1\}$, where $f(t)$ is the Doppler shift, $s(t)$ is the measured SNR and $b(t) \in \{0, 1, \dots, N-1\}$ is the beam the detection was made at a time sample t . If the pointing angle $p_b(\theta, \phi)$ of each beam is known, the AZ and EL pointings through which the target passed can be determined. For a data point i , detected at a time sample t , within beam b , the corresponding θ, ϕ angle, denoted by $p_i(\theta, \phi)$, is given by the beam's pointing $p_i = p_b(\theta, \phi)$.

There are two approaches that were investigated to determine the path of an object at each time sample. The first approach, shown earlier, was to take the pointing at which the maximum SNR was measured. Another approach, and the one used in the ensuing discussion, is to take a weighted mean, $\bar{p}(\theta, \phi)$, of the pointings at which a detection is made. This is given by,

$$\bar{p}(\theta, \phi) = \sum_{i=1}^n w_i p_i \quad (5.2)$$

where, w_i is the normalised SNR level measured in that beam. This process is repeated for all time samples such that the path taken by the RSO, expressed as a vector of pointings, can be reconstructed. The pointing of the beams is assumed to be the AZ and EL pointing at which the maximum gain is recorded. The maximum gain is given by the multi-pixel configuration obtained through simulation.

As was discussed in Chapter 2 the multi-pixel changes with declination. The multi-pixel configuration at this declination (41.14 deg EL and 180° AZ), is shown in Figure 5.7. One may observe that at this declination, the beam widths at -3 dB are larger than the zenith case. This reaffirms the importance of having an accurate model of the BEST-2 array. The implication is that the multi-pixel should be simulated at each angle of elevation given that this changes as a function of the array's declination.

The figure also illustrates the predicted path taken by space station (in black) when this is compared with the expected trajectory extracted from the latest TLE data (in blue). The Root Mean Square Error (RMSE) between the predicted and the measured trajectory was calculated to be 0.19° . This discrepancy is attributed to the inherent uncertainty of the TLE for an RSO during re-entry. In fact, re-entry campaigns usually involve multiple sensors across the globe where the measurement data for the object is shared to re-fine its orbital parameters upon each pass over a sensor within its network. The BIRALES radar was one such sensor involved in the last few days before the Tiangong-1 re-entry.

5.3 NORAD 1328

On March 5th, 2019, the BIRALES system was used in its TRF-Medicina configuration for another routine targeted campaign. In order to increase the likelihood of a detection, objects with an RCS greater than (2 m^2) were chosen as targets in these campaigns. One such RSO was the Explorer 27 (NORAD 1328) decommissioned satellite. Launched on April 1965, Explorer 27 has a RCS of 2.16 m^2 and orbits the Earth at a perigee altitude of around 926.8 km. The satellite was subsequently decommissioned in July, 1973.

Table 5.2 lists the parameters used for this observation. The BEST-2 declination was put to 21.24° whilst the transmitter was pointed to 45.24° AZ and 73.07° EL. At these pointings, the slant range was expected to be 2107.4 km.

Transit time (UTC)	10:37:53
TRF Elevation ($^\circ$)	73.07
TRF Azimuth ($^\circ$)	45.24
BEST-2 Declination ($^\circ$)	21.24
Range _{Tx} (km)	1035.56
Range _{Rx} (km)	1071.84
Slant Range (km)	2107.40
RCS (m^2)	2.16
Doppler shift (Hz)	-1462.14

Table 5.2: The parameters for the NORAD 1328 observation campaign on 5th March, 2019

The BIRALES system was able to successfully detect the radar echo reflected by the target RSO. Figure 5.8 illustrates the linear relationship between the measured Doppler shift and time (r-value = -0.99991). Such a strong linear relationship together with the measured Doppler shift is evidence of a hyper-velocity object crossing the FoV of the instrument.

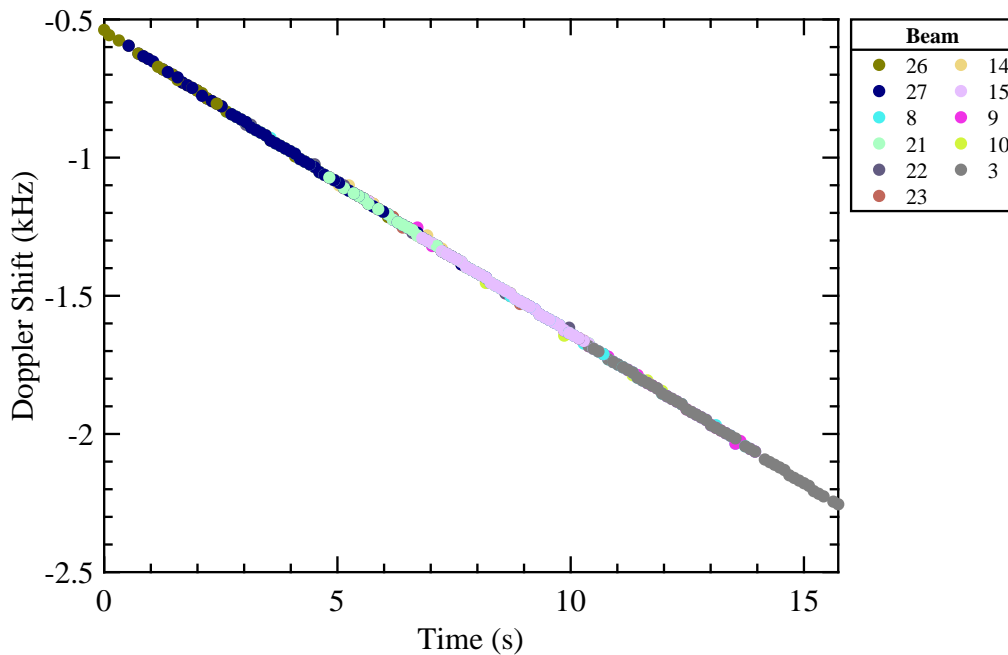


Figure 5.8: The measured Doppler shift against time. NORAD 1328 detection on March 5th, 2019

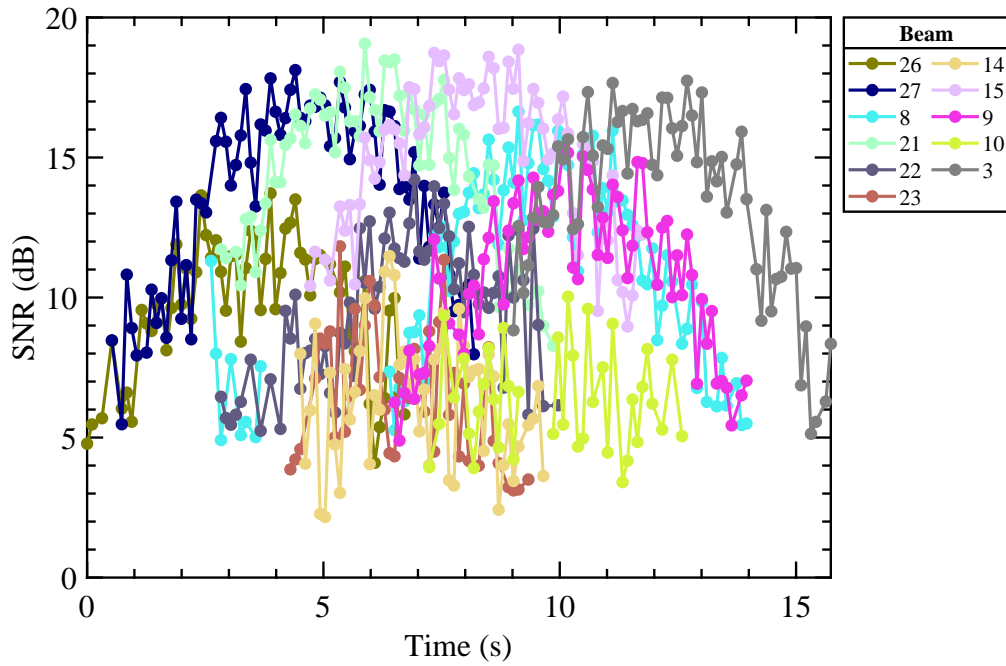


Figure 5.9: The SNR profile across the activated beams. NORAD 1328 detection on March 5th, 2019

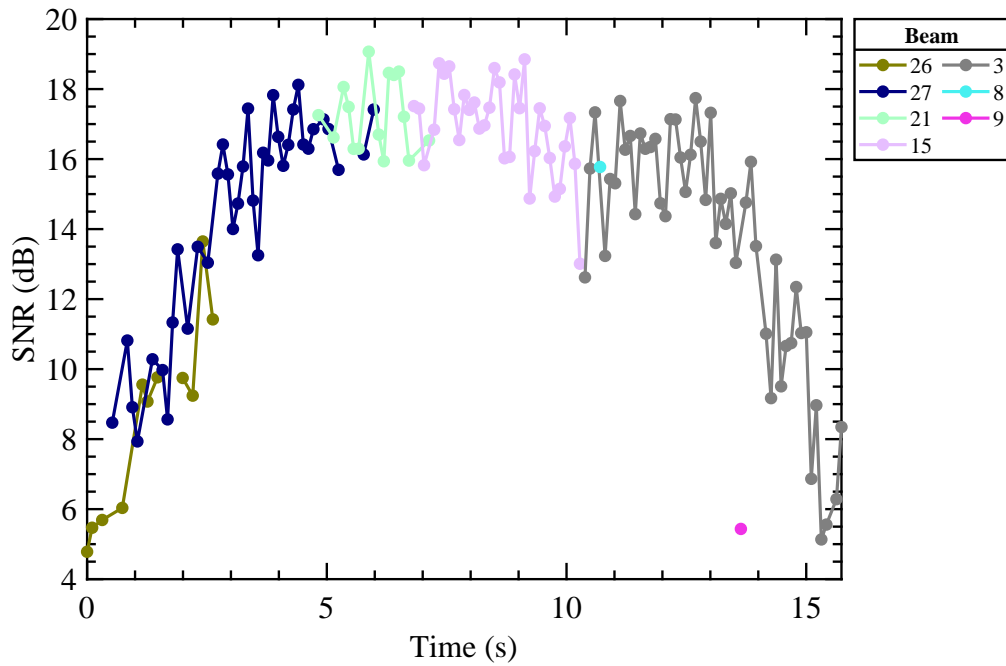


Figure 5.10: The SNR profile across the activated beams produced by taking the beam at which the maximum SNR, per time epoch, was measured. NORAD 1328 detection on March 5th, 2019

Figure 5.9 illustrates the SNR profile of the detection with time while the beam illumination sequence is shown in Figure 5.10. It can be noted that the radar echo was detected across several beams of the multi-pixel. A strong SNR was measured in each of these beams, with the highest SNR value of 19.07 dB. Taking the median time sample as the transit time of the RSO, the target object crossed beam 15 at 10:37:53 UTC at a Doppler shift of -1357.99 Hz. Table 5.2, gives an expected Doppler shift of -1462.14 Hz at 10:37:53 UTC which is very close to the experimental values.

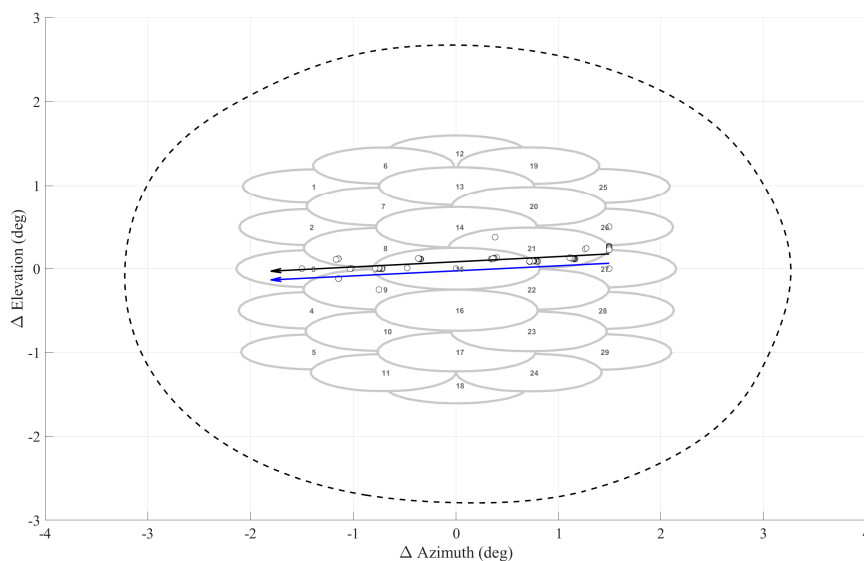


Figure 5.11: The reconstructed trajectory of the RSO (black), together with the trajectory predicted by the latest TLE (blue). Pointings are expressed as angular deviation from the reference pointing ($EL = 66.72^\circ$, $AZ = 180^\circ$). NORAD 1328 detection on March 5th, 2019

The predicted path of the object is shown in Figure 5.11. At a pointing angle of 66.72° EL and 180° AZ, the beam width along the EL direction are smaller than the zenith case. In this case, one may note that the beam arrangement is more efficient since the overlap between the beams is minimised.

In this case, an RMSE of 0.10° between the predicted and the expected trajectory suggests that the predicted trajectory is very close to the one expected. However, one can observe an offset between the measured and the expected path. Such an error would still result in appreciably significant errors in position a velocity rendering an accurate Initial Orbit Determination (IOD) measurement difficult. Future research should certainly further test

whether the accuracy of the reconstructed trajectory can be improved if ranging information is used. These studies should also investigate whether such an approach can be integrated with more rigorous IOD algorithms such as the MODA algorithm developed at the Politecnico di Milano. It would also be interesting to test MODA's performance using real-world data such as those presented in this section.

The positive results presented through these two expository examples show that, in principle, it is possible to obtain an estimate of the trajectory of the object can be obtained. However, thus far, this is still considered to be an initial approximation and not suitable for the precise determination of an object's orbit. For such a calculation, ranging information is necessary to completely characterise the object's orbital parameters. These preliminary results, pave the way for further research into this method of determining an object's trajectory.

5.4 Conclusion

In this chapter, the results obtained during a number of observation campaigns were presented. Experimental results have shown that the system is capable of detecting catalogued objects with an RCS of less than 1 m^2 at a slant range of more than 1900 km. These results are at the limit of the design specifications of this new radar.

Apart from routine measurements of known objects, the radar has also been part of an international monitoring campaign of the Tiangong-1 re-entry. On May 11th, the radar was engaged in the monitoring of the 21 t Long March 5B rocket body. These achievements mark one of the latest positive developments of the EU SST program.

While the results are promising, the system is still constantly being improved in order to enhance the capability of this new radar. This provides a good starting point for discussion and further research.

For instance, future studies should aim to confirm the estimated system loss presented in this chapter. A more precise measurement of the system loss of the radar can be achieved if calibration spheres, with a precisely defined radar cross-section and range, are used.

The planned future upgrades to the BEST-2 array are meant to improve the sensitivity of the instrument. In so doing, objects with a smaller RCS can be detected at farther distances. An enhanced sensitivity is essential for routine beam park experiments meant to discover new uncatalogued space debris objects. Such experiments would necessitate the introduction of algorithms that can automatically correlate the detection data with known objects such that unknown objects can be discovered. The in-depth analysis of the detected data in such campaigns are used to characterise the near Earth space environment and assess the growth trends of the orbital debris population.

Potentially, this data can be used to create an independent catalogue for the system such as that of the French GRAVES system. This catalogue can be compared with existing public catalogues and be made available to the international space community. In so doing, the system would play an important role in the mitigation of such the international effort required for the future sustainability of space. The conclusions of this study together with the planned future extensions of this work are summarised in the next chapter.

Chapter 6

Conclusion

The world's economy has become heavily dependant on the services provided by satellites. With the exponential increase in satellite launches, the population of defunct or inactive hardware in space has grown substantially. This is especially true in sensitive orbits such as the LEO and GEO regimes. These objects, collectively known as orbital debris, can reach speeds of up to $28\,000\text{ km h}^{-1}$ in LEO. At these orbital speeds, even the smallest of objects can pose a considerable threat to the operational satellites or astronauts. A potential in-orbit collision could create a cloud of debris which can in turn cause a catastrophic cascade of further collisions that can lead to a situation where the space environment is unusable. This makes the monitoring of these objects of the utmost importance.

Unfortunately, there are a limited number of European facilities that are routinely engaged in the detection and tracking of orbital debris. The ESA's SST programme was established to address this deficit by building new facilities and upgrading existing systems for their potential use in SSA. One of the latest facilities within the ESA SST consortium is a new SSA radar named BIRALES that is the focus of this work. BIRALES is a bi-static radar consisting of a CW transmitter in Sardinia, Italy and the BEST-2 radio telescope located within the Northern Cross radio telescope in Medicina near Bologna, Italy.

This work set out to investigate the use of this radio telescope in the detection of orbital debris. The aim of this study was to lay out the foundations necessary for the realisation of the first operational space debris detection radar in Italy. Consequently, the key outcomes of this investigation were presented in this work.

In Chapter 2, it was shown that the BEST-2 astronomical instrument is a suitable receiver for a new bi-static radar. Simulations showed that if the receiver is coupled with a powerful CW transmitter in the northern hemisphere, the radar is able to detect LEO objects. In addition, if the radiation pattern of the receiver is known, the trajectory of the RSO can be estimated. This is achieved by considering the illumination sequence of the array's beams as the transient passes over the FoV of the instrument. An accurate characterisation of the array's theoretical beam pattern can be obtained through a full electromagnetic simulation. However, the true assessment of the instrument's actual radiation pattern is ultimately achieved by in-situ experiments carried out by an antenna verification system.

This study introduces a new UAV-based antenna verification system, called ChopPy. ChopPy was designed to be an end-to-end solution that is capable of characterising the far-field radiation pattern of large radio telescopes whose study in anechoic chambers is impractical. Researchers have only recently been using drone-based antenna verification systems and to date no commercial system is available. Unlike existing prototypes, ChopPy cuts down on the time taken to characterise an antenna by implementing a real-time data acquisition system. In ChopPy, the position of the transmitter is combined with the antenna's response through a specially designed real-time synchronisation algorithm. The system is still in preliminary stages, however the results on smaller antennas have been encouraging. Its applicability to the BEST-2 antenna is the subject of ongoing research.

The realisation of a new radar for space debris detection necessitated the implementation of a new software backend for the BEST-2 array's digital backend. Chapter 3 introduced the PyBirales data processing backend. PyBirales is a Python application that is used to process the incoming signals from the instrument's 32 receivers. The application processes one, 78 kHz wide, single polarisation, channel using a system of processing pipelines. A processing pipeline is a software construct that uses a series of modules that are chained together in such a way that the output of one processing module is the input to another module. At each module, the input data is mutated in real-time.

The detection pipeline is designed to sieve through the input data for radar echoes reflected off hyper-velocity in-orbit objects. The signals from the 32 antennas are beamformed into a 32-beam multi-pixel covering the FoV of the instrument. Each beam is finely channelized at a spectral resolution of around

9.5 Hz and a temporal resolution of around 100 ms. Chapter 4 presented the track detection strategy used by the detection pipeline. The strategy consists of an image segmentation stage that is used to filter the incoming data from the background noise and any RFI interference. Filtering the data reduces the number of data points that are processed by the subsequent feature extraction algorithm.

This work presented two methods of extracting the track information from the incoming spectrogram data. The first method uses a popular clustering algorithm, called DBSCAN, to detect the linear radar echoes. This approach was shown to be effective at detecting linear streaks in spectrogram images. However, the precision and recall score fell dramatically for low-SNR tracks. These limitations were addressed with the introduction of a new track detection algorithm, called MSDS. This algorithm is a bottom-up approach which makes use of single-linkage clustering to identify faint radar streaks. Tests on synthetic data have shown that the algorithm obtains a substantially better recall and precision score when compared with existing methods. Unlike other approaches, the MSDS algorithm was still able to recall 90% of the track information at an SNR of 2 dB.

A selection of the results obtained in various test campaigns were presented in Chapter 5. It was shown that the system is capable of detecting radar signatures reflected from objects with an RCS of less than 0.15 m^2 at a slant range of more than 1900 km. A high level of agreement was achieved between the measured and the expected orbital state of the target object. The results are representative of a series of test campaigns which led to the instrument's monitoring of the Tiangong-1 space station's uncontrolled re-entry. In this campaign, BIRALES joined an international network of sensors monitoring the station's decaying orbit a few days before its re-entry. The positive results obtained during the various observation campaigns together with the deliverables of this work, lay the foundation on which future extensions to this work can build upon.

6.1 Future work

The results obtained in this study are promising, however, they are still preliminary and further work is needed before the system can be used for the

routine tracking of orbital debris whose orbital state is not known a priori. In this investigation it was shown that an accurate prediction of the trajectory and, subsequently, orbit determination of the detected targets is not possible without a deep understanding of the position and shape of the main beams and their respective side lobes. Thus, the verification of the model can be achieved experimentally using an antenna verification system such as that proposed in this study. This is the subject of future work.

Recently, work started on upgrading the BEST-2 array to its BEST-3 configuration. The upgraded system increases the number of receivers to 56 installed on 14 cylinders along the Northern Cross. This upgrade increases the collecting area from the current 1410 m^2 to 7260 m^2 [60]. The increase in data rate has yet to be tested on the data processing software developed for the BEST-2 array. It is envisaged that some of the modules, such as the Detection module, would need to be optimised in order to handle the increased data rate.

The detection algorithms investigated in this study were evaluated using ideal linear streaks within spectrogram images. These results can be reproduced on test data generated by a high-fidelity orbital simulator that emulates the radar echo streaks emanating from high-velocity orbital objects. Such a simulator would take into account, the radiation pattern of the receiver, the object's range and RCS to generate the expected radar echo. Ranging information can also be used to improve the existing detection techniques presented in this study. Future studies can investigate how ranging information can enhance the false-positive rejection rates and thereby increasing the precision of the proposed approaches.

Further test and observation campaigns are envisaged in order to verify the system suitability in the routine detection of orbital debris. Routine beam park experiments can be performed to potentially discover new uncatalogued orbital objects thereby fulfilling the European overarching SSA commitment. The ultimate goal of these advances is to build upon the results achieved thus far in the quest for the continued enhancement of Europe's latest orbital debris monitoring system.

Appendix A

Appendix

A.1 Antenna Verification

Antenna verification is a term that is usually used to describe a series of experiments that are performed on an antenna to characterise its radiation pattern in real operative conditions. This process is particularly useful in novel antenna designs whose radiation pattern is not known. It is also valuable for the validation of simulations for these types of antennas. The data derived from these experiments can also be used for calibrating the instrument and maximise its efficiency.

The study of an antenna is typically performed in a controlled environment which is shielded from external RFI sources such as an-echoic chambers. These experiments can give the radiation pattern of the Antenna Under Test (AUT) to a high degree of accuracy. However, these chambers can only accommodate small antennas that are a few meters in size. This limitation prohibits their use in the study of the large antennas that are typical of radio astronomy.

Radio telescopes, such as the Northern Cross, can extend to hundreds of meters, making their study in an-echoic chambers difficult. Thus, these types of antennas have to be studied in-situ. These experiments shed light into the influence of the surrounding environment, such as soil and background RFI, on the AUT [182]. Furthermore, they are also useful to establish the present state of an antenna. Such a system is particularly helpful in the study of older antennas whose performance may have degraded over time.

Traditionally, the study and beam calibration of antennas is performed through the use of a bright astronomical source such as the sun [183] or known

radio sources [184]. As will be discussed in Chapter 3, this is the method that is used to calibrate the BEST-2 array. The beam pattern of the AUT is obtained by measuring the power signal being the output of the AUT as the astronomical source passes through the beam. The limitation of this method is that the number of available strong radio sources is limited and not readily available. Thus, artificial, high-altitude, RF sources such as balloons or helicopters [185, 186] have also been investigated. However, such techniques are often not trivial to set-up and are very expensive.

In recent years, less expensive solutions that make use of commercial drones equipped with an RF source, have been introduced. There have been several studies detailing the results obtained by these systems. This methodology was used in the measurements of smaller antenna elements such as biconical and log-periodic antennas in [187] and [188]. Digitally beam-formed arrays were also investigated in [189], whilst small radio dishes have also been characterised in [190] at VHF and in UHF [71].

Conventional systems use a total station to pin-point the drone in 3D space. While this system poses some advantages, it can be challenging to align the drone with the base station, especially as its altitude increases. With the increased accuracy and reliability of commercial GNSS solutions, the use of an accurate GNSS device has been proposed as an alternative way to track the drone in 3D space.

These studies combine the output power of the AUT at a particular frequency with the position of the GNSS at a final post-processing stage once the drone lands. Given the limited flight-time of these drones, the full assessment of an antenna typically requires multiple flights. The acquisition of these measurements is very time-consuming. Thus, to cater for these issues and improve on existing systems, this work introduces a new control system capable of testing the far-field of an antenna in real-time, drastically decreasing the time needed to obtain the beam pattern of the AUT. The aim of the system, named ChopPy, is to put in place the components necessary for the verification of large antennas, whose study using traditional methods, is either difficult or too time-consuming.

A.1.1 A real-time antenna verification system

ChopPy is an antenna verification system that was designed to be an end-to-end solution for the verification of an antenna's radiation pattern. The system makes use of a drone equipped with a variable RF source acting as a transmitter and a frequency spectrum analyser to read the corresponding power output measured by the AUT. As shown in Figure A.1, this system can be broadly split into two main components; the rover system and the control unit.

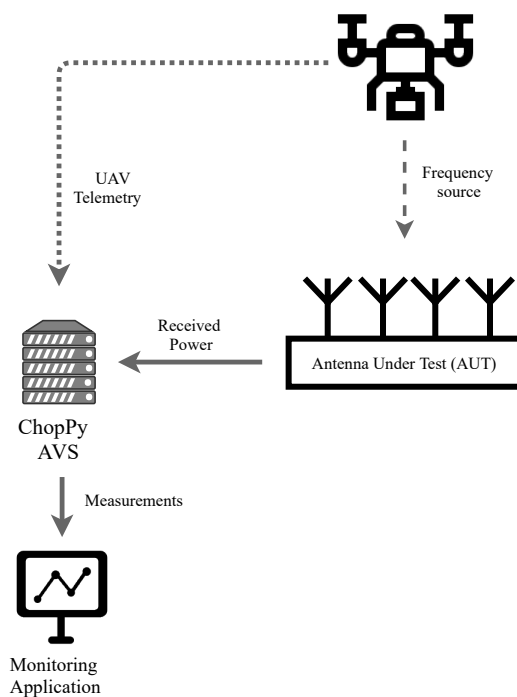


Figure A.1: System overview of the ChopPy antenna verification system

The Rover

ChopPy was designed to be independent of the vehicle that is used to manoeuvre the transmitting antenna. This feature makes it easily portable to the equipment available to the operators of the system. In this study, a Mikrocopter ARF-OktoXL 4S12¹ UAV was used. This commercially available UAV is an octocopter drone with a maximum payload of 2.5 kg. The maximum range

¹ www.mikrocontroller.com

of the drone while carrying a 1 kg payload, is that of a few hundred meters with a maximum flight time of less than 30 min on a 10 mA h charge. A custom payload box was built to house the components of the system, including the variable signal generator feeding the dipole antenna transmitter.

Accurate GNSS positioning was achieved by using two high precision GNSS modules (u-Blox NEO-M8P²) which are housed in the payload box. GNSS data from these devices, is extracted by a Python application running on a Raspberry Pi³ module which is also installed on the drone. This simple application, henceforth referred to as ChopPy-Rover reads the GNSS data from a standard serial (USB) port at 1 Pulse Per Second (PPS). Data is then published on the network as JSON strings through the ZeroMQ⁴ messaging library. At present, the data-link between the drone and the control unit is through a standard 3G connection.

The Control Unit

The system was designed to be able to work with any National Instruments - Virtual Instrument Software Architecture (NI-VISA)⁵ compatible device. As a result, ChopPy was made extensible to a wide range of devices which support the NI-VISA protocol. In this work, the response of the antenna is measured by an Anritsu⁶ MS2724B portable spectrum analyser.

The ChopPy control unit can be run on any standard machine. This machine is usually a portable device for practicality in on-site experiments. The control unit initiates a frequency sweep from the spectrum analyser which is connected to the control unit through an ethernet link. For every frequency sweep, the power at the test frequency is determined. The control unit is also responsible for combining these readings with the corresponding GNSS measurements which can arrive at different times. The interval at which the data is being polled is different. Whilst the GNSS can be polled at 1 PPS, the spectrum analyser can only extract a reading every ~ 5 s. Network latency issues in both the spectrum analyser and the ChopPy-Rover system can cause

² www.u-blox.com

³ www.raspberrypi.org

⁴ www.zeromq.org

⁵ www.ni.com/visa

⁶ www.anritsu.com

added random delays that are difficult to control. Furthermore, there could be instances where the connection between the control unit and the rover is lost. When the connection is re-established, the GNSS positions need to be matched with the corresponding power measurements.

It is thus essential to develop a system which can sync the data between the two devices. While this task can be done at a post-processing stage, where the time-stamps of the individual devices are matched, this application can do this in real-time. The advantage is that the analysis of the test antenna can be done on the fly, making it easier and faster to generate an accurate assessment of the test antenna. This is especially useful when the test antenna is spread over a large area such as those typical in radio astronomy.

A.1.2 Real-time synchronisation

The real-time synchronisation of the data is done at the control unit, which makes use of 2 separate non-blocking consumers: the GNSS and the spectrum analyser threads which consume the data coming from the respective devices. The synchronisation algorithm is described in Figure A.2.

The consumers push the data to a queue in a FIFO fashion. The algorithm is run iteratively through the duration of the campaign. A separate ‘combiner’ thread consumes data from these queues. This combiner thread blocks until a spectrum analyser reading become available.

A reading from the spectrum analyser is matched with a GNSS measurement whose time-stamp is closest. This is achieved by popping measurements from the GNSS queue iteratively until a match is found. In the case where no GNSS data is present in the queue, which could occur when the network connection is lost, the spectrum analyser measurements are queued. This way, the queue acts as a buffer and ensures that data losses are minimised. The synchronised measurements are saved to a MongoDB database and sent in real-time to a dedicated monitoring application through Socket.IO⁷.

⁷ www.socket.io

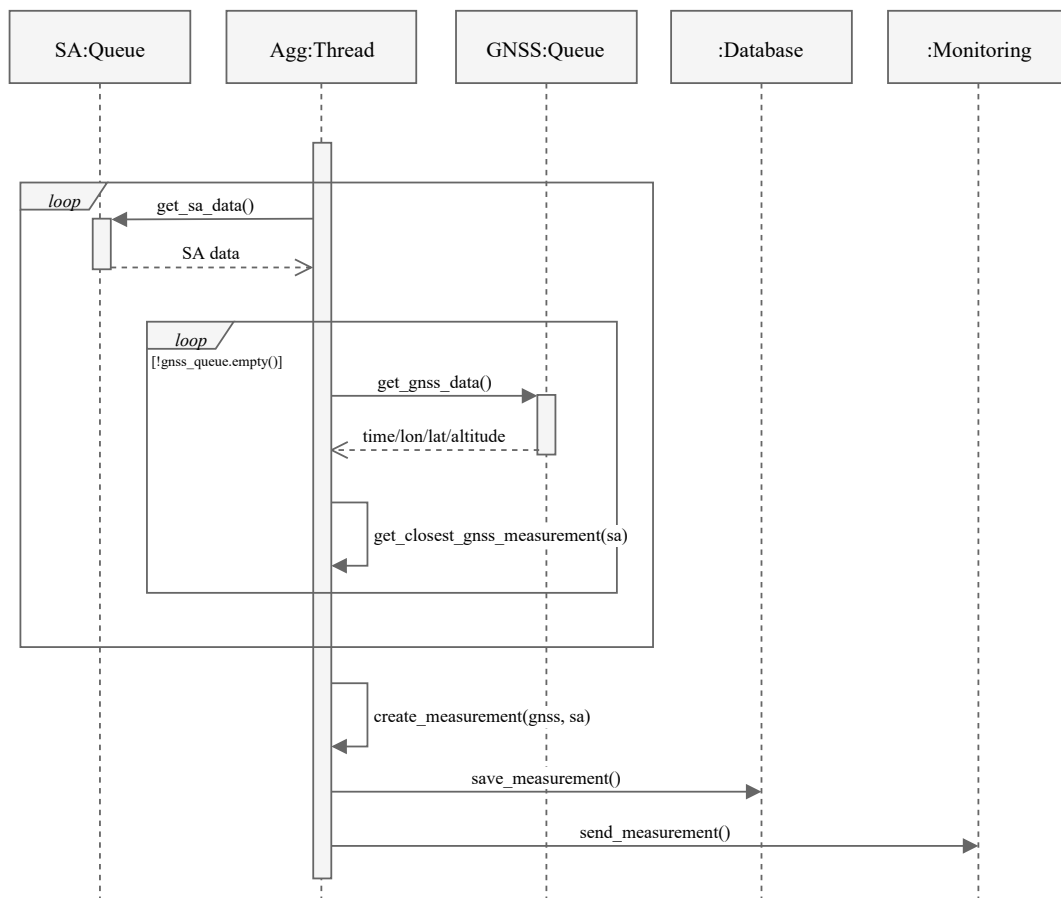


Figure A.2: A UML sequence diagram describing the real-time synchronisation algorithm used in ChopPy

A.1.3 Monitoring application

The monitoring application distributed as part of the ChopPy system was designed to visualise, in real-time, the measurements being acquired by the ChopPy system. This way, the user can monitor the measurement campaign and thereby be able to identify any potential problem quickly. Figure A.3 illustrates the real-time monitoring plots that are typical of a measurement campaign.

The antenna response to the transmitting drone is presented in the top right plot. This is helpful to assess the operating environment of the antenna. One can note that the antenna was tested in a very noisy environment where some RFI peaks are present. The frequency transmitted by the drone's antenna can be identified as a small peak at 1 GHz. The power at this frequency can be monitored over time by the second plot in the monitoring dashboard. In

this example, the power reading changes as the drone passes over the antenna and back again.

The altitude of the drone can be monitored in the bottom left plot in Figure A.3. As one may note, the drone's altitude is not perfectly constant throughout the flight path. This can be either due to windy conditions or inaccuracies in the drone's inbuilt guidance system. In this case, the height of the UAV above the antenna varies between (70 ± 2) m which can be considered to be constant with respect to the far-field condition for the particular AUT.

The path taken by the drone is visualised in the last plot in which part of the grid-like flight strategy can be seen. The flight path's colour represents the power response of the AUT at that coordinate. These plots give the operator an indication of the quality of the measured data before the subsequent post-processing stage.

A.1.4 Methodology

The measurements stored in the database mentioned above are used to generate the radiation pattern of the AUT. This is achieved by using the far-field two antenna method. The transmitter is kept at a constant distance from the AUT such that the far-field condition of the antenna is satisfied [191]. The far-field region R , of an antenna with a baseline D , operating at wavelength λ , is given by,

$$R > \frac{2D^2}{\lambda} \quad (\text{A.1})$$

Initial tests were carried out on small antennas whose radiation pattern is known. One such antenna is the log-periodic antenna whose model is shown in Figure A.4. The far-field region for this 95.1 cm antenna, is estimated to be at 6 m at 1 GHz. The gain of the antenna, under the far-field approximation is given by [187, 192],

$$G(\hat{r})M(\hat{r}) = \frac{P_R(\mathbf{r})}{G_S(\hat{r}, \alpha, \beta, \gamma)P_S G_R} \cdot \left(\frac{4\pi R}{\lambda}\right)^2 \quad (\text{A.2})$$

where, G is the gain of the antenna in spherical coordinates, \hat{r} is the unit vector, \mathbf{r} is the position vector of the transmitter (drone), M is the polarization mismatch and P_R is the received power as measured by the spectrum analyser.

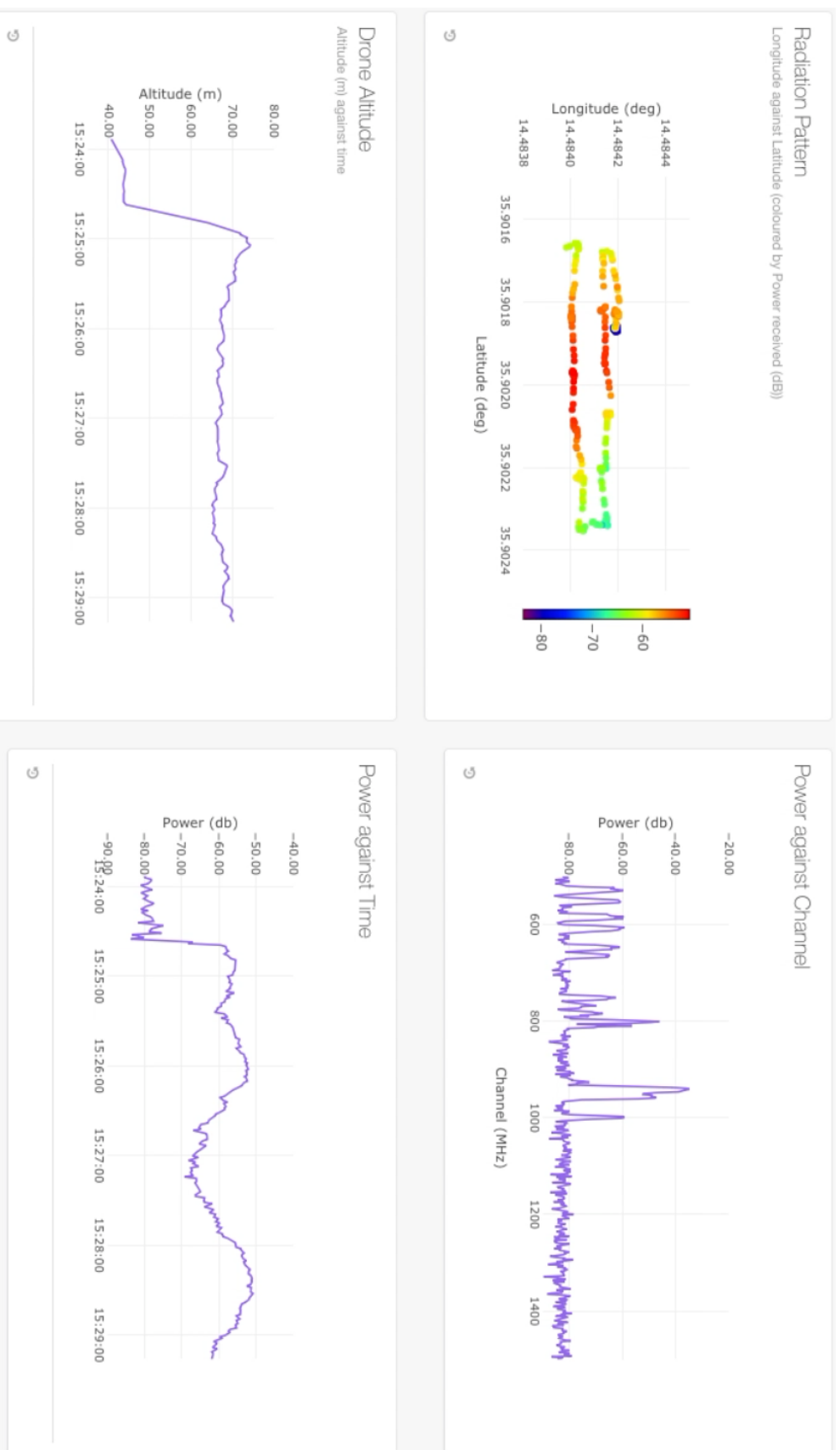


Figure A.3: The purpose-built monitoring application for the ChopPy antenna verification system. Going clockwise, the operator can monitor the AUT's power spectrum (top right) and the power received over time (lower right). The stability of the drone can be measured by the altitude plot (lower left). Finally, an indication of the power distribution can be seen in the top left figure.

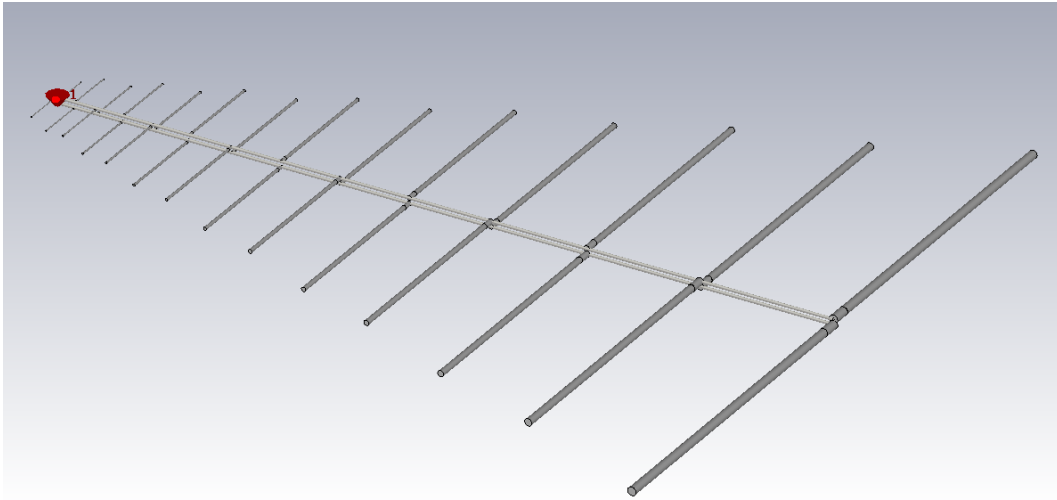


Figure A.4: The model of the log-periodic antenna used in the initial tests of the ChopPy system

The power of the transmitter is represented by P_S , and its radiation pattern is denoted by G_S . The angles α , β and γ are the bearing, pitch and roll of the UAV source while G_R accounts for the Low Noise Amplifier (LNA) gain and cable losses. Equation A.2 can be expressed in logarithmic decibel form, such that,

$$G(\text{dB}) = P_R(\text{dB}) - G_S(\text{dB}) - G_R(\text{dB}) - P_S(\text{dB}) - 20 \log \left(\frac{\lambda}{4\pi R} \right) \quad (\text{A.3})$$

Thus, the radiation pattern of an antenna is obtained by removing the contribution of the source antenna, the path loss quantities P_S and G_R from the measured power received by the ChopPy system. The drone is flown at a constant altitude above the far-field region in a quasi-rectangular grid covering a total area of 900 m^2 centred around the AUT. The orientation of the UAV is such that the flight path is aligned with the antenna's co-polar E-plane. As the drone manoeuvres through the pre-programmed flight path, its position is transmitted to the control unit in real-time.

Analysis of the received data is usually done in a separate post-processing step. The GNSS positioning of the UAV is transformed into a 2D cartesian coordinate system by projecting the coordinates to the Universal Transverse Mercator (UTM) coordinate system. At each point, the gain of the antenna at these positions is calculated through Equation A.3. The data is then linearly

interpolated across the whole domain such that the complete radiation pattern of the AUT can be obtained. The radiation pattern obtained experimentally can be validated against theoretical or simulated models of the AUT.

A.1.5 Results

The radiation pattern of the log-periodic antenna that was obtained using this system is shown in Figure A.5. The E-plane pattern obtained for the log-periodic antenna is shown in Figure A.6. Validation of the results was performed by comparing the measurements to the numerical simulations obtained from CST Microwave Studio.

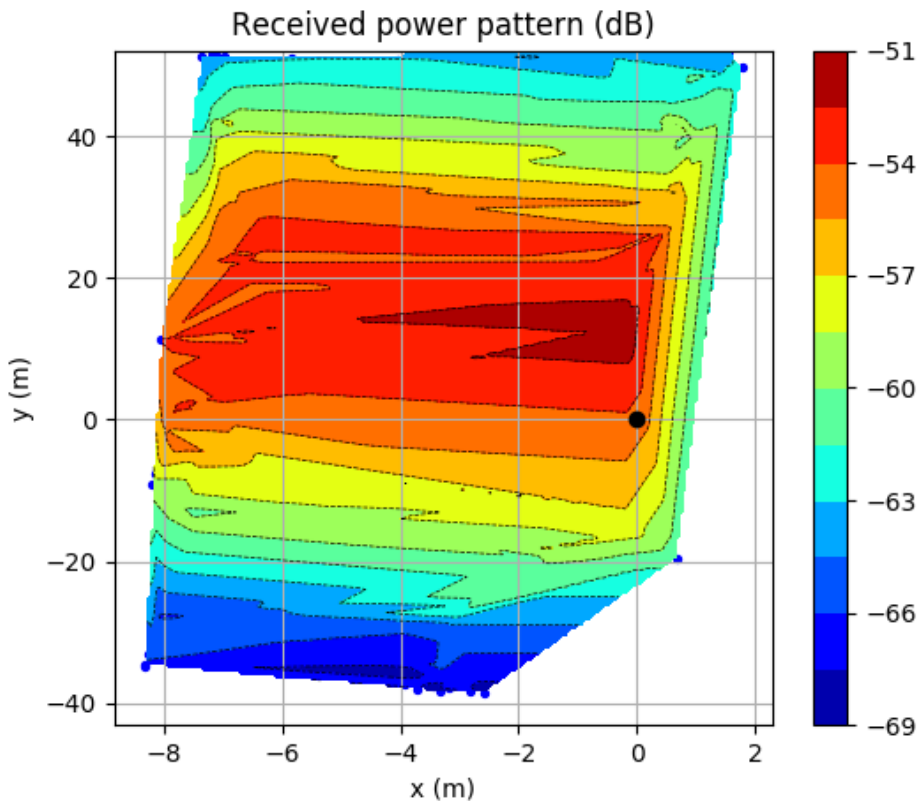


Figure A.5: The calculated radiation pattern for the log-periodic antenna at a frequency of 1 GHz in cartesian coordinates

The simulations of the AUT pattern are computed in the far-field region, neglecting the electromagnetic coupling between the AUT and the transmitting antenna. One can notice that there is a good agreement between the measured

and the simulated data. However, this agreement is not apparent for higher values of θ . The current understanding is that this is due to the background environment, such as the soil and nearby metallic structures, were not included in the simulation. Additionally, it would be interesting to compare these results with another study which scans a more substantial area over the antenna.

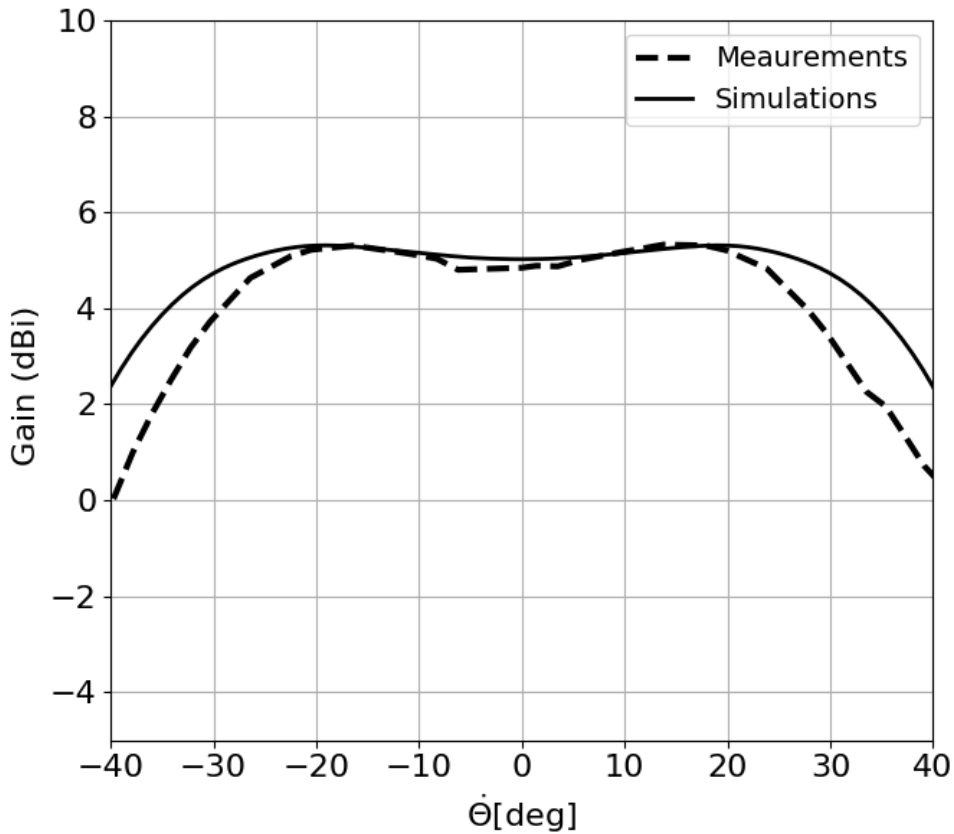


Figure A.6: The measured (dashed) and the simulated (solid) co-polar gain at the zenith in the E-plane for the log-periodic antenna

A.1.6 Future work

The ChopPy antenna verification system presented in the preceding sections marks the first step towards an inexpensive antenna verification system for large arrays. While the preliminary results are encouraging, several limitations need to be addressed before the system can be marketed as a robust method for antenna verification. For instance, the drone does not make use of the

external, accurate GNSS module for navigation. Consequently, its flight path and bearing are not precise. Furthermore, the drone's orientation (yaw, pitch and roll) are not being accounted for in the radiation pattern calculation. The system assumes that the drone's yaw is kept constant.

At present, ChopPy uses an off-the-shelf spectrum analyser to measure the power of the antenna as the artificial source flies over it. However, the rate of measurements of such a device is rather limited (1 measurement every 5 s). Ideally, the spectrum analyser is replaced by a high-performance digital backend which can achieve a higher data throughput. This results in a better characterisation of the AUT radiation pattern.

Another limitation is the 3G data link that is currently being used to transmit the drone's location. In radio-silent zones, this data link would also need to be changed to a dedicated data-link. A dedicated data-link would also make it possible to receive real-time telemetry over larger areas.

The goal of ChopPy is its deployment for the calibration of large phased arrays. However, if the system were to be used on the BEST-2 antenna, the transmitter would have to exceed a height of 1.5 km for just one parabolic reflector of the BEST-2 antenna. This rises to 13.4 km if the full array is used. At these, altitudes, a drone-based solution is not feasible. One solution is to modify the ChopPy system for use in non-drone vehicles, such as aircraft.

As a compromise, ChopPy can be used to characterise the radiation pattern of a single receiver within a parabolic cylinder. In this case, the far-field region is around 175 m. At this height, a modern battery-powered drone should be suitable. Once the radiation pattern of all the receivers within the BEST-2 array are obtained, they can be combined to produce the corresponding synthesised beam as shown in Chapter 2. In principle, this method makes it possible to verify any phased array, albeit it would require multiple observation campaigns to characterise all the elements within large phased arrays. This emphasises the need for a real-time antenna verification system that makes it possible to expedite the analysis of the incoming data.

A.2 Performance metrics

SNR	Algorithm	Time		Recall		Specificity		Score	
		<i>mean</i>	<i>std</i>	<i>mean</i>	<i>std</i>	<i>mean</i>	<i>std</i>	<i>mean</i>	<i>std</i>
0	Iso Data	0.04	0.00	1.00	0.01	0.80	0.00	0.89	0.00
0	Otsu Filter	0.04	0.00	1.00	0.01	0.80	0.00	0.89	0.00
0	Sigma Clip	0.04	0.00	0.28	0.05	0.96	0.00	0.43	0.05
0	Triangle	0.04	0.00	0.33	0.13	0.95	0.02	0.47	0.13
0	Yen	0.04	0.00	0.00	0.00	1.00	0.00	0.01	0.00
1	Iso Data	0.04	0.00	1.00	0.00	0.80	0.00	0.89	0.00
1	Otsu Filter	0.04	0.00	1.00	0.00	0.80	0.01	0.89	0.00
1	Sigma Clip	0.04	0.00	0.51	0.10	0.96	0.00	0.67	0.07
1	Triangle	0.04	0.00	0.54	0.20	0.96	0.02	0.67	0.14
1	Yen	0.04	0.00	0.01	0.00	1.00	0.00	0.01	0.01
2	Iso Data	0.04	0.00	1.00	0.00	0.80	0.00	0.89	0.00
2	Otsu Filter	0.04	0.00	1.00	0.00	0.80	0.01	0.89	0.00
2	Sigma Clip	0.04	0.00	0.93	0.05	0.96	0.00	0.95	0.03
2	Triangle	0.04	0.00	0.93	0.10	0.95	0.01	0.94	0.05
2	Yen	0.04	0.00	0.01	0.01	1.00	0.00	0.03	0.02
3	Iso Data	0.04	0.00	1.00	0.00	0.80	0.00	0.89	0.00
3	Otsu Filter	0.04	0.00	1.00	0.00	0.80	0.00	0.89	0.00
3	Sigma Clip	0.04	0.00	1.00	0.00	0.96	0.00	0.98	0.00
3	Triangle	0.04	0.00	1.00	0.00	0.96	0.01	0.98	0.01
3	Yen	0.04	0.00	0.06	0.05	1.00	0.00	0.11	0.08
4	Iso Data	0.04	0.00	1.00	0.00	0.81	0.00	0.89	0.00
4	Otsu Filter	0.04	0.00	1.00	0.00	0.80	0.01	0.89	0.00
4	Sigma Clip	0.04	0.00	1.00	0.00	0.96	0.00	0.98	0.00
4	Triangle	0.04	0.00	1.00	0.00	0.96	0.01	0.98	0.01
4	Yen	0.04	0.00	0.25	0.29	1.00	0.00	0.35	0.29
5	Iso Data	0.04	0.00	1.00	0.00	0.81	0.00	0.89	0.00
5	Otsu Filter	0.04	0.00	1.00	0.00	0.81	0.00	0.89	0.00
5	Sigma Clip	0.04	0.00	1.00	0.00	0.96	0.00	0.98	0.00
5	Triangle	0.04	0.00	1.00	0.00	0.96	0.01	0.98	0.01
5	Yen	0.04	0.00	1.00	0.00	1.00	0.00	1.00	0.00
6	Iso Data	0.04	0.00	1.00	0.00	0.81	0.00	0.89	0.00
6	Otsu Filter	0.04	0.00	1.00	0.00	0.81	0.00	0.89	0.00
6	Sigma Clip	0.04	0.00	1.00	0.00	0.96	0.00	0.98	0.00
6	Triangle	0.04	0.00	1.00	0.00	0.95	0.01	0.98	0.01
6	Yen	0.04	0.00	1.00	0.00	1.00	0.00	1.00	0.00

Table A.1: Performance metrics for the image segmentation algorithms presented in Chapter 4

SNR	Algorithm	Time		F1		Precision		Recall	
		<i>mean</i>	<i>std</i>	<i>mean</i>	<i>std</i>	<i>mean</i>	<i>std</i>	<i>mean</i>	<i>std</i>
0	Astride	1.99	0.03	0.00	0.00	0.00	0.00	0.00	0.00
0	DBSCAN	0.53	0.18	0.02	0.06	0.07	0.21	0.01	0.04
0	Hough	0.22	0.11	0.00	0.00	0.00	0.00	0.00	0.00
0	MSDS	1.66	0.86	0.12	0.15	0.30	0.31	0.10	0.14
1	Astride	1.99	0.04	0.08	0.10	0.25	0.26	0.05	0.07
1	DBSCAN	0.49	0.19	0.13	0.20	0.28	0.36	0.10	0.16
1	Hough	0.20	0.11	0.00	0.00	0.00	0.00	0.00	0.00
1	MSDS	1.49	0.87	0.40	0.21	0.67	0.28	0.33	0.25
2	Astride	1.99	0.03	0.39	0.07	0.41	0.02	0.39	0.12
2	DBSCAN	0.52	0.16	0.52	0.23	0.64	0.25	0.46	0.25
2	Hough	0.21	0.10	0.17	0.21	0.39	0.41	0.12	0.17
2	MSDS	1.68	0.80	0.83	0.09	0.81	0.12	0.88	0.10
3	Astride	2.00	0.04	0.38	0.07	0.40	0.02	0.38	0.13
3	DBSCAN	0.50	0.16	0.58	0.27	0.65	0.25	0.55	0.31
3	Hough	0.19	0.10	0.17	0.30	0.24	0.38	0.15	0.30
3	MSDS	1.51	0.78	0.89	0.06	0.84	0.10	0.96	0.02
4	Astride	2.00	0.03	0.38	0.07	0.40	0.02	0.37	0.12
4	DBSCAN	0.49	0.18	0.61	0.29	0.64	0.25	0.61	0.33
4	Hough	0.19	0.10	0.21	0.27	0.37	0.39	0.16	0.22
4	MSDS	1.50	0.77	0.88	0.10	0.82	0.13	0.95	0.07
5	Astride	2.02	0.04	0.38	0.07	0.40	0.03	0.37	0.12
5	DBSCAN	0.51	0.19	0.68	0.18	0.70	0.12	0.67	0.25
5	Hough	0.19	0.10	0.24	0.28	0.41	0.44	0.19	0.23
5	MSDS	1.51	0.77	0.88	0.11	0.82	0.14	0.95	0.08
6	Astride	1.99	0.05	0.38	0.07	0.40	0.03	0.37	0.12
6	DBSCAN	0.51	0.18	0.64	0.27	0.66	0.25	0.63	0.32
6	Hough	0.20	0.11	0.24	0.24	0.46	0.42	0.18	0.20
6	MSDS	1.57	0.83	0.89	0.10	0.84	0.13	0.95	0.07
7	Astride	2.00	0.03	0.38	0.07	0.40	0.03	0.37	0.12
7	DBSCAN	0.49	0.14	0.73	0.28	0.71	0.26	0.77	0.33
7	Hough	0.20	0.10	0.30	0.30	0.46	0.41	0.25	0.29
7	MSDS	1.52	0.79	0.91	0.09	0.87	0.13	0.97	0.03

Table A.2: Performance metrics for the feature detection algorithms presented in Chapter 4

Bibliography

- [1] European Space Operations Center (ESOC). ESA's Annual Space Environment Report; 2019.
- [2] Klinkrad H. Space debris. Encyclopedia of Aerospace Engineering. 2010;.
- [3] Space Debris Mitigation Guidelines of the Committee on the Peaceful Uses of Outer Space. Vienna: United Nations Office for Outer Space Affairs; 2010.
- [4] Alessi E, Deleflie F, Rosengren A, Rossi A, Valsecchi G, Daquin J, et al. A numerical investigation on the eccentricity growth of GNSS disposal orbits. *Celestial Mechanics and Dynamical Astronomy*. 2016;125(1):71–90.
- [5] Bonnal C, McKnight DS. IAA Situation Report on Space Debris. International Academy of Astronautics (IAA); 2016.
- [6] Pupillo G, Salerno E, Bartolini M, Di Martino M, Mattana A, Montebugnoli S, et al. The INAF contribution to the ASI Space Debris program: observational activities. *Memorie della Societa Astronomica Italiana Supplementi*. 2012;20:43.
- [7] Council NR, Sciences DEP, Board ASE, Programs CANOD. Limiting Future Collision Risk to Spacecraft: An Assessment of NASA's Meteoroid and Orbital Debris Programs. National Academies Press; 2011.
- [8] Markkanen J, Lehtinen M, Landgraf M. Real-time space debris monitoring with EISCAT. *Advances in Space Research*. 2005;35(7):1197–1209.
- [9] Bauer W, Romberg O, Wiedemann C, Drolshagen G, Vörsmann P. Development of in-situ Space Debris Detector. *Advances in Space Research*. 2014;54(9):1858–1869.

- [10] Drolshagen G. EURECA and HST solar array post-flight impact analysis. *Earth Space Review*. 1995;4(3):15–18.
- [11] Klinkrad H. *Space debris*. Springer; 2006.
- [12] Mathews JD, Janches D, Meisel D, Zhou QH. The micrometeoroid mass flux into the upper atmosphere: Arecibo results and a comparison with prior estimates. *Geophysical Research Letters*. 2001;28(10):1929–1932.
- [13] Yuan W, Zhang C, Song Q, Zhang B. Research on space target surveillance radar technology. *Proceedings of 2011 IEEE CIE International Conference on Radar, RADAR 2011*. 2011;1:1–3.
- [14] Schildknecht T. Optical surveys for space debris. *Astronomy and Astrophysics Review*. 2007;14(1):41–111.
- [15] Ender J, Leushacke L, Brenner A, Wilden H. Radar techniques for space situational awareness. *2011 12th International Radar Symposium (IRS)*. 2011;p. 21–26.
- [16] Zhao Z, Zhao Y, Gao PQ. Analyzing the capability of a radio telescope in a bistatic space debris observation system. *Research in Astronomy and Astrophysics*. 2013;13(12):1518–1526.
- [17] Virgili BB, Dolado J, Lewis H, Radtke J, Krag H, Revelin B, et al. Risk to space sustainability from large constellations of satellites. *Acta Astronautica*. 2016;126:154–162.
- [18] Kessler DJ, Cour-Palais BG. Collision frequency of artificial satellites: The creation of a debris belt. *Journal of Geophysical Research: Space Physics*. 1978;83(A6):2637–2646.
- [19] *Space debris mitigation guidelines*. Inter-Agency Space Debris Coordination Committee (IADC); 2007.
- [20] Lim SM, Kim HD, Seong JD. Vision-based ground test for active debris removal. *Journal of Astronomy and Space Sciences*. 2013;30(4):279–290.
- [21] Alby F. Spot 1 end of life disposition manoeuvres. *Advances in Space Research*. 2005;35(7):1335–1342.

- [22] McKnight DS, Pentino FRD. New insights on the orbital debris collision hazard at GEO. *Acta Astronautica*. 2013;85:73 – 82.
- [23] Jehn R, Agapov V, Hernández C. End-of disposal of geostationary satellites. In: 4th European Conference on Space Debris. vol. 587; 2005. p. 373.
- [24] Abdel-Aziz YA. An analytical theory for avoidance collision between space debris and operating satellites in LEO. *Applied Mathematical Modelling*. 2013;37(18):8283 – 8291.
- [25] Percy TK, Landrum DB. Investigation of national policy shifts to impact orbital debris environments. *Space Policy*. 2014;30(1):23 – 33.
- [26] Sánchez-Ortiz N, Belló-Mora M, Klinkrad H. Collision avoidance manoeuvres during spacecraft mission lifetime: Risk reduction and required δv . *Advances in Space Research*. 2006;38(9):2107–2116.
- [27] Foster J. The analytic basis for debris avoidance operations for the International Space Station; 2001.
- [28] Montebugnoli S, Pupillo G, Salerno E, Pluchino S, di Martino M. The bistatic radar capabilities of the Medicina radiotelescopes in space debris detection and tracking. *Advances in Space Research*. 2010;45(5):676–682.
- [29] Lizia PD, Massari M, Losacco M, Bianchi G, Mattana A, Pupillo G, et al. Performance assessment of the multibeam radar sensor birales for space surveillance and tracking. In: 7th European Conference on Space Debris; 2017. p. 1–13.
- [30] Rossi A, Valsecchi G. Collision risk against space debris in Earth orbits. *Celestial Mechanics and Dynamical Astronomy*. 2006;95(1-4):345–356.
- [31] Hernández C, Pina F, Sánchez N, Sdunnus H, Klinkrad H. The DISCOS database and web interface. In: Proceedings of the Third European Conference on Space Debris; 2001. p. 803–807.
- [32] Carl JR, Arndt GD, Bourgoise BA, Paz I. Space-borne radar detection of orbital debris. Proceedings of GLOBECOM '93 IEEE Global Telecommunications Conference. 1993;p. 939–943.

- [33] Brian W, Cefola P, Sankaran J. Global space situational awareness sensors. In: AMOS Conference; 2010. .
- [34] Adnerson PV. Characterizing Longitude-dependent orbital debris congestion in the GSO regime. University of Colorado. 2014;.
- [35] Grassi M, Cetin E, Dempster AG. Enabling orbit determination of space debris using narrowband radar. *IEEE Transactions on Aerospace and Electronic Systems*. 2015;51(2):1231–1240.
- [36] Walsh DW. A Survey of Radars Capable of Providing Small Debris Measurements for Orbit Prediction; 2013.
- [37] Brown WM, Pensa AF. History of Haystack. *Lincoln Laboratory Journal*. 2014;21(1):1–4.
- [38] Busch MW. Shapes and Spins of Near-Earth Asteroids. Universal-Publishers; 2010.
- [39] Matney M, Goldstein R, Kessler D, Stansbery E. Recent results from Goldstone orbital debris radar. *Advances in Space Research*. 1999;23(1):5–12.
- [40] Vierinen J, Kastinen D, Markkanen J, Grydeland T, Kero J, Horstmann A, et al. 2018 BEAM-PARK OBSERVATIONS OF SPACE DEBRIS WITH THE EISCAT RADARS. January; 2019. p. 22–24.
- [41] Markkanen J, Jehn R, Krag H. EISCAT space debris during the IPY—a 5000 hour campaign. In: Proc. 5th ESA space debris conference; 2009. .
- [42] Li A, Close S, Markkannen J. EISCAT Space Debris after the International Polar Year (IPY). In: Conference Proceedings from IAC. vol. 12; 2012. p. A6.
- [43] Vierinen J, Markkanen J, Krag H. High power large aperture radar observations of the Iridium-COSMOS collision. In: Proc. 5th ESA space debris conference; 2009. .
- [44] McCrea I, Aikio A, Alfonsi L, Belova E, Buchert S, Clilverd M, et al. The science case for the EISCAT_3D radar. vol. 2. *Progress in Earth and Planetary Science*; 2015.

- [45] Vierinen J, Markkanen J, Krag H, Siminski J, Mancas A. Use of Eiscat 3D for Observations of Space Debris. In: 7th European Conference on Space Debris ESA/ESOC, Darmstadt/Germany 18 - 21 April 2017. April; 2017. p. 18–21.
- [46] Michal T, Eglizeaud JP, Bouchard J. GRAVES: The new French system for space surveillance. In: European Space Agency, (Special Publication) ESA SP. 587; 2005. p. 61–66.
- [47] Klinkrad H. Space Debris: Models and Risk Analysis. Springer-Verlag Berlin Heidelberg; 2006.
- [48] Mehrholz D, Leushacke L, Flury W, Jehn R, Klinkrad H, Landgraf M. Detecting, tracking and imaging space debris. *ESA Bulletin*(0376-4265). 2002;109(109):128–134.
- [49] Flohrer T, Krag H. Space Surveillance and Tracking in ESA's SSA Programme. In: 7th European Conference on Space Debris; 2017. p. 18–21.
- [50] Morselli A, Armellin R, Di Lizia P, Bernelli-Zazzera F, Salerno E, Bianchi G, et al. Orbit Determination of Space Debris Using a Bi-Static Radar Configuration with a Multiple-Beam Receiver. *Proceedings of the International Astronautical Congress, IAC*. 2014;p. 1–11.
- [51] Piergentili F, Paolillo F, Cappelletti C, Cevolani G, Grassi G, Marti M, et al. Italian activity in space debris measurements. In: Fifth European Conference on Space Debris. vol. 672; 2009. p. 1–8.
- [52] Pupillo G, Montebugnoli S, Di Martino M, Salerno E, Bartolini M, Pluchino S, et al. Space debris radar experiments at the medicina VLBI dish. *European Space Agency, (Special Publication) ESA SP*. 2009;672 SP(April):2–5.
- [53] Losacco M, Di Lizia P, Massari M, Naldi G, Pupillo G, Bianchi G, et al. Initial orbit determination with the multibeam radar sensor BIRALES. *Acta Astronautica*. 2020;167:374–390.
- [54] Hall PJ. *The square kilometre array: An engineering perspective*. vol. 2. Springer; 2005.

- [55] Falcke HD, van Haarlem MP, de Bruyn AG, Braun R, Röttgering HJ, Stappers B, et al. A very brief description of LOFAR—the Low Frequency Array. *Proceedings of the International Astronomical Union*. 2006;2(14):386–387.
- [56] Perini F, Bianchi G, Monari J, Montebugnoli S, Schiaffino M. Skads. In: *First MCCT-SKADS Training School*. vol. 59. SISSA Medialab; 2008. p. 8.
- [57] Perini F, Bianchi G, Schiaffino M, Monari J. BEST receiver experience: general architecture, design and integration. In: *Wide Field Astronomy & Technology for the Square Kilometre Array*. vol. 132. SISSA Medialab; 2011. p. 62.
- [58] Montebugnoli S, Bianchi G, Bortolotti C, Cattani A, Cremonini A, Maccaferri A, et al. Italian SKA test bed based on cylindrical antennas. *Astronomische Nachrichten: Astronomical Notes*. 2006;327(5-6):624–625.
- [59] Montebugnoli S, Bianchi G, Monari J, Naldi G, Perini F, Schiaffino M. BEST: basic element for SKA training. In: *Wide Field Astronomy & Technology for the Square Kilometre Array*; 2009. .
- [60] Bolli P, Perini F, Montebugnoli S, Pelosi G, Poppi S. Basic element for square kilometer array training (BEST): Evaluation of the antenna noise temperature. *IEEE Antennas and Propagation Magazine*. 2008;50(2):58–65.
- [61] Hickish J. *Digital signal processing methods for large-n, low-frequency radio telescopes*. Oxford University; 2014.
- [62] Mailloux RJ. *Electronically scanned arrays*. vol. 6. Morgan & Claypool; 2007.
- [63] Hubregt J Visser. *Array and Phased Array Basics*. Chippenham, Wiltshire: John Wiley & Sons, Ltd; 2005.
- [64] Richards MA, Scheer JA, Holm WA. *Principles of Modern Radar, Volume I - Basic Principles*. vol. I. SciTech Publishing; 2010.
- [65] Van Trees HL. *Optimum Array Processing (Detection, Estimation, and Modulation Theory, Part IV)*. Part iv ed. Wiley, New York; 2002.

- [66] Stutzman WL, Thiele GA. Antenna Theory and Design, 3rd Edition. Antenna Theory and Design. Wiley; 2012.
- [67] Orfanidis SJ. Electromagnetic waves and antennas. Rutgers University New Brunswick, NJ; 2002.
- [68] Mailloux RJ. Phased Array Antenna Handbook. vol. 4. ARTECH HOUSE; 2005.
- [69] Revankar UK, Beenamole KS, Sreenivasulu K, Veerabhadra KM. Side-lobe minimisation in active phased arrays. IETE Technical Review (Institution of Electronics and Telecommunication Engineers, India). 2001;18(2-3):191–196.
- [70] Miller C. Minimizing the effects of phase quantization errors in an electronically scanned array. In: Proc. 1964 Symp. Electronically Scanned Phased Arrays and Applications. vol. 1; 1964. p. 17–38.
- [71] Chang C, Monstein C, Refregier A, Amara A, Glauser A, Casura S. Beam Calibration of Radio Telescopes with Drones. Publications of the Astronomical Society of the Pacific. 2015;127(957):1131–1143.
- [72] Ince AN, Topuz E, Panayirci E, Işık C. Principles of Integrated Maritime Surveillance Systems. Springer Science; 1998.
- [73] Wijnholds SJ, Tol SVD, Nijboer R, Veen AJVD. Calibration Challenges for the Next Generation of Radio Telescopes. Proceedings of the IEEE. 2010;2(c):1–12.
- [74] Foster G, Hickish J, Magro A, Price D, Zarb Adami K. Implementation of a direct-imaging and FX correlator for the BEST-2 array. Monthly Notices of the Royal Astronomical Society. 2014;439(3):3180–3188.
- [75] Boonstra AJ, Van der Veen AJ. Gain decomposition methods for radio telescope arrays. IEEE Workshop on Statistical Signal Processing Proceedings. 2001;31(0):365–368.
- [76] Salvini S, Wijnholds SJ. StEFCal - An Alternating Direction Implicit method for fast full polarization array calibration. 2014 31th URSI General Assembly and Scientific Symposium, URSI GASS 2014. 2014;p. 1–4.

- [77] Salvini S, Wijnholds SJ. Fast gain calibration in radio astronomy using alternating direction implicit methods: Analysis and applications. *Astronomy and Astrophysics*. 2014;571:1–14.
- [78] Morselli A, Lizia PD, Bianchi G, Bortolotti C, Montebugnoli S, Naldi G, et al. A new high sensitivity radar sensor for space debris detection and accurate orbit determination. In: *2015 IEEE Metrology for Aerospace (MetroAeroSpace)*; 2015. p. 562–567.
- [79] Parliament E, of the Council. Parliament E, of the Council, editors. Decision. Establishing a Framework for Space Surveillance and Tracking Support no 541/2014/EU; 2014.
- [80] Njoku EG. *Encyclopedia of remote sensing*. 1st ed. California: Springer-Verlag New York; 2014.
- [81] Banka D, Leushacke L, Mehrholz D. Beam-park-experiment-1/2000 with TIRA. *Space Debris*. 2000;2(2):83–96.
- [82] Chen WK. *The electrical engineering handbook*. 1st ed. Elsevier; 2005.
- [83] Kostylev VI, Blyakhman AB, Ryndyk AG. *Bistatic Radar : Principles and Practice*. John Wiley & Sons Ltd; 2007.
- [84] Hart R. Single-station Tracking for Orbit Determination of Small Satellites. Technical Session VI: Small Satellites - Support Systems (Small Satellite Conference). 1987;p. 1–8.
- [85] Curry GR. *Radar Essentials*. Scitech Publishing; 2011.
- [86] Maddalena R, Johnson C. High precision calibration of data from single-dish radio telescopes. In: *Bulletin of the American Astronomical Society*. vol. 37; 2005. p. 1438.
- [87] Bemporad A. On the theory of the extinction of light in the earth's atmosphere. *Grand Ducal Observatory Heidelberg*. 1904;4.
- [88] Zaitsev AL, Ignatov S, Di Martino M, Montebugnoli S, Nabatov A. A proposal for radar detection of centimetric space debris in geostationary ring. In: *Proceedings of the Third European Conference on Space Debris, ESA SP-473*. ESA Publications Division, Noordwijk, The Netherlands; 2001. p. 79–81.

- [89] Muntoni G. Space debris observations with the Sardinia radio telescope. Universita di Cagliari; 2019.
- [90] Pisanu T, Schirru L, Urru E, Ortu P, Inaf C, Scienza V, et al. Upgrading the Italian BIRALES System to a Pulse Compression Radar for Space Debris Range Measurements. 2018 22nd International Microwave and Radar Conference (MIKON). 2018;p. 317–320.
- [91] Montebugnoli S, Perini F, Bianchi G, Bolli P, Pupillo G, Naldi G, et al. Some results from the BEST demonstrator. In: Wide Field Astronomy & Technology for the Square Kilometre Array. vol. 132. SISSA Medialab; 2011. p. 59.
- [92] Ruiz G, Patzelt T, Leushack L, Loffeld O. Autonomous tracking of space objects with the FGAN tracking and imaging radar. INFORMATIK 2006 - Informatik fur Menschen, Beitrage der 36 Jahrestagung der Gesellschaft fur Informatik eV (GI). 2006;1(17820):349–353.
- [93] for Space Data Systems (CCSDS) TCC. Recommendation for Space Data System Standards Tracking data message recommended standard. The Consultative Committee for Space Data Systems (CCSDS); 2007.
- [94] Losacco Mea. The multibeam radar sensor BIRALES: performance assessment for space surveillance and tracking. In: Proceedings of the 40th IEEE Aerospace Conference. Montana, USA; 2019. p. 1–9.
- [95] Raju GSN. Radar Engineering. I.K. International Publishing House Pvt. Limited; 2008.
- [96] Jankiraman M. FMCW Radar Design. Artech House radar library. Artech House; 2018.
- [97] Hickish J, Abdurashidova Z, Ali Z, Buch KD, Chaudhari SC, Chen H, et al. A decade of developing radio-astronomy instrumentation using casper open-source technology. Journal of Astronomical Instrumentation. 2016;5(04):1641001.
- [98] Jonas J, et al. The MeerKAT radio telescope. In: MeerKAT Science: On the Pathway to the SKA. vol. 277. SISSA Medialab; 2018. p. 001.

- [99] Parsons AR, Backer DC, Foster GS, Wright MC, Bradley RF, Gugliucci NE, et al. The precision array for probing the epoch of re-ionization: Eight station results. *The Astronomical Journal*. 2010;139(4):1468.
- [100] Magro A, Hickish J, Adami KZ. Multibeam Gpu Transient Pipeline for the Medicina Best-2 Array. *Journal of Astronomical Instrumentation*. 2013;02(01):1350008.
- [101] Manley J, Welz M, Parsons A, Ratcliffe S, Van Rooyen R. SPEAD: streaming protocol for exchanging astronomical data. SKA document. 2010;.
- [102] Farnes J, Mort B, Dulwich F, Salvini S, Armour W. Science Pipelines for the Square Kilometre Array. *Galaxies*. 2018;6(4):120.
- [103] Quinn P, Axelrod T, Bird I, Dodson R, Szalay A, Wicenec A. Delivering SKA science. arXiv preprint arXiv:150105367. 2015;p. 1–26.
- [104] Jones DL, Wagstaff K, Thompson DR, D’Addario L, Navarro R, Mattmann C, et al. Big data challenges for large radio arrays. In: 2012 IEEE Aerospace Conference. IEEE; 2012. p. 1–6.
- [105] Price D, Staveley-Smith L, Bailes M, Carretti E, Jameson A, Jones M, et al. HIPSR: A Digital Signal Processor for the Parkes 21-cm Multibeam Receiver. *Journal of Astronomical Instrumentation*. 2016;5(04):1641007.
- [106] Garofalakis M, Gehrke J, Rastogi R. Data stream management: processing high-speed data streams. Springer; 2016.
- [107] Mort B, Dulwich F, Williams C, Salvini S. Pelican: Pipeline for Extensible, Lightweight Imaging and CALibration. *Astrophysics Source Code Library*. 2015;.
- [108] Cranmer MD, Barsdell BR, Price DC, Dowell J, Garsden H, Dike V, et al. Bifrost: a Python/C++ Framework for High-Throughput Stream Processing in Astronomy; 2017.
- [109] Virtanen J, Poikonen J, Sääntti T, Komulainen T, Torppa J, Granvik M, et al. Streak detection and analysis pipeline for space-debris optical images. *Advances in Space Research*. 2016;57(8):1607–1623.

- [110] Lanaro G. Python High Performance Programming. Packt Publishing; 2013.
- [111] Gorelick M, Ozsvald I. High Performance Python: Practical Performant Programming for Humans. O'Reilly Media; 2014.
- [112] Lam SK, Pitrou A, Seibert S. Numba: A LLVM-based python JIT compiler. In: Proceedings of the Second Workshop on the LLVM Compiler Infrastructure in HPC. ACM; 2015. p. 7.
- [113] Burrowbridge SE. Optimal allocation of satellite network resources. Virginia Tech; 1999.
- [114] Schalck SM. Automating satellite range scheduling. AIR FORCE INST OF TECH WRIGHT-PATTERSON AFB OH; 1993.
- [115] Barbulescu L, Howe AE, Whitley LD, Roberts M. Understanding algorithm performance on an oversubscribed scheduling application. Journal of Artificial Intelligence Research. 2006;27:577–615.
- [116] Agaba D. System Design of the MeerKAT L - band 3D Radar for Monitoring Near Earth Objects. University of Cape Town; 2017.
- [117] Magro A, Bugeja K, Chiello R, DeMarco A. A High-Performance, Flexible Data Acquisition Library for Radio Instruments. In: 2019 IEEE-APS Topical Conference on Antennas and Propagation in Wireless Communications (APWC); 2019. p. 69–74.
- [118] MADISETTI V. The Digital Signal Processing Handbook. Electrical Engineering Handbook. Taylor & Francis; 1997.
- [119] Losacco M, Di Lizia P, Massari M, Mattana A, Perini F, Schiaffino M, et al. Orbit determination of resident space objects with the multibeam radar sensor BIRALES. In: 2018 Space Flight Mechanics Meeting; 2018. p. 7–29.
- [120] Cutajar D, Magro A, Borg J, Zarb Adami K, Bianchi G, Bortolotti C, et al. A real-time space debris detection system for BIRALES. In: 69th International Astronautical Congress (IAC 2018); 2018. p. 1–9.

- [121] Smith SW, et al. The scientist and engineer's guide to digital signal processing. California Technical Pub. San Diego; 1997.
- [122] Bellanger M, Bonnerot G, Coudreuse M. Digital filtering by polyphase network: Application to sample-rate alteration and filter banks. *IEEE Transactions on Acoustics, Speech, and Signal Processing*. 1976;24(2):109–114.
- [123] Schafer R, Rabiner L. Design and simulation of a speech analysis-synthesis system based on short-time Fourier analysis. *IEEE Transactions on Audio and Electroacoustics*. 1973;21(3):165–174.
- [124] Harris C, Haines K. A mathematical review of polyphase filterbank implementations for radio astronomy. *Publications of the Astronomical Society of Australia*. 2011;28(4):317–322.
- [125] Price DC. Spectrometers and polyphase filterbanks in radio astronomy. arXiv preprint arXiv:160703579. 2016;.
- [126] Lampert TA, O'Keefe SE. A survey of spectrogram track detection algorithms. *Applied acoustics*. 2010;71(2):87–100.
- [127] Magro A, DeMarco A, Adami KZ, Cutajar D, Borg J. A monitoring and control prototype for the SKA low frequency aperture array. In: 2017 International Conference on Control, Automation and Diagnosis (ICCAD). IEEE; 2017. p. 451–456.
- [128] Magro A, Chiello R, Cutajar D, Borg J, Zarb-Adami K, Gonzalez-Esparza A, et al. A New Digital Backend for the Mexican Array Radio Telescope. In: 2019 International Conference on Electromagnetics in Advanced Applications (ICEAA). IEEE; 2019. p. 185–189.
- [129] Virtanen J, Flohrer T, Muinonen K, Granvik M, Torppa J, Poikonen J, et al. StreakDet data processing and analysis pipeline for space debris optical observations. In: 40th COSPAR Scientific Assembly. vol. 40; 2014. p. 8–14.
- [130] Tagawa M, Yanagisawa T, Kurosaki H, Oda H, Hanada T. Orbital objects detection algorithm using faint streaks. *Advances in Space Research*. 2015;57(4):929–937.

- [131] Kim DW, Byun YI, Kim SY. Automated streak detection for high velocity objects: Test with YSTAR-NEOPAT images. *Journal of Astronomy and Space Sciences*. 2005;22(4):385–392.
- [132] Lorensen WE, Cline HE. Marching cubes: A high resolution 3D surface construction algorithm. *Computer Graphics*. 1987;21(4):163–169.
- [133] Koenig W, Dunn H, Lacy L. The sound spectrograph. *The Journal of the Acoustical Society of America*. 1946;18(1):19–49.
- [134] Lee C, Yoon C, Kong HJ, Kim HC, Kim Y. Heart rate tracking using a doppler radar with the reassigned joint time-frequency transform. *IEEE Antennas and Wireless Propagation Letters*. 2011;10:1096–1099.
- [135] Dutta PK, Arora AK, Bibyk SB. Towards radar-enabled sensor networks. *Proceedings of the Fifth International Conference on Information Processing in Sensor Networks, IPSN '06*. 2006;2006:467–474.
- [136] Roy A, Gale N, Hong L. Automated traffic surveillance using fusion of Doppler radar and video information. *Mathematical and Computer Modelling*. 2011;54(1-2):531–543.
- [137] Ram SS, Li Y, Lin A, Ling H. Doppler-based detection and tracking of humans in indoor environments. *Journal of the Franklin Institute*. 2008;345(6):679–699.
- [138] Harmanny RIA, De Wit JJM, Prémel Cabic G. Radar micro-Doppler feature extraction using the spectrogram and the cepstrogram. *European Microwave Week 2014: 'Connecting the Future', EuMW 2014 - Conference Proceedings; EuRAD 2014: 11th European Radar Conference*. 2014;p. 165–168.
- [139] Tahmoush D, Silvius J. Radar Micro-Doppler for Long Range Front-View Gait Recognition. In: *IEEE 3rd International Conference on Biometrics: Theory, Applications, and Systems; 2009*. p. 1–6.
- [140] Morrissey R, Ward J, DiMarzio N, Jarvis S, Moretti D. Passive acoustic detection and localization of sperm whales (*Physeter macrocephalus*) in the tongue of the ocean. *Applied acoustics*. 2006;67(11-12):1091–1105.

- [141] Mellinger DK, Nieukirk SL, Matsumoto H, Heimlich SL, Dziak RP, Haxel J, et al. Seasonal occurrence of North Atlantic right whale (*Eubalaena glacialis*) vocalizations at two sites on the Scotian Shelf. *Marine Mammal Science*. 2007;23(4):856–867.
- [142] Chen CH, Lee JD, Lin MC. Classification of underwater signals using neural networks. *Tamkang Journal of Science and Engineering*. 2000;3(1):31–48.
- [143] Yang S, Li Z, Wang X. Ship recognition via its radiated sound: The fractal based approaches. *The Journal of the Acoustical Society of America*. 2002;112(1):172–177.
- [144] Paris S, Jauffret C. A new tracker for multiple frequency line. In: 2001 IEEE Aerospace Conference Proceedings (Cat. No. 01TH8542). vol. 4. IEEE; 2001. p. 4–1771.
- [145] Lampert TA, O’Keefe SE. Active contour detection of linear patterns in spectrogram images. In: 2008 19th International Conference on Pattern Recognition. IEEE; 2008. p. 1–4.
- [146] Abel JS, Lee HJ, Lowell AP. An image processing approach to frequency tracking (application to sonar data). In: ICASSP-92: 1992 IEEE International Conference on Acoustics, Speech, and Signal Processing. vol. 2. IEEE; 1992. p. 561–564.
- [147] Di Martino JC, Tabbone S. An approach to detect lofar lines. *Pattern Recognition Letters*. 1996;17(1):37–46.
- [148] Lu M, Li M, Mao W. The detection and tracking of weak frequency line based on double-detection algorithm. In: 2007 International Symposium on Microwave, Antenna, Propagation and EMC Technologies for Wireless Communications. IEEE; 2007. p. 1195–1198.
- [149] Hocking W, Fuller B, Vandeppeer B. Real-time determination of meteor-related parameters utilizing modern digital technology. *Journal of Atmospheric and Solar-Terrestrial Physics*. 2001;63(2-3):155–169.
- [150] Wen CH, Doherty JF, Mathews JD, Janches D. Meteor detection and non-periodic bursty interference removal for Arecibo data. *Journal of Atmospheric and Solar-Terrestrial Physics*. 2005;67(3):275–281.

- [151] Weryk RJ, Brown PG. Simultaneous radar and video meteors - I: Metric comparisons. *Planetary and Space Science*. 2012;62(1):132–152.
- [152] Roman VŞ, Buiu C. Automatic analysis of radio meteor events using neural networks. *Earth, Moon, and Planets*. 2015;116(2):101–113.
- [153] Gonzalez RC, Woods RE. *Digital Image Processing (3rd Edition)*. USA: Prentice-Hall, Inc.; 2006.
- [154] Lampert TA, O’Keefe SEM. A detailed investigation into low-level feature detection in spectrogram images. *Pattern Recognition*. 2011;44(9):2076–2092.
- [155] Barrett R, McMahon D, et al. ML estimation of the fundamental frequency of a harmonic series. In: *1st IASTED International Symposium on Signal Processing and its Applications*. Institution of Engineers, Australia; 1987. .
- [156] Rife D, Boorstyn R. Single tone parameter estimation from discrete-time observations. *IEEE Transactions on information theory*. 1974;20(5):591–598.
- [157] Jolliffe IT, Cadima J. Principal component analysis: a review and recent developments. *Philosophical Transactions of the Royal Society A: Mathematical, Physical and Engineering Sciences*. 2016;374(2065):20150202.
- [158] Adams GJ, Evans RJ. Neural networks for frequency line tracking. *IEEE Transactions on Signal Processing*. 1994;42(4):936–941.
- [159] Barniv Y. Dynamic programming solution for detecting dim moving targets. *IEEE Transactions on Aerospace and Electronic Systems*. 1985;p. 144–156.
- [160] Streit RL, Barrett RF. Frequency line tracking using hidden Markov models. *IEEE Transactions on Acoustics, Speech, and Signal Processing*. 1990;38(4):586–598.
- [161] Otsu N. A threshold selection method from gray-level histograms. *IEEE transactions on systems, man, and cybernetics*. 1979;9(1):62–66.

- [162] Glasbey CA. An analysis of histogram-based thresholding algorithms. *CVGIP: Graphical models and image processing*. 1993;55(6):532–537.
- [163] Prewitt JM, Mendelsohn ML. The analysis of cell images. *Annals of the New York Academy of Sciences*. 1966;128(3):1035–1053.
- [164] Yen JC, Chang FJ, Chang S. A new criterion for automatic multilevel thresholding. *IEEE Transactions on Image Processing*. 1995;4(3):370–378.
- [165] Sezgin M, Sankur B. Survey over image thresholding techniques and quantitative performance evaluation. *Journal of Electronic imaging*. 2004;13(1):146–166.
- [166] Zack GW, Rogers WE, Latt S. Automatic measurement of sister chromatid exchange frequency. *Journal of Histochemistry & Cytochemistry*. 1977;25(7):741–753.
- [167] Young IT, Gerbrands JJ, Van Vliet LJ. *Fundamentals of image processing*. Delft University of Technology; 1998.
- [168] Illingworth J, Kittler J. A survey of the Hough transform. *Computer vision, graphics, and image processing*. 1988;44(1):87–116.
- [169] Jain AK, Murty MN, Flynn PJ. Data clustering: a review. *ACM computing surveys (CSUR)*. 1999;31(3):264–323.
- [170] Bojchevski A, Matkovic Y, Günnemann S. Robust spectral clustering for noisy data: Modeling sparse corruptions improves latent embeddings. In: *Proceedings of the 23rd ACM SIGKDD International Conference on Knowledge Discovery and Data Mining*; 2017. p. 737–746.
- [171] Von Luxburg U. A tutorial on spectral clustering. *Statistics and computing*. 2007;17(4):395–416.
- [172] Ester M, Kriegel HP, Sander J, Xu X, et al. A density-based algorithm for discovering clusters in large spatial databases with noise. In: *Kdd*. vol. 96; 1996. p. 226–231.
- [173] Beyeler M. *Machine Learning for OpenCV*. june. Packt Publishing Ltd; 2018.

- [174] Wyrzykowski R, Dongarra J, Paprzycki M, Wasniewski J. *Parallel Processing and Applied Mathematics: 4th International Conference, PPAM 2001 Naleczow, Poland, September 9-12, 2001 Revised Papers*. vol. 2328. Springer; 2003.
- [175] Rajasekaran S, Reif J. *Handbook of Parallel Computing: Models, Algorithms and Applications*. Chapman & Hall/CRC Computer and Information Science Series. CRC Press; 2007.
- [176] Samet H. *Foundations of multidimensional and metric data structures*. Morgan Kaufmann; 2006.
- [177] Foster I. *Designing and Building Parallel Programs: Concepts and Tools for Parallel Software Engineering*. Addison-Wesley; 1995.
- [178] Müllner D. *Modern hierarchical, agglomerative clustering algorithms*. arXiv preprint arXiv:11092378. 2011;.
- [179] Everitt BS, Landau S, Leese M, Stahl D. *Cluster analysis*. John Wiley & Sons; 2011.
- [180] Mandal JK, Bhattacharya D. *Emerging Technology in Modelling and Graphics: Proceedings of IEM Graph 2018*. *Advances in Intelligent Systems and Computing*. Springer Singapore; 2019.
- [181] Fischler MA, Bolles RC. *Random sample consensus: a paradigm for model fitting with applications to image analysis and automated cartography*. *Communications of the ACM*. 1981;24(6):381–395.
- [182] Pupillo G, Pluchino S, Bolli P, Virone G, Mariotti S, Monari J, et al. *UAV-based method for the sensitivity measurement on low-frequency receiving systems*. In: *Proceedings of the 2017 19th International Conference on Electromagnetics in Advanced Applications, ICEAA 2017*; 2017. p. 1232–1235.
- [183] Kraus JD. *Radio astronomy*. New York: McGraw-Hill, 1966. 1966;.
- [184] Baars J, Genzel R, Pauliny-Toth I, Witzel A. *The absolute spectrum of CAS A—an accurate flux density scale and a set of secondary calibrators*. *Astronomy and Astrophysics*. 1977;61:99–106.

- [185] Stehle RH, DesBrisay GA, Whitson AL, Hagn GH. RELEDOP: a full-scale antenna pattern measurement system for high-powered HF transmitting antennas. *IEEE transactions on broadcasting*. 1988;34(2):210–220.
- [186] Witvliet BA. Airborne evaluation/verification of antenna patterns of broadcasting stations. In: 18th International Wroclaw Symposium and Exhibition on Electromagnetic Compatibility 2006; 2006. .
- [187] Virone G, Lingua AM, Piras M, Cina A, Perini F, Monari J, et al. Antenna pattern verification system based on a micro unmanned aerial vehicle (UAV). *IEEE Antennas and Wireless Propagation Letters*. 2014;13:169–172.
- [188] Üstüner F, Aydemir E, Güleç E, Ilarslan M, Çelebi M, Demirel E. Antenna radiation pattern measurement using an unmanned aerial vehicle (UAV). In: General Assembly and Scientific Symposium (URSI GASS), 2014 31st URSI. IEEE; 2014. p. 1–4.
- [189] Pupillo G, Naldi G, Bianchi G, Mattana A, Monari J, Perini F, et al. Medicina array demonstrator: calibration and radiation pattern characterization using a UAV-mounted radio-frequency source. *Experimental Astronomy*. 2015;39(2):405–421.
- [190] Picar AM, Marqué C, Anciaux M, Lamy H, Ranvier S. Antenna Pattern Calibration of Radio Telescopes using an UAV-based device. In: 2015 International Conference on Electromagnetics in Advanced Applications (ICEAA). IEEE; 2015. p. 981–984.
- [191] Balanis CA. Antenna Theory: Analysis and Design. No. v. 1 in Antenna Theory: Analysis and Design. John Wiley & Sons; 2005.
- [192] Virone G, Paonessa F, Peverini O, Addamo G, Orta R, Tascone R, et al. Antenna pattern measurements with a flying far-field source (hexacopter). In: Antenna Measurements & Applications (CAMA), 2014 IEEE Conference on. IEEE; 2014. p. 1–2.